

UNIVERSITY OF OKLAHOMA
GRADUATE COLLEGE

SEQUENCE-STRATIGRAPHIC AND FACIES CONTROLS ON RESERVOIR
QUALITY AND PRODUCTIVITY OF EARLY TO MIDDLE MIOCENE FLUVIAL
AND TIDE-DOMINATED DELTAIC DEPOSITS, FORMATION 2,
GULF OF THAILAND

A THESIS
SUBMITTED TO THE GRADUATE FACULTY
in partial fulfillment of the requirements for the
Degree of
MASTER OF SCIENCE

By
PUNTIRA HENGLAI
Norman, Oklahoma
2018

© Copyright by PUNTIRA HENGLAI 2018
All Rights Reserved.

Acknowledgements

This research was funded and sponsored by PTT Exploration and Production Public Company Limited (PTTEP). Software was provided for use in research to the University of Oklahoma by Schlumberger (Petrel and Techlog) and CGG Geosolutions (Hampson-Russell). I would like to recognize Dr. Matthew Pranter for his guidance, patience, time, and support throughout the course of this project. I would also like to thank Dr. Kurt Marfurt and Dr. John Pigott for their input and advice. I would like to acknowledge Schlumberger for their donation of Petrel and Techlog. I would like to thank my fellow graduate students at OU: Antonio Cervantes, Richard Brito, Laura Sanchez, Ifunanya Ekwunife, David Duarte, and Phan Tien for their time and valuable friendship. I would like to thank my precious Thai friends: Paksamol Boonyuen, Puridej Warakunwit, and Parichat Phaodee for making me feel like I am at home. Lastly, I would like to thank my family for their support and unconditional love.

Table of Contents

Acknowledgements	iv
List of Tables	vii
List of Figures.....	viii
Abstract.....	ix
Introduction	1
Geological Setting	7
Methods	9
Lithofacies and Lithology Description and Electrofacies Classification	9
Depositional Environment.....	17
Stratigraphic and Structural Framework	17
Spatial Distribution of Lithology, Porosity, Permeability, and Pore Volume.....	21
Results	24
Formation 2 lithologies and lithofacies	24
Electrofacies Classification	28
Stratigraphic and Structural Framework	32
Spatial Distribution of Lithology, Porosity, Permeability, and Pore Volume.....	37
Discussion.....	47
Conclusions	54
References	57
Appendix A: Geological Setting	66
Appendix B: Core Descriptions.....	69
Appendix C: Stratigraphic and Structural Framework.....	106

Appendix D: Variograms	113
Appendix E: Spatial Distribution of Lithology and Reservoir Quality	128

List of Tables

Table 1. Variogram Parameters for Lithology Model	62
Table 2. Variogram Parameters for Petrophysical Models	63
Table 3. Lithologies and Lithofacies	64
Table 4. Parameters Used for OGIP Estimation.....	65

List of Figures

Figure 1. Regional Base Map	2
Figure 2. Stratigraphic Column and Type Log.....	3
Figure 3. Detailed Basemap	6
Figure 4. Unit 2A Core Samples	11
Figure 5. Unit 2B Core Samples.....	13
Figure 6. Unit 2C Core Samples.....	15
Figure 7. Correlation using DTA.....	20
Figure 8. Core-Defined Lithofacies.....	26
Figure 9. Cross-plot of Porosity and Permeability	27
Figure 10. Comparison of Electrofacies Classifications	29
Figure 11. 3-D Stratigraphic and Structural Framework.....	34
Figure 12. Vertical Proportion Curve.....	37
Figure 13. 3-D Lithology Model	39
Figure 14. Vertical Proportional Curve by Regions.....	40
Figure 15. 3-D Effective Porosity Model.....	43
Figure 16. 3-D Permeability Model.....	44
Figure 17. Pore Volume Distribution	45
Figure 18. Depositional Environments.....	48

Abstract

The Early to Middle Miocene Formation 2 is the main contributor to hydrocarbon production in the Gulf of Thailand. Formation 2 consists of nine key lithofacies deposits in fluvial and tide-dominated deltaic environments. These lithofacies include 1) coal, 2) organic claystone, 3) bioturbated and laminated claystone, 4) heterolithic sandstone, 5) parallel-laminated sandstone, 6) ripple cross-laminated sandstone 7) cross-bedded sandstone, 8) structureless sandstone, and 9) conglomerate. Two methods of electrofacies classification were used to estimate rock types in non-cored wells, including Artificial-Neural Networks (ANNs) and K-means clustering. For mapping purposes, lithofacies are combined into four lithologies:

1) coal, 2) claystone, 3) heterolithic sandstone, and 4) sandstone. Using ANNs classification with an overall accuracy of 85%, lithology logs were estimated to establish a sequence-stratigraphic framework and to map reservoir properties.

Formation 2 strata form a subset of a large first-order transgressive sequence that includes the underlying Formation 0, Formation 1, and the overlying Formation 3. Formation 2 stratigraphic framework consists of five third-order stratigraphic cycles named, from deepest to shallowest, units 2A-E. The moderate eustatic sea-level rise approximately 19 Ma resulted in a variety of depositional environments, facies distributions, and their reservoir properties. Units 2A-C represent a continuous transgression and landward shift of facies. The top of unit 2C possibly indicates the maximum landward extent of the shoreline. Unit 2D records a major regression and basinward shift of facies resulting from the combination of a glacio-eustatic sea-level fall and tectonic uplift in this region.

Three-dimensional reservoir models illustrate the spatial distribution of lithology, porosity, permeability, and pore volume of the fluvial and tide-dominated deltaic deposits. Sandstone percentage and reservoir quality directly relates to the regressive cycle, unit 2D, while transgressive cycles 2A-C exhibit lower sandstone content and reservoir quality. A combination of the stratigraphic variability of fluvial and deltaic sandstones and fault compartmentalization control hydrocarbon accumulation.

Introduction

The Malay Basin, within the Gulf of Thailand (Figure 1), is a Paleogene intra-cratonic basin that contains a thick succession of alluvial, fluvial, and marginal-marine sediments (Madon et al., 2006). Hydrocarbons were first discovered in the Gulf of Thailand in 1973, and the Malay and Pattani basins are the major hydrocarbon producers (Polachan, 1986). Two significant petroleum systems are present in the Malay Basin, including the deeper Oligocene fluvial-lacustrine deposits and the shallower Miocene fluvial-deltaic deposits (Figure 2). Of all these deposits, the Early to Middle Miocene Formation 2 has been the most favorable target for hydrocarbons production (Carney et al., 2008) that is primarily represented by gas and condensate with various amounts of CO₂. The combination of structure and stratigraphy provides efficient trapping mechanisms for hydrocarbon accumulations.

Leo (1997) divided Formation 2 at Bongkot Field into five major lithostratigraphic units named, from oldest to youngest, units 2A-E, using well-log characteristics, lithology classification, and seismic-amplitude maps. Formation 2 exhibits an overall regressive deltaic sequence with interbedded sandstones, shales, and coals, with sediment supplied by the paleo Chao Praya River.

Madon (1999a) established a stratigraphic framework for the Malay Basin. The stratigraphic framework is linked to three main phases of the basin structural evolution, including pre-, syn-, and post-rift. The Early to Middle Miocene interval was a post-rifted phase with a fluctuation of sea level, causing a cyclical succession of facies patterns. Madon (1999a) defined stratigraphic units A-C, which were formed as a retrogradational marine to deltaic deposits, during a relative rise of sea level.

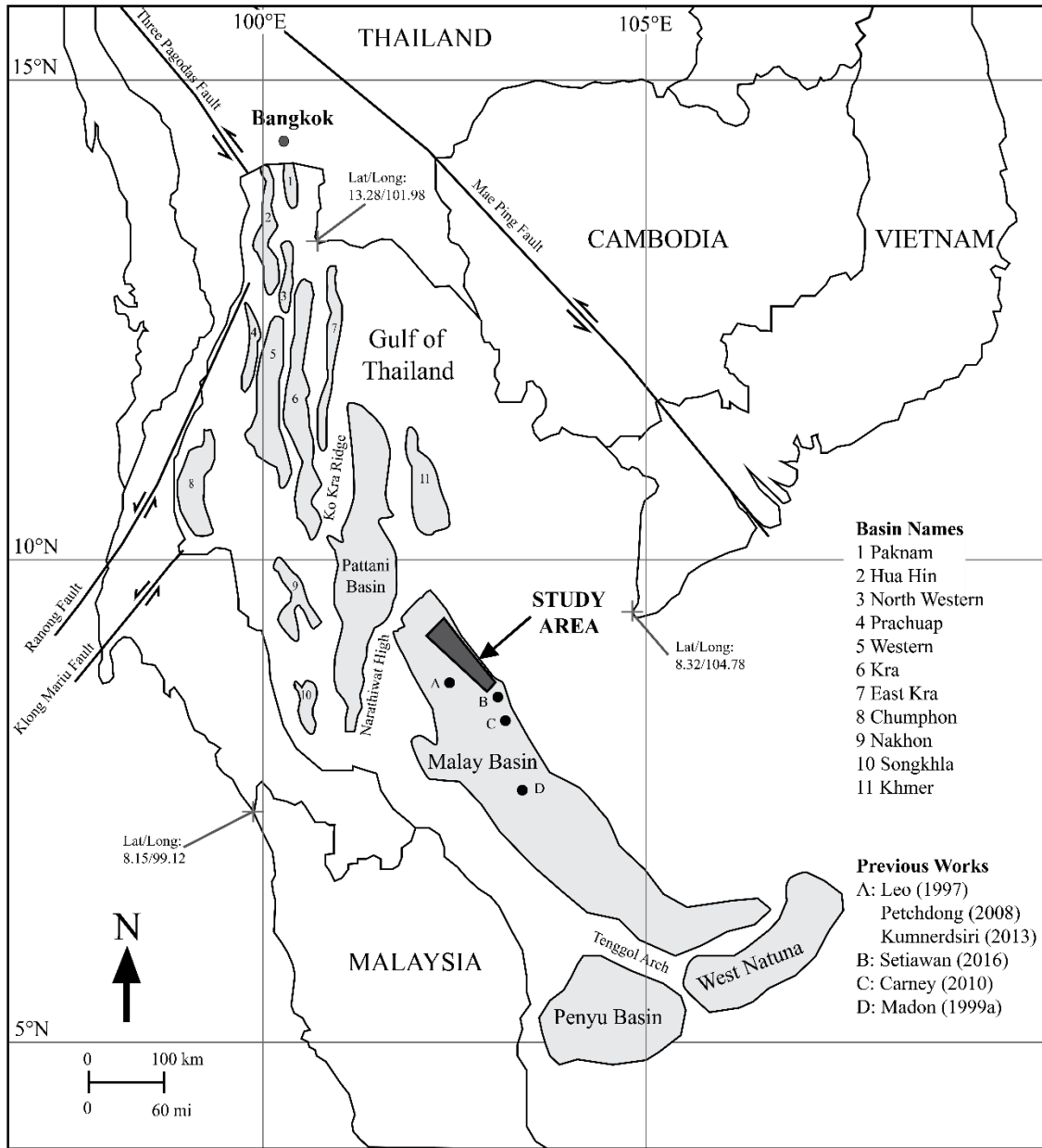


Figure 1. Regional base map showing the Paleogene intra-cratonic basins across the Gulf of Thailand through the offshore area of Malaysia. The study area is in the northern part of Malay Basin (modified from Madon et al., 1999; Watcharanantakul and Morley, 2000; Morley, 2011).

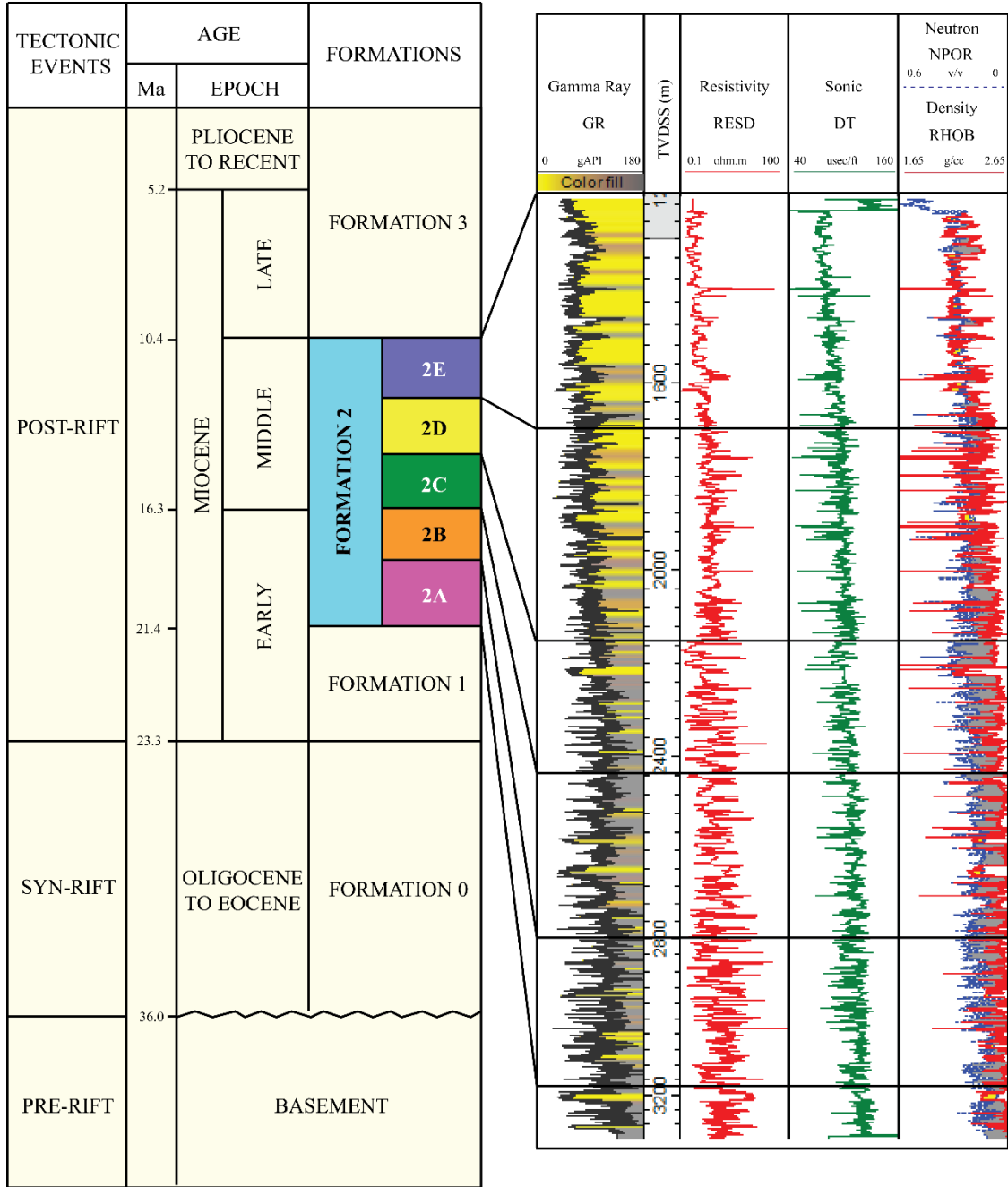


Figure 2. Generalized stratigraphic column tied to a type log of the Early to Middle Miocene Formation 2 interval (modified from Leo, 1997). The GR curve is filled by an interpretive color, which represents lithology. The yellow color indicates crossover between RHOB and NPOR logs, while the gray color presents no-crossover.

Furthermore, units D-E were deposited as progradational fluvial and estuarine channels that were formed during a relative fall of sea level and local tectonic uplifting.

Using core samples and borehole-image logs at Bongkot Field (Figure 1), Petchdong (2008) defined lithofacies and facies associations to interpret tidal channels, tidal sand flats, and tidal mud flats of lower delta-plain to delta-front settings for Formation 2. Prior to this time, Formation 2 was thought to consist of fluvial-dominated deposits.

Carney (2010) identified three major lithofacies for the Miocene-Pliocene reservoirs in block PM301, Malaysia (Figure 1). The integration of depositional models, stratigraphic framework, lithofacies, and petrographic data were used to identify sandstones, mixed sandy/muddy heterolithics, and mudstone-dominated facies. Detrital clay occurred as matrix shale, laminar shale, and dispersed shale and is believed to be a key control of reservoir quality.

Kumnerdsiri (2013) expanded on the work of Petchdong (2008) and examined the depositional environment of the middle Miocene interval at Bongkot Field. Kumnerdsiri (2013) used core-defined lithofacies and well logs to define ten upward-coarsening successions, consisting of mudstone, heterolithic sandstone, sandstone, and coal. Heterolithic sandstone contains cross-bedded sandstones with abundant mudstone drapes; thus, suggesting a tidal influence. Based on the facies associations, the middle Miocene interval was interpreted as a deltaic environment, where the fluvial and tidal processes interacted with each other near the shoreline.

Setiawan (2016) interpreted the tide-dominated deltaic deposits for the Middle to the Late Miocene interval in the Malaysia-Thailand Joint Development Area (Figure

1) using cores, well logs, and seismic attributes (RMS attributes). These data illustrate possible tidal-bar geometries that correspond to the upward-coarsening successions with extensive interbedded sandstones and shales.

To expand upon these previous studies of the depositional environment and reservoir properties, this study explores the sequence-stratigraphic and facies controls on reservoir quality and productivity of Formation 2. The study area targets the northern part of Malay Basin within the Gulf of Thailand (Figure 1). Data include digital logs for 56 exploration wells and 86 development wells and include gamma ray (GR), deep resistivity (ILD), sonic (DT), neutron-porosity (NPOR), and bulk density (RHOB). There are six cored intervals from four wells (Figure 3) representing three units, 2A-C. The 3-D seismic data covers a 3-D reservoir modeling area of approximately 770 km² (297 mi²). Moreover, these data include core porosity, permeability data, and photomicrographs of thin sections. Using these data, this study 1) identifies the key lithofacies and facies associations to evaluate and interpret the depositional environment, 2) classifies lithologies in non-cored wells, 3) establishes a stratigraphic and structural framework, 4) constructs 3-D reservoir models of lithology, porosity, permeability, and 5) relates lithology and reservoir quality distribution to the sequence stratigraphy.

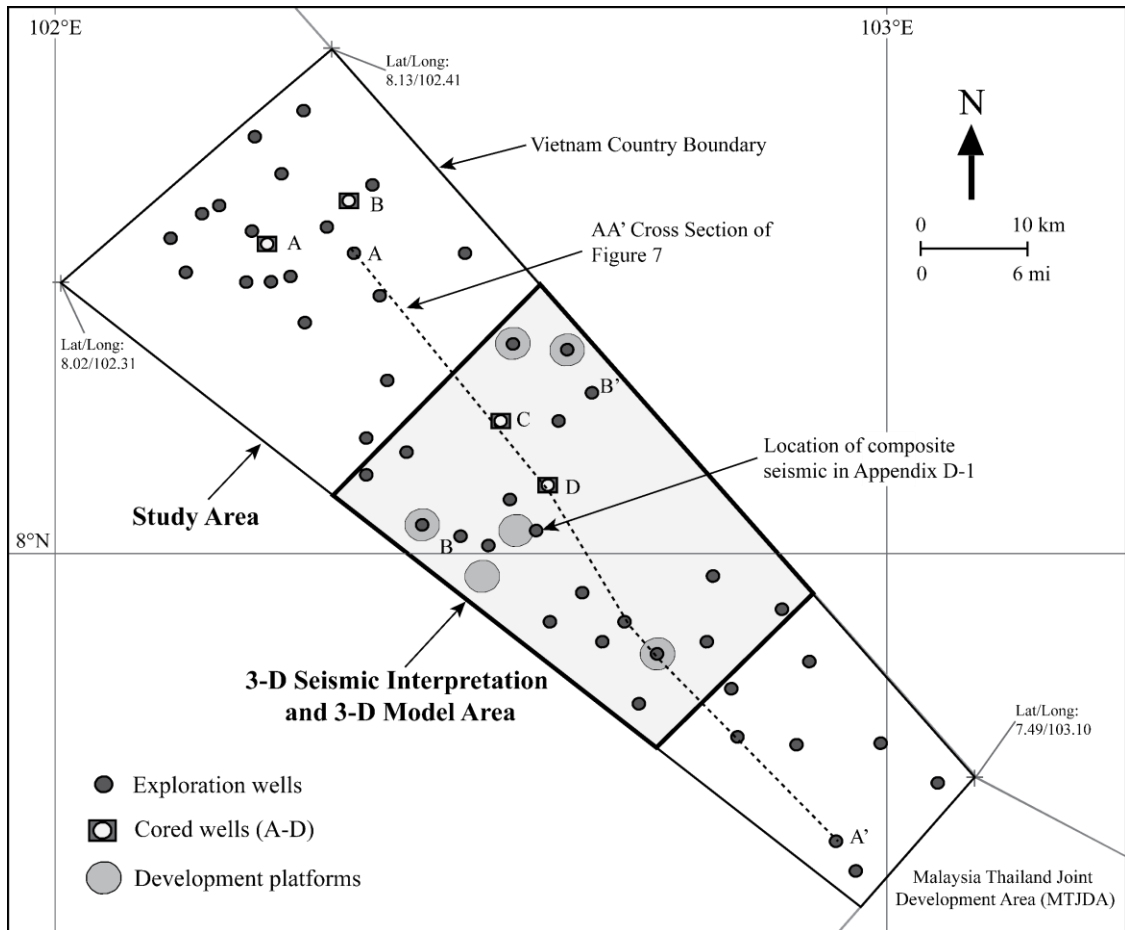


Figure 3. Detailed study area showing the location of 52 exploration wells, 4 cored wells (A-D), 6 development platforms (86 development wells), study area, 3-D seismic interpretation area, and 3-D model area.

Geological Setting

The Malay Basin is a Paleogene intra-cratonic basin, which has an elongated NW-SE trending geometry and is approximately 500 km (310 mi) long and 250 km (155 mi) wide. The basin is bounded on the northwest by the Narathiwat basement high and on the south by the Penyu and Natuna basins (Madon et al., 1999b).

The major collision that occurred between the Indian and Eurasian plates during the Middle Eocene was the principal cause of basin development in Southeast Asia (Pubellier and Morley, 2014) as shown in Appendix A-1. An escape tectonic model, which was initially proposed by Tapponnier (1982) and later revised by Morley (2001), provides an important concept about the clockwise rotation of Indochina continental crust to the southeast and the development of the major strike-slip faults in the eastern part of Asia. Plate movement in a clockwise direction and strike-slip fault activation resulting from the collision between two continental plates developed the formation of rift basins in Southeast Asia (Morley, 2001). The strike-slip movement of the NW-SE Three Pagodas Fault and NE-SW Klong Mariu Fault (Figure 1) during the Middle Eocene corresponded to a major collision event that led to the opening of the Malay Basins. The structural evolution of the Malay Basin first developed in the southern part of the basin by opening in a north-south direction with the development of east-west trending normal faults. The lateral motion of these strike-slip faults significantly decreased during the Early Oligocene, while the east-west trending extension initially developed from the Early Oligocene to Early Miocene. Changes in stress direction produced north-south trending faults superimposed on the older east-west trending faults (Madon, 1995). A significant change in stress regime took place around the Late

to Middle Miocene, when the basins experienced compression by developing an inversion structure, especially in the central part of the Malay Basin. From the Late Miocene until recently, the basin extension stopped and changed to subsidence because of sediment loading (Madon, 1997).

The stratigraphy of the Malay Basin was divided into four lithostratigraphic formations (Figure 2), which are related to basin evolution and sea-level cycles. 1) During the Eocene to Late Oligocene, the oldest syn-rift section, Formation 0, developed with pure extension tectonics. It was restricted to isolated half-grabens and lies unconformably on basement rocks. The syn-rift sediments were dominated by alluvial fan, braided stream, and lacustrine deposits with an increase of lacustrine influence toward the basin center. 2) The Late Oligocene to Early Miocene Formation 1 was marked as an early post-rift period (Morley and Westaway, 2006) with falling of the eustatic sea level due to the last glacial maximum and thermal subsidence. Sedimentation consists of alluvial plain red-beds including fluvial channel and floodplain deposits. 3) The Early to Middle Miocene Formation 2 was controlled by a changing of the eustatic sea level from a slow rising to a falling level (Appendix A-2). The depositional environment gradually changed from fluvial-dominated to a marginal-marine setting that was characterized by a large deltaic system (Appendix A-3). Then, the entire basin sagged downward and was covered by shallow-marine sediments during the Late Miocene to Early Pliocene Formation 3; then regional subsidence resumed and fully open-marine conditions now exist across the Gulf of Thailand.

Methods

Lithofacies and Lithology Description and Electrofacies Classification

The major lithofacies of Formation 2 were determined using six cored intervals covering 182.5 m (598.8 ft) from 4 wells (Figure 3). The detailed core description includes lithology, color, grain size, sorting, rounding, sedimentary structures, bounding surfaces, bioturbation index, and stacking patterns (Appendix B-1). Figures 4 to 6 illustrate a schematic core description in units 2A-C, respectively.

Electrofacies classification for lithofacies and lithology was analyzed using Artificial-Neural Networks (ANNs) and K-means clustering techniques with different well-log inputs. This process aimed to classify and predict rock types for lithology log in non-cored wells.

ANNs was performed as a supervised classification consisting three layers, including the input layer, hidden layer, and output layer, which were called the Feed-Forward Artificial-Neural Networks (FF-ANNs). These networks will propagate the information or data in only one direction and learn to recognize the relationship between inputs and outputs (Ashena and Thonhauser, 2015)

K-means clustering is an unsupervised technique that groups the similar characteristics of data points into the same clusters (Kanungo et al., 2002; Antonenko et al., 2012). The objects within the same cluster are internally more homogeneous to each other than to those are in other clusters. This technique has to define the number of clusters (K) that is equivalent to the number of centroids for its cluster. In general, K should be equal to the number of rock types observed in the core samples. However, as the core samples might not represent all the rock types, statistical approach will be used

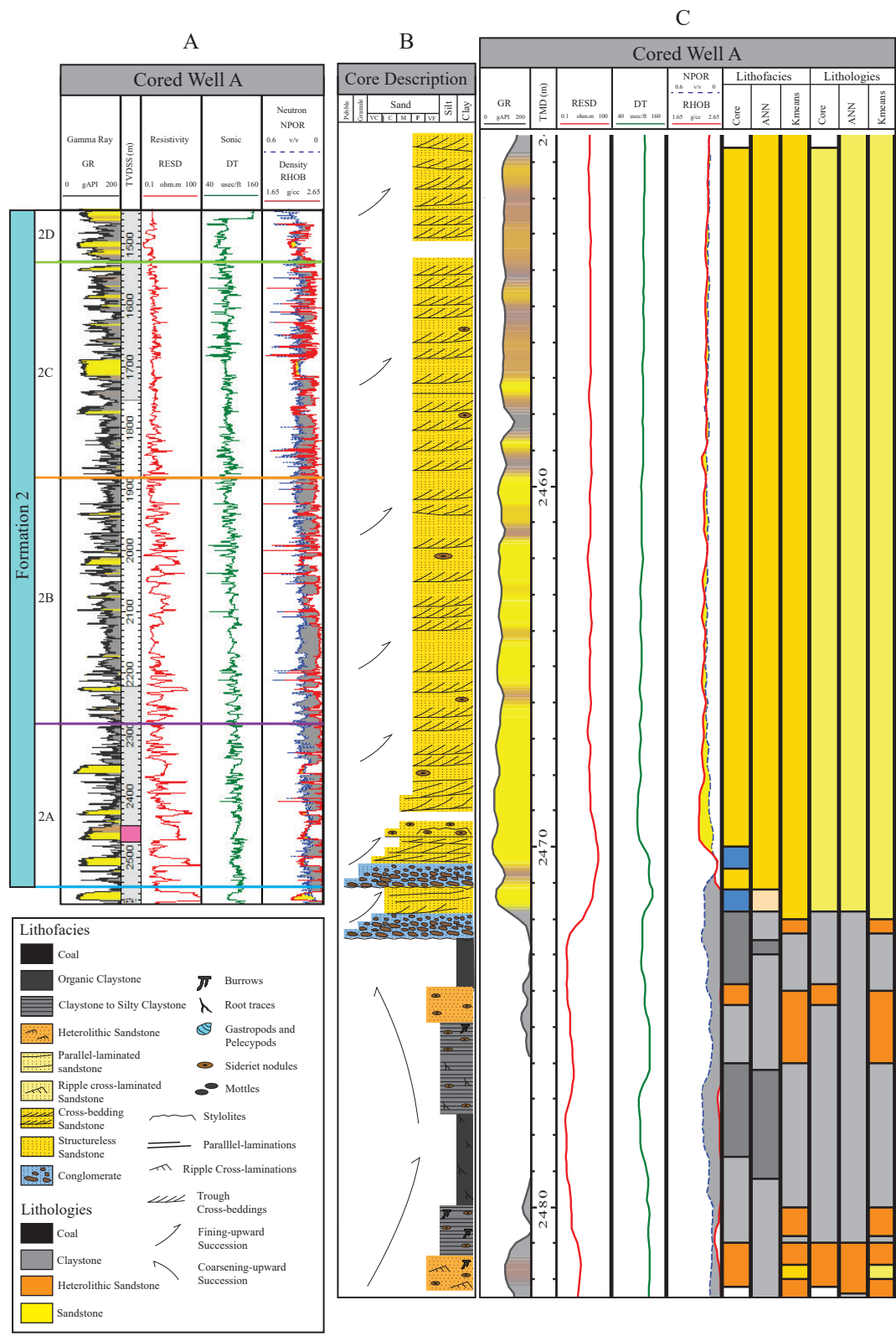


Figure 4. A) Gamma-ray (GR), deep-resistivity (RES), neutron porosity (NPOR), and bulk density (RHOB) well-log responses for the cored well A in unit 2A. The pink bar indicates the cored interval. The GR curve is filled with an interpretive color to represent lithology. The yellow color highlights crossover between NPOR and RHOB logs, while the gray color indicates no crossover. B) Schematic core description from cored well A. The cored interval has a fining-upward pattern from the conglomerate at the bottom to the cross-bedded sandstone at the top. C) Gamma-ray (GR), deep-resistivity (RES), neutron porosity (NPOR), and bulk density (RHOB) well-log responses for the cored interval. Conglomerates do not have a crossover between NPOR and RHOB logs and they have slightly higher gamma-ray and resistivity values than sandstones. Sandstones have a moderate crossover between NPOR and RHOB logs with slightly lower gamma-ray. The right track shows lithofacies and lithologies observed in core samples and predicted by ANNs and K-means clustering techniques, respectively.

Figure 5. A) Gamma-ray (GR), deep-resistivity (RES), neutron porosity (NPOR), and bulk density (RHOB) well-log responses for the cored well B in unit 2B. The pink bar indicates the cored interval. The GR curve is filled with an interpretive color to represent lithology. The yellow color highlights crossover between NPOR and RHOB logs, while the gray color indicates no crossover. B) Schematic core description from cored well B. The cored interval illustrates a fining-upward pattern from cross-bedded sandstone at the bottom to ripple cross-laminated sandstone, heterolithic sandstone, and laminated and bioturbated claystone at the top. C) Gamma-ray (GR), deep-resistivity (RES), neutron porosity (NPOR), and bulk density (RHOB) well-log responses for the cored interval. Cross-bedded sandstone is recognized by slight crossovers between NPOR and RHOB logs and it has a significantly lower gamma-ray value than heterolithic sandstone and claystone. Ripple cross-laminated sandstone and heterolithic sandstone have slightly higher gamma-ray value with no crossovers between NPOR and RHOB logs. The right track shows lithofacies and lithologies observed in core samples and predicted by ANNs and K-means clustering techniques, respectively.

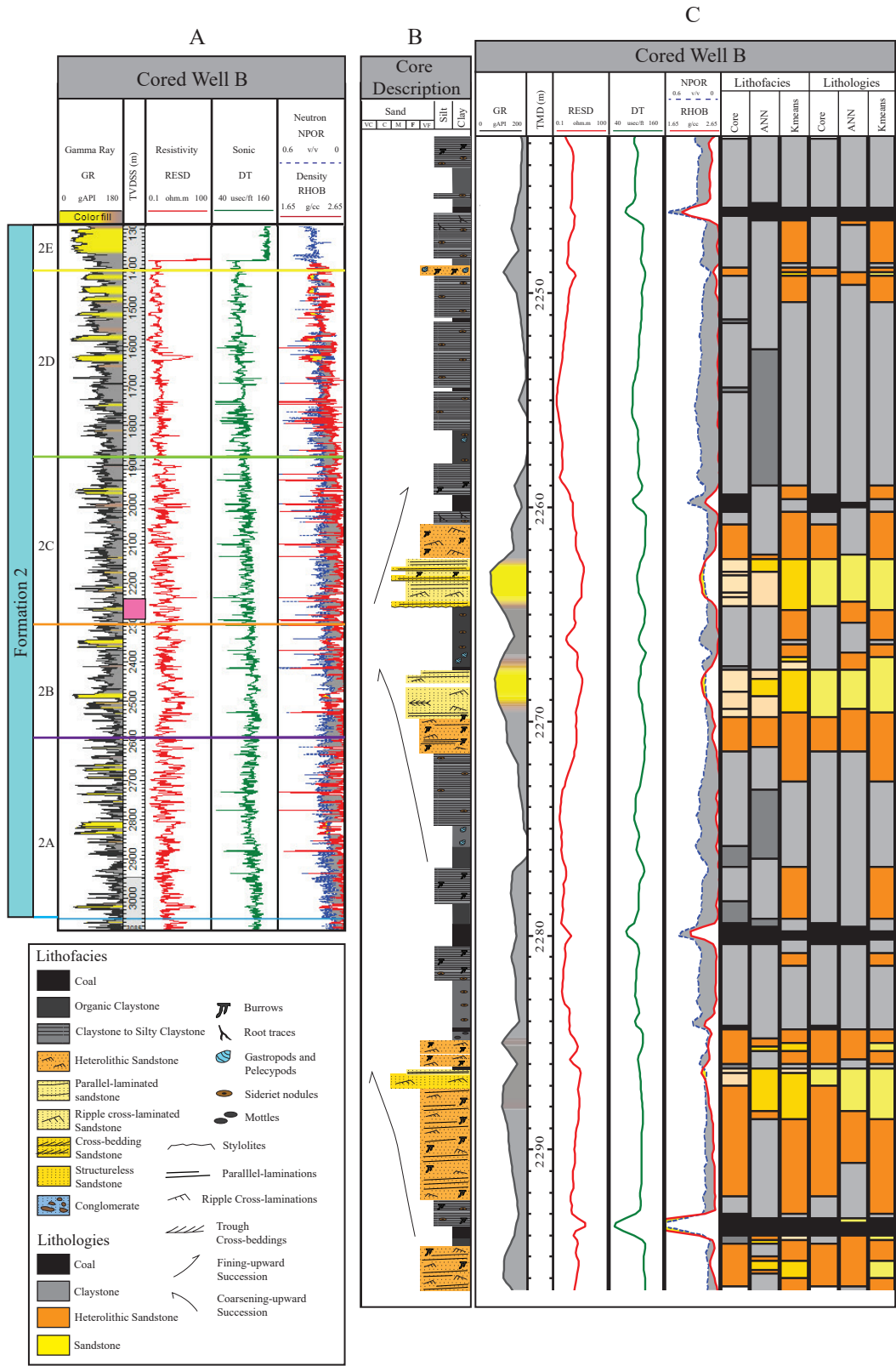


Figure 6. A) Gamma-ray (GR), deep-resistivity (RES), neutron porosity (NPOR), and bulk density (RHOB) well-log responses for the cored well B in unit 2C. The pink bar indicates the cored interval. The GR curve is filled with an interpretive color to represent lithology. The yellow color highlights crossover between NPOR and RHOB logs, while the gray color indicates no crossover. B) Schematic core description from cored well B. The cored interval consists of two coarsening-upward patterns that grade from claystone at the base to ripple cross-laminated sandstone at the top. Then, it can be observed the change from medium-grained sandstone with mud laminations at the base to heterolithic sandstone and claystone at the top demonstrates a fining-upward pattern. C) Gamma-ray (GR), deep-resistivity (RES), neutron porosity (NPOR), and bulk density (RHOB) well-log responses for the cored interval. Cross-bedded sandstone has slight crossovers between NPOR and RHOB logs with a significant lower gamma-ray value than heterolithic sandstone and claystone. Overall, ripple cross-laminated sandstone has slight crossovers between NPOR and RHOB logs and moderate low gamma-ray values, while the other lithofacies do have relatively high gamma-ray values without any crossover between NPOR and RHOB logs. The right track shows lithofacies and lithologies observed in core samples and predicted by ANNs and K-means clustering techniques, respectively.

by plotting the sum of squared distances within the centroid (SSW) and the sum of squared distances between the centroid (SSB) against the number of clusters (K). The optimum K can be defined from the elbow point that shows a significant decrease in the distances, and in which the number of clusters in this study was set at 9 (Appendix B-4).

The accuracy of electrofacies classifications was determined by comparing the estimated rock types with core-defined rock types in a confusion matrix (Ting, 2011). The predicted classes were assigned in columns and the actual classes were given in rows, which the confusion matrices showed in numbers of correct and incorrect classifications (Appendices B-5 through B-12). Overall accuracy was obtained by dividing the total number of correctly predicted classes with the total number of predicted classes. Similarly, the accuracy of individual classes, known as a user's accuracy, was calculated by dividing the number of correct predictions for each class with the total number of each class. To select between ANNs and K-means methods with various well-log combinations, their overall accuracy and user's accuracy were compared. In addition, the number of wells containing each well-log combination needs to be considered, as these wells were acquired with different well-log configurations. Therefore, a balance is needed between using the most well-log inputs and ensuring representative data coverage. In this study, three cored wells, A, C, and D, were assigned as a training data set, whereas cored well B was used to validate predicted classes from ANN and K-means clustering techniques (Figures 5 and 6).

Depositional Environment

The depositional environment of Formation 2 was interpreted based on the lithofacies characteristics and their vertical associations as described in the core samples. The specific features, including grain sizes, sedimentary structures, bioturbations, and bounding surfaces in all lithofacies, were considered to define the sedimentary processes and determined the depositional setting that could make those processes. The vertical facies associations were analyzed to identify the relationship on how lithofacies change from one to another because the different lithofacies associations also reflect different depositional environment settings. In addition, the coarsening-upward or fining-upward facies successions can be used to recognize some depositional environments. These informational data were integrated to develop several hypotheses for depositional environment interpretation.

Stratigraphic and Structural Framework

A stratigraphic and structural framework of Formation 2 was developed to gain a better understanding of the variability in lithology and reservoir quality related to stratigraphic sequences and to identify the key markers for well-log correlation.

The Formation 2 interval was subdivided into five major stratigraphic units named, from deepest to shallowest, 2A-2E, based on their potential cyclicity (Leo, 1997). A stratigraphic and structural framework of Formation 2 was established by correlating well logs from 142 wells: each well having at least gamma ray (GR), deep resistivity (RESD), neutron porosity (NPOR), and bulk density (RHOB). Then, 3-D seismic data was tied to well-defined flooding surfaces of each stratigraphic cycle for horizons interpretation and depth structural-maps conversion.

Description of the top and base of Formation 2 were guided by the changing in cutting's colors based on the depositional environments as observed in the mud-log data. The top of Formation 2 was identified when cuttings change from the green color of the shallow marine deposits in Formation 3 to a gray color, while cuttings changing from the gray to a reddish-brown color of fluvial-dominated deposits in Formation 1 corresponds to the base of Formation 2.

The stratigraphic framework of Formation 2 was characterized by multiple cycles of stacked lithologies based on the changes in accommodation space resulting from the relative changes in sea level and sediment supply. Lithology logs resulting from electrofacies classification also reveal the cyclical patterns of stacked lithologies. The increase-upward in claystone content corresponds to a fining upward succession, while the increase-upward in sandstone content suggests a coarsening-upward succession.

A type of log-attribute analysis called Derivative-Trend Analysis (DTA) was conducted with commercial software using GR logs in every well to highlight well-log signatures that are normally hard to observe from within the actual measurement values (Appendix C-1). The DTA process consists of two main steps. The first step is to define an appropriate window for GR smoothing (Guo, 2011). The second step is to differentiate how the smoothed GR curve changes by using the central-difference method (Wethington, 2017). In this study, low GR values indicate sandstone while high GR values represent claystone. An upward-decrease of GR values suggested cleaning-upward patterns with a decrease in clay content resulting in a positive DTA. In contrast,

an upward-increase of GR values showed a fining-upward motif with an increase in clay content resulting in a negative DTA (Figure 7).

Resulting from the facies successions and stacking patterns, the sequence-stratigraphic cycles of Formation 2 were defined as likely to separate by flooding surfaces. These key flooding surfaces relating to claystone lithology were distinctive in the well-logs with higher GR, lower RESD, and larger separation between NPOR and RHOB. Furthermore, these surfaces can be recognized and correlated using DTA curves that change from a negative to a positive trend. The flooding surfaces were of lateral continuity and they could be correlated across the study area (Figure 7). Given this information, these flooding surfaces were assigned to be the top of stratigraphic units 2A-D.

The 3-D seismic data fully covering the 3-D modeling area (Figure 3) was acquired by Fugro M/V Geco Sapphire in 1998. It was re-processed many times to decrease migration artifact, minimize fault shadow effect, and improve reflection continuity at the reservoir target. The 3-D seismic volume shows in the time domain with a reverse polarity, in which the trough is a positive reflectivity (+RC) and the peak is a negative reflectivity (-RC). Wells with check-shot data (N=28) were tied to a seismic time-volume using commercial software (Appendix C-2) to generate a time-depth correlation. For mapping purposes, five key surfaces, including Formation 1 and Formation 2 (units A-D), were interpreted. The interpreted faults provided by PTTEP were checked and their accuracy was validated. Well-tops were used to estimate average velocities for time-to-depth conversion of both horizons and fault surfaces.

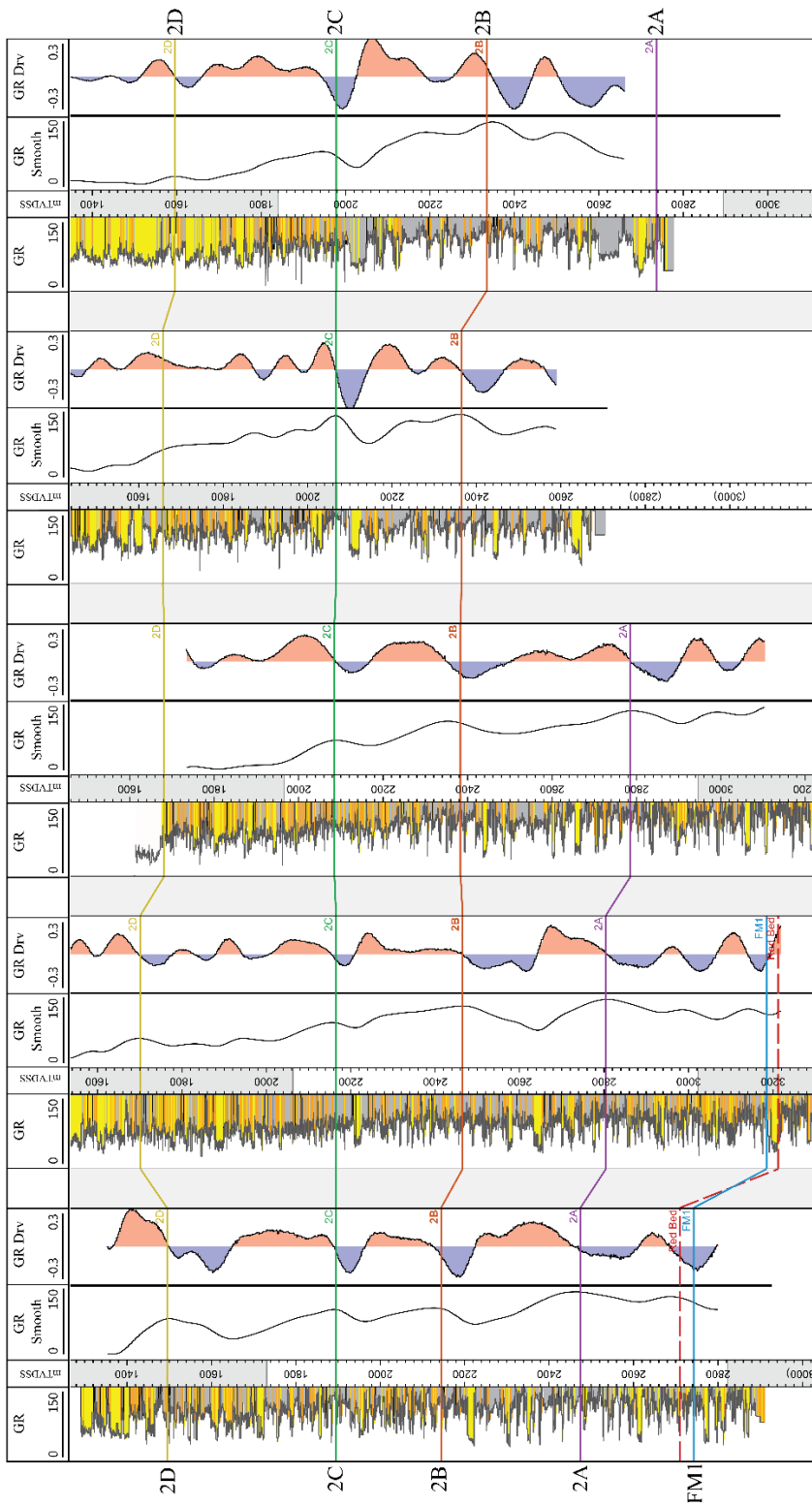


Figure 7. Example of well-log correlations guided by GR derivative curves. Refer to Figure 3 for the location of the cross section. The first track on the left is the regular GR track filled by lithology log resulted from electrofacies classifications, which color legend can be found in Figure 4-6. The second track is the GR after a gaussian smoothing filter, with a 120 m (390 ft) window applied. The third track is the GR derivative with a red fill for positive values (GR is decreasing or cleaning upward) and a blue fill for negative values (GR is increasing or fining upward). The tops of the units named, 2A-D, are picked at the transition on GR derivative curve that changes from the negative to positive trends.

The depth surfaces and major faults were used to construct a 3-D stratigraphic and structural framework (3-D grid) for reservoir modeling (Appendix C-4). The RMS amplitude of seismic data was analyzed to generate the sandstone probability maps for lithology model. However, the relation between sandstone lithology and acoustic impedance (AI) value was not confirmed by a cross-plot of AI versus the effective porosity (Appendix C-5). Referring to a cross-plot, all lithologies, including coal, claystone, heterolithic sandstone, and sandstone, were overlapped with each other at the same AI values. Therefore, the probability maps derived from RMS amplitude were not represented to sandstone lithology for constraining the lithology model.

Spatial Distribution of Lithology, Porosity, Permeability, and Pore Volume

Model Grid

The 3-D model grid includes 4 stratigraphic zones representing units 2A-D and covers about 770 km² (297 mi²) with an aerial cell size of 150 m × 150 m (492 ft × 492 ft). There are 680 layers made by the proportional layering scheme to the reference depth surfaces. In total, the 3-D model grid cell dimensions are 254 × 258 × 680 and contain approximately 45 million cells.

Lithology Models

The lithology model was created using a Sequential-Indicator Simulation (SIS) to model the spatial distribution of four lithologies (coal, claystone, heterolithic sandstone, and sandstone) with the following data and constraints: 1) stratigraphic and structural framework; 2) upscaling lithology logs (N=94); 3) 1-D vertical proportional curve of lithologies; 4) input histogram of lithology percentages in each zone; and 5)

variogram parameters. The vertical variogram ranges were mostly estimated from the vertical wells, while the horizontal ranges were estimated using the 2-D variogram maps (polar plots) generated by zones for each lithology to determine the major and minor anisotropy ranges (Appendix D). The major azimuth was parallel to the direction of the sedimentary supply from the paleo Chao Praya River (Appendix A-3). The experimental variograms, ranges for each lithology and zones are concluded in Table 1.

Petrophysical Models

The effective porosity as provided by PTTEP was modeled using a Sequential-Gaussian Simulation (SGS) with the following data and constraints: 1) lithology model; 2) upscaling effective porosity logs biased to lithology logs (N=94); 3) input histogram of porosity distributions for each lithology; and 4) variogram parameters. The variogram ranges for petrophysical properties were smaller than the lithology model to capture the internal heterogeneity within each lithology as summarized in Table 2.

The permeability model was additionally constrained to the effective porosity model as a secondary variable using a collocated co-kriging method (co-variance) with a constant coefficient of 0.84 derived from a correlation between porosity and permeability (Figure 9). The co-kriging method has been commonly applied when the main attribute lacking well data, but the related secondary attribute has abundant constraining wells (Tavakkoli, 2010). Only sandstone and heterolithic sandstone were modeled with the output range as summarized in Table 2. Coal and claystone lithologies have a very low permeability; therefore, their permeability were assigned at 0.

Pore volume distribution

Pore volume distributions deriving from lithology and porosity models were analyzed for 100 realizations, which each of them was varied by changing the iteration numbers between 10,000-20,000. Then, the pore volume in each case was combined and calculated by using Monte-Carlo simulation to generate the distribution range in each stratigraphic zone and lithology.

Volumetric estimation

The original gas initial in-place (OGIP) was also estimated for one future development platform by using the same defined prospect area, filling ratio, gas saturation (Sg), and gas expansion factor (Bg) as provided by PTTEP. The net reservoirs of sandstone and heterolithic sandstone containing more than 10% porosity were determined from the 3-D lithology model. The equation of OGIP estimation was described as the details below:

$$OGIP (MMscf) = \frac{0.04356 \times \text{Area (m}^2\text{)} \times \text{Net Reservoirs (m)} \times \text{Filling Ratio} \times \phi \times Sg}{Bg}$$

- Filling ratio is the total thickness of net reservoirs divided by the total thickness of net sands in each unit.
- Bg is a function of temperature and pressure resulting from PVT database.
- Sg is the fraction of the pore space occupied by gas.

Results

Formation 2 lithologies and lithofacies

Formation 2 consists of nine lithofacies including 1) coal, 2) organic claystone, 3) laminated and bioturbated claystone, 4) heterolithic sandstone, 5) parallel-laminated sandstone, 6) ripple cross-laminated sandstone, 7) cross-bedded sandstone, 8) structureless sandstone, and 9) conglomerate (Figures 8). Table 3 provides a summary of each lithofacies and Appendix B-2 show the detailed descriptions and lithofacies interpretations. Lithofacies are mostly fine-grained deposits and gradually change from one to another depending upon to the process of deposition.

A porosity and permeability cross-plot of core-plug data (Figure 9) reveals a good relationship between lithofacies and reservoir properties. The high porosity value has a better permeability as observed in the structureless and cross-bedded sandstone, while the low porosity has a low permeability as found in the heterolithic sandstone and claystone. This cross-plot can be grouped into three clusters showing a high, a moderate, and a low reservoir quality. Structureless sandstone and cross-bedded sandstone have a very high porosity and permeability. Their porosity varies from 13 to 25%, while permeability occurs in a wide range from about 3 to 415 mD. Ripple cross-laminated sandstone and parallel-laminated sandstone have a moderate reservoir quality, where the porosity is just about 8-20 % and permeability ranges from 0.05 up to 40 mD. While heterolithic sandstone has the lowest reservoir quality, their porosity ranges from 5-12% and permeability is mostly less than 0.1 mD. Laminated and bioturbated claystone does not contain any significant reservoir properties, as its permeability is generally less than 0.01 mD. Framework grains of Formation 2 is

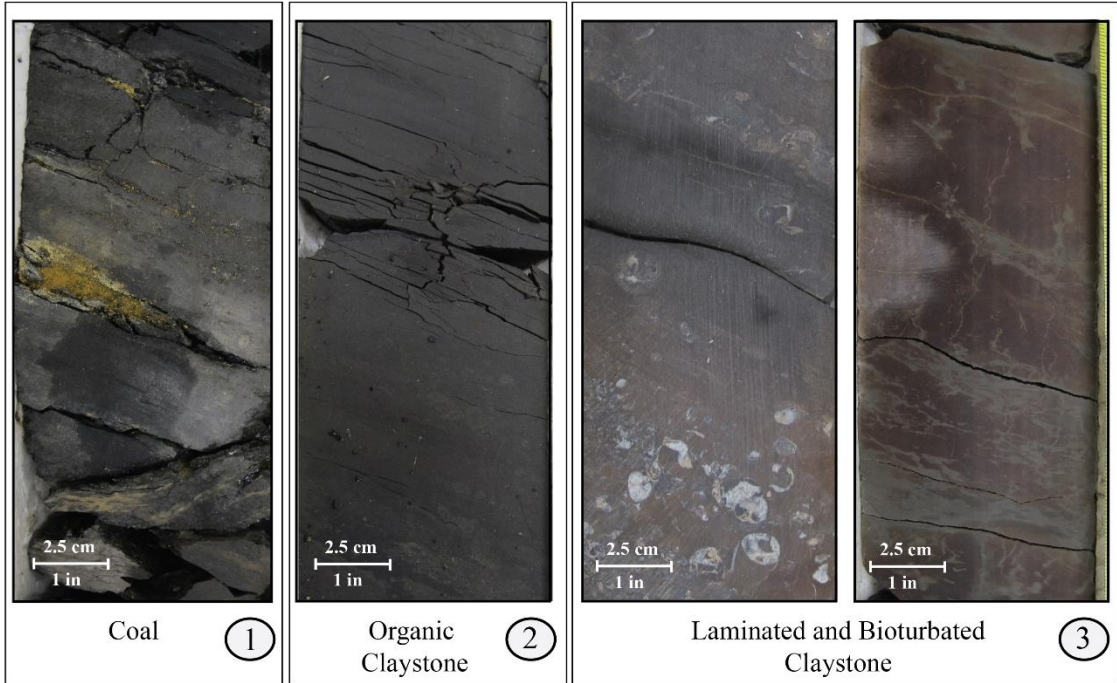




Figure 8. Core-defined lithofacies include 1) coal, 2) organic claystone, 3) laminated and bioturbated claystone, 4) poorly-bedded heterolithic sandstone, 5) parallel-laminated sandstone, 6) ripple cross-laminated sandstone, 7) cross-bedded sandstone, 8) structureless sandstone, and 9) conglomerate.

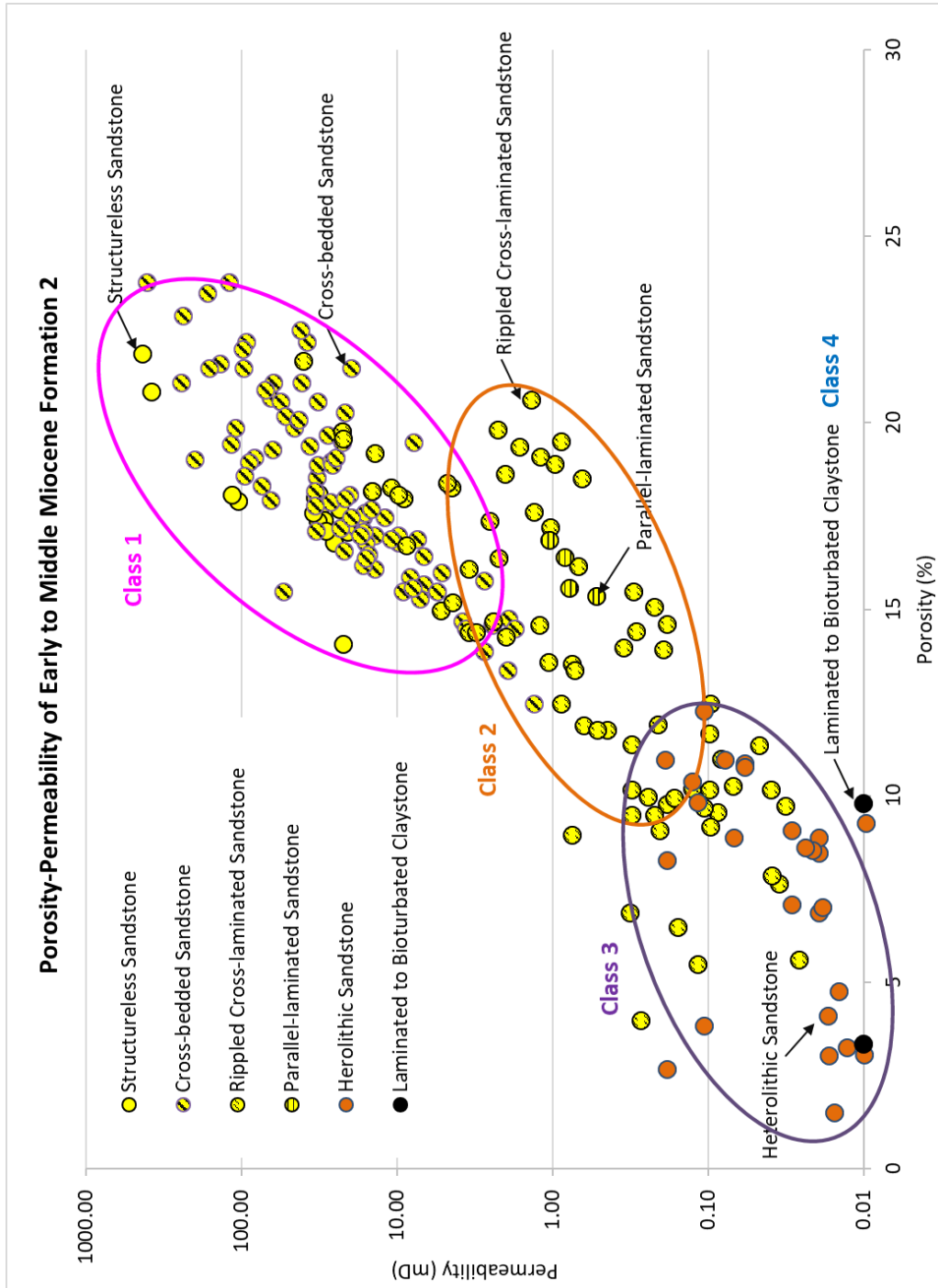


Figure 9. Cross-plot between porosity and permeability measured on a suit of core plugs as colored by core-defined lithofacies

predominantly quartz with common accessory grains and minor rock fragments (Appendix B-3). Clay matrix primarily comprises detrital dispersed clay, kaolinite, and laminar clay. Ferroan dolomite and calcite cement are the most common. Pore structure is an intergranular porosity, which the porosity reduction is caused by compaction, quartz overgrowth, detrital dispersed clay, and ferroan dolomite cement.

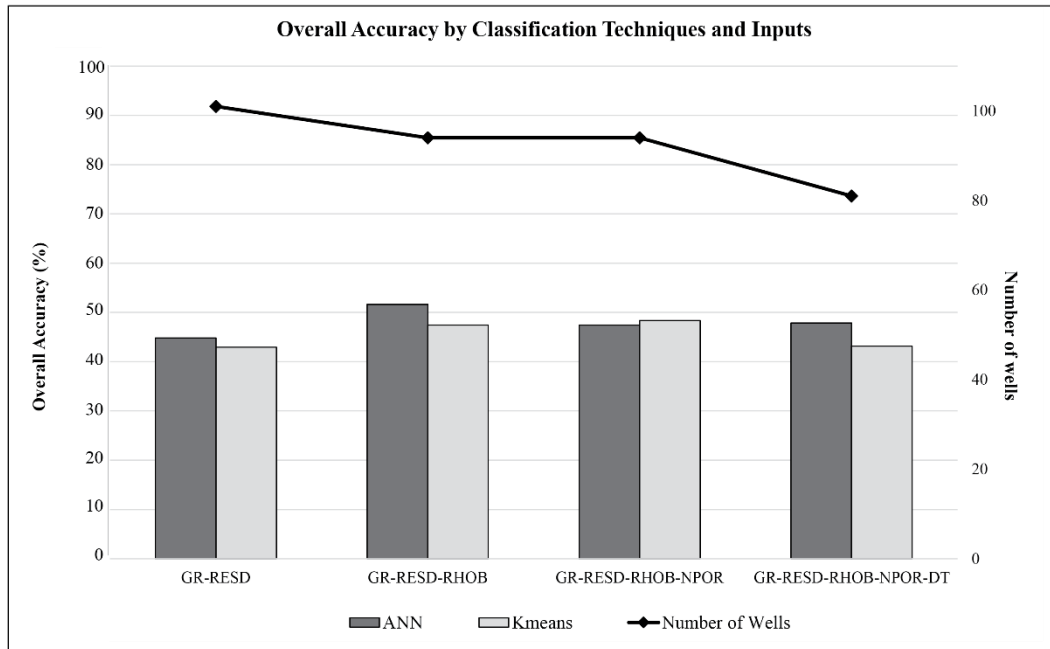
Electrofacies Classification

Lithofacies Classification

Predicting lithofacies through the ANNs achieves the highest overall accuracies with the best case of 52% when using the GR, RESD, RHOB, NPOR, and DT logs (Figure 10). User's accuracies for this case are 56%, 15%, 85%, 43%, 28%, and 25% for only coal, organic claystone, laminated and bioturbated claystone, poorly bedded heterolithic sandstone, ripple cross-laminated sandstone, and cross-bedded sandstone, respectively (Appendix B-8). The ANNs failed to classify parallel-laminated sandstone, structureless sandstone, and conglomerate. The confusion matrix shows that parallel-laminated sandstone is mostly misclassified as a cross-bedded sandstone, while structureless sandstone and conglomerate are predicted as a ripple cross-laminated sandstone. The other well-log assemblages also produce a relatively low overall accuracy of about 47%, while only laminated and bioturbated claystone has the highest individual user's accuracy of more than 70%.

K-means clustering was performed such that the number of clusters (K) was assigned at 9 clusters resulting from a cross-plot between sum of square within (SSW) and sum of square between (SSB) as displayed in Appendix B-4. The highest overall accuracy of K-means clustering is 48% when using the combinations of GR, RESD,

A Lithofacies Prediction



B Lithology Prediction

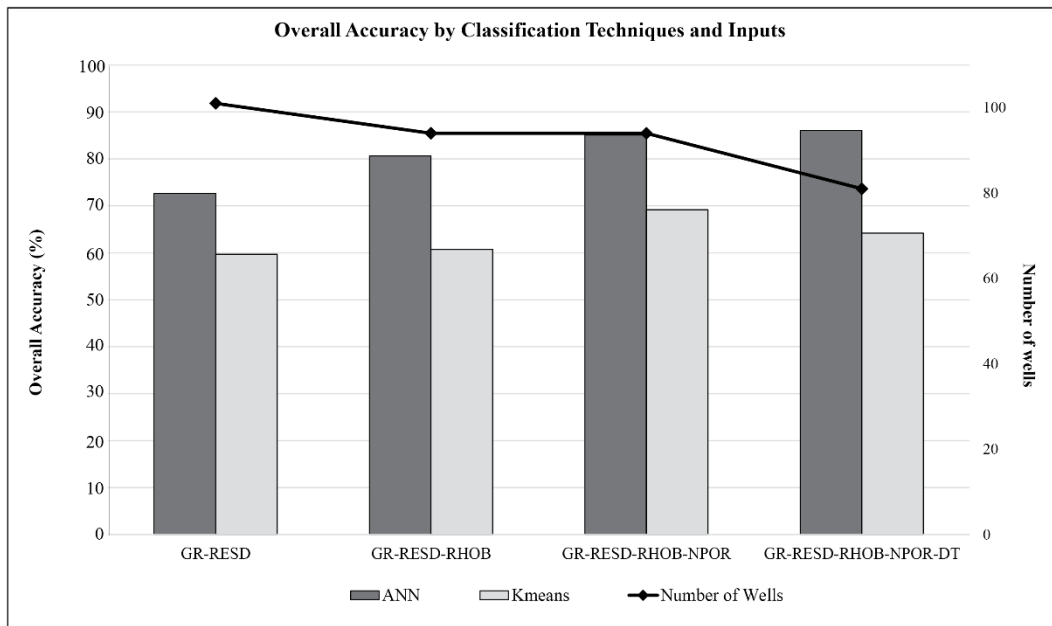


Figure 10. Chart comparing the overall accuracies of A) lithofacies and B) lithologies classification between ANNs and K-means clustering techniques for each set of log curves used as inputs (GR: Gamma Ray; RESD: Deep Resistivity; RHO: Bulk Density; NPOR: Neutron Porosity; DT: Sonic). Diamonds represent the number of wells that contain each set of input. This chart is also used to compare how well each set of input is able to cover the area of study.

RHOB, and NPOR (Appendix B-7). The overall accuracy is slightly higher than for the ANN analysis using the same combination of inputs (47%). User's accuracy is 44%, 57%, 78%, 3%, and 100% for coal, laminated and bioturbated claystone, heterolithic sandstone, parallel-laminated sandstone, and cross-bedded sandstone, respectively. Like the predictions of the ANNs, K-means clustering cannot predict organic claystone, ripple cross-laminated sandstone, structureless sandstone, and conglomerate. A confusion matrix indicates that organic claystone is misclassified as a laminated and bioturbated claystone, while ripple cross-laminated sandstone, structureless sandstone, and conglomerate are predicted as a cross-bedded sandstone. The overall prediction accuracy of the other well-log combinations is relatively consistent, with the lowest case at 43% and the highest case at 47%.

Based on the low overall accuracy achieved, it can be concluded that lithofacies classification using ANNs and K-means clustering techniques is inadequate. Because lithofacies determination relies on core samples, their detailed physical properties can be easily observed including grain sizes, sedimentary structures, bounding surfaces, and minor components. Moreover, the vertical resolution of well-logs is not good enough to capture the detailed variations of lithofacies. Some lithofacies, including parallel-laminated sandstone, ripple-laminated sandstone, and structureless sandstone, are not recognized by the ANNs, which could be attributed to the lack of core-derived lithofacies for training. Because of these reasons, nine lithofacies were grouped into their parent four lithologies: 1) coal, 2) claystone, 3) heterolithic sandstone, and 4) sandstone for further analysis.

Lithology Classification

Using the ANNs for lithology classification provided the highest overall accuracy, with a best case of 86% by using the GR, RESD, RHOB, NPOR, and DT logs (Figure 10). User's accuracies for this case are 78%, 92%, 64%, and 82% for coal, claystone, heterolithic sandstone, and sandstone, respectively. A confusion matrix (Appendix B-8) indicates that heterolithic sandstone is confused with claystone as these two lithologies exhibit very similar characteristics in well-log responses. They tend to grade into one another, which makes them significantly harder to classify without core samples. The lowest overall accuracy predicted by ANNs is 73% when using GR and RESD logs.

The estimated lithofacies by K-means clustering are then lumped into their parent four lithologies to evaluate the accuracy of lithology prediction. The highest overall accuracy is 69% when using the well-log combinations of GR, RESD, RHOB, and NPOR (Appendix B-11). The result was remarkably less than the overall accuracy of the ANNs using the same inputs (85%). User's accuracy is 66%, 71%, 36%, and 79% for coal, claystone, heterolithic sandstone, and sandstone, respectively. The lowest user's accuracy occurs in heterolithic sandstone, which is mainly predicted as claystone and sandstone. This issue is similar to the one resulting from the ANNs prediction, which classified some of the heterolithic sandstones as claystone. Other log combinations of K-mean clustering analysis result in overall accuracies of approximately 60%, which is generally less accurate than the ANNs.

In comparison, the lithology prediction made by the ANNs provides the best overall accuracy, when compared to K-means clustering method. However, the highest

overall accuracy of the ANNs prediction must include the input of GR-RESD-RHOB-NPOR-DT logs, which exist for only 81 wells (Figure 10). To optimize the prediction accuracies and the number of constraining wells, the well-log inputs of GR-RESD-RHOB-NPOR occurring in 94 wells with the overall prediction accuracy of 85% are to be selected to generate lithology logs in non-cored wells.

Stratigraphic and Structural Framework

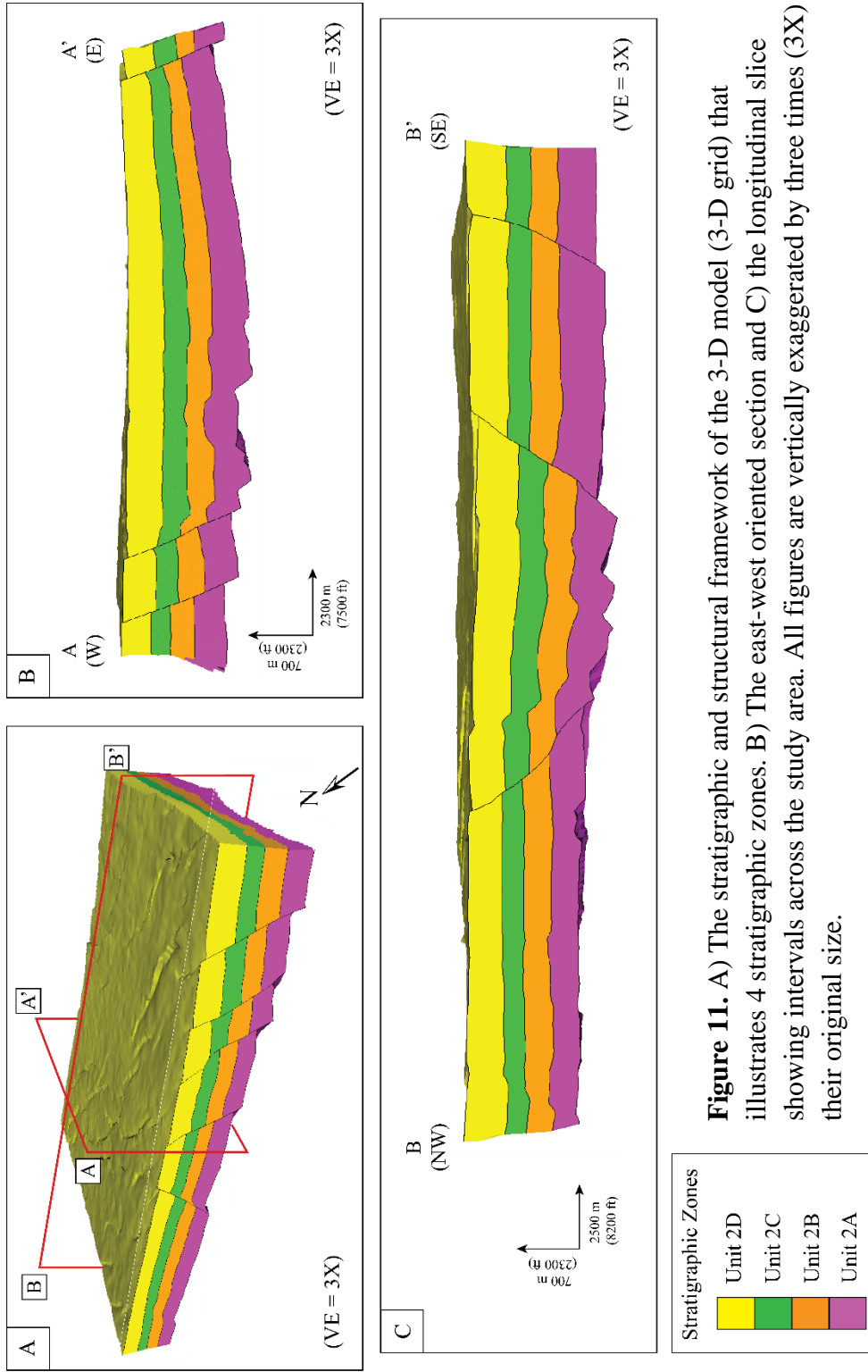
The stratigraphic framework of Formation 2 was established through detailed well-logs correlation guided by lithology logs derived from electrofacies classification and smoothed GR curves and their DTA curves (Figure 7).

The Formation 2 interval was subdivided into five stratigraphic cycles named, 2A-2E, which are separated by key flooding surfaces (FS). The FS corresponding to claystone lithology is characterized on wireline logs by distinct GR, RESD, NPOR, and RHOB values. In addition, FS is identified by the highest value on smoothed GR curves and the sudden change from a negative to a positive trend on DTA curves. In general, these FS are laterally widespread and can be correlated across the study area; consequently, they are assigned to be the reference markers of each stratigraphic unit in well-log correlations.

These key markers, representing the FS of each stratigraphic unit, are tied to seismic data using time-depth correlations from check-shot data (Appendix C-2). In this study, five seismic horizons, representing Formation 1 and Formation 2 (units A-D), are picked at zero phase amplitude (Appendix C-3) and they can be interpreted entirely the 3-D model area (Figure 3). The shallow gases, located near the sea bed, generally interrupt the lateral continuity of seismic reflector and affect the horizons interpretation.

In comparison, the seismic reflectors of units 2B-D have more lateral continuity than unit 2A and Formation 1 as they are in the deeper shallower section with small fault displacement. The interpreted faults provided by PTTEP are also validated during horizons interpretation. These faults can be interpreted at just nearly the top of Formation 1 due to the low seismic resolution in the deeper section. These interpreted horizons and faults are converted from time- to depth-structural surfaces using the estimated average velocities of well tops for a 3-D stratigraphic and structural framework (3-D grid).

The 3-D model occurs as tilted blocks dipping against normal faults oriented in the NNW-SSE direction (Figure 11). The vertical offset of these normal faults gradually increases with depth, but most of them do not extend beyond the top of Formation 2. The structural features are characteristic of three main areas, including the western part, the central part, and the eastern part (Appendix C-6). 1) The western part consists of northwest-southeast trending normal faults that are mostly east dipping toward the central part. 2) The central part is mainly controlled by the N-S trending normal faults that develop into a major graben structure, which is bounded on the western side by east-dipping normal faults and on the eastern side by a series of west-dipping normal faults. The topographic elevation of the graben structure is deeper than the western and eastern parts. 3) The western part is a structurally high area extending from the eastern side of the graben structure, which mostly contains a series of northwest-southeast trending, eastward dipping normal faults. An isopach map for the interval of units 2A-D illustrates the overall increase in thickness from the central graben toward the southern part of the study area (Appendix C-6).



The 1-D trend of the vertical proportional curve (VPC) generated by upscaling lithology logs represents the variability in the percentage of lithology stratigraphically (scale between 0 and 1) for sequence stratigraphy interpretation (Figure 12). The FS defined in well-correlation are related to the VPC that show the highest claystone content. Sequence boundaries (SB) are defined on the VPC, which has the highest sandstone content. The transgressive surface (TS) is formed as the first marine flooding surface that indicates the top of a lowstand system tract (LST) and the base of a transgressive system tract (TST). As the study area is located in the proximal continental shelf, the LST is expected to be thin and difficult to separate from the TST. Therefore, the LST and TST deposits are combined into a single package and separated from HST deposits by the MFS.

Formation 2 stratigraphic cycles are interpreted to be separated by the maximum flooding surfaces (MFS) according to the Genetic Stratigraphic Sequence approach (Galloway, 1989). As this study mainly works on the digital well-logs, the characteristic of MFS is well-recognized and it is applicable to correlate. Regarding this information, each stratigraphic cycle includes all three key system tracts (HST and LST & TST) and two main surfaces (SB and MFS).

The stratigraphic cycles of units 2A, 2B, and 2C exhibit a series of transgressive cycles, with back-stepping of facies pattern indicating shoreline movements in a landward direction. The maximum landward extension of the shoreline is likely near the top of unit 2C, based on the highest percentage of claystone as seen in the lithology logs

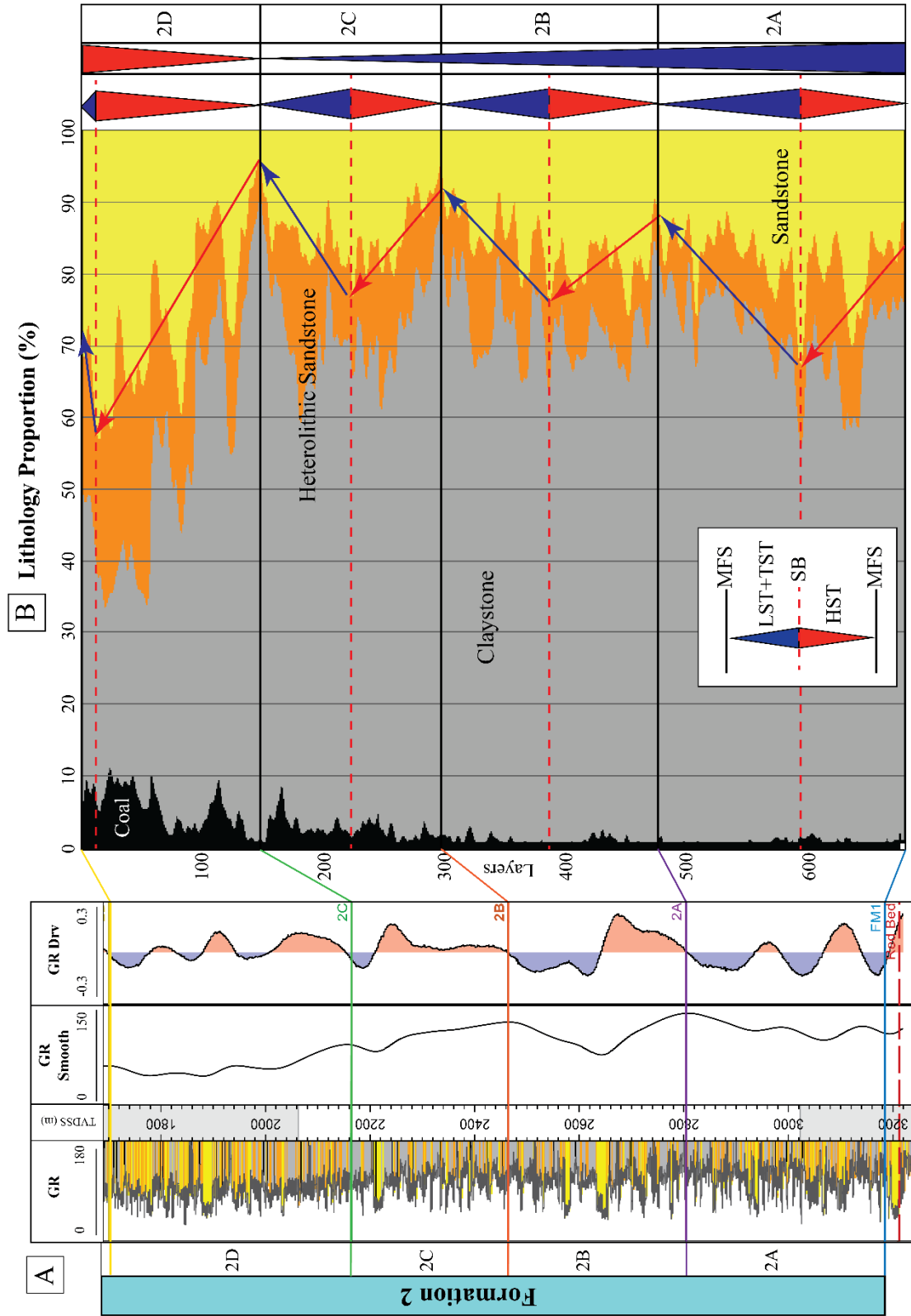


Figure 12. A) Type log for well-correlation shows the identified flooding surfaces. B) Lithology proportion curve shows the vertical proportion of four lithologies created from the upscaled lithology logs. System tracts are interpreted from the vertical proportion curve (VPC) and well-logs correlation. There are four zones, representing the third-order cycles, each of which consists of MFS: Maximum flooding surface; SB: Sequence boundary; LST: Lowstand system tract; TST: Transgressive system tract; HST: Highstand system tract (Catuneanu et al., 2010). The LST and the TST are combined into one package, as a thin LST and a difficulty to define the transgressive surface (TS) within the study area. The MFS is used to separate the LST and the TST deposits from HST deposits, which has the highest proportion of claystone content on VPC. SB is defined as the highest proportion of sandstone content and the transition from coarsening upward of HST to fining upward depositional trend of TST.

and VPC (Figure 12). Furthermore, unit 2C has the lowest sandstone content compared to the other stratigraphic units. On the other hand, unit 2D strongly depicts a regressive character with fore-stepping or down-stepping of a facies pattern that represents the shoreline moving in a seaward direction. The proportion of sandstone significantly increases, as compared to the other stratigraphic units.

Spatial Distribution of Lithology, Porosity, Permeability, and Pore Volume

Lithology Distribution

A 3-D lithology model (Figure 13) using the stratigraphic and structural framework interpretations described above is populated with results from electrofacies classification to reveal the spatial distribution of each lithology. This lithology model is constrained to stratigraphic frameworks, upscaling lithology logs, VPC of lithologies, input histogram of lithology percentages, and variograms. Based on the Formation 2 (units A-D) isopach map (Appendix C-6), the study area is separated into northwest and southeast regions. For these two regions, separate VPC curves are generated from the

upscaled lithology logs to compare how lithology varies between the regions (Figure 14).

Unit 2A consists of 1% coal, 72% claystone, 10% heterolithic sandstone, and 18% sandstone. The percentage of sandstone in the northwest region is ~18%, while the southeast region has 16% with greater claystone content.

Unit 2B contains 1% coal, 72% claystone, 11% heterolithic sandstone, and 16% sandstone. The overall percentage of each lithology in this unit is quite similar to the underlying unit 2A. The sandstone content in the northwest region is about 16%, whereas the southeast region is approximately 18%.

Unit 2C consists of 2% coal, 71% claystone, 13% heterolithic sandstone, and 14% sandstone. The overall percentages of sandstone in unit 2C indicate a significant decrease compared to the underlying units (Figure 13). In place of sandstone, unit 2C has a minimal increase in the quantity of coal and heterolithic sandstone. The northern region has 15% sandstone, while the southern region has only 11% sandstone. During this period, the major direction of sedimentary supply moved principally in a northwest to southeast direction.

Unit 2D is recognized by a dramatic increase in sandstone percent to almost 25%, and by an increase in heterolithic sandstone to ~19%. In addition, unit 2D has the highest quantity of coal, while claystone significantly decreases from the underlying units, to just ~50%. The northwestern region has 26% sandstone, while the southeastern region shows ~24%.

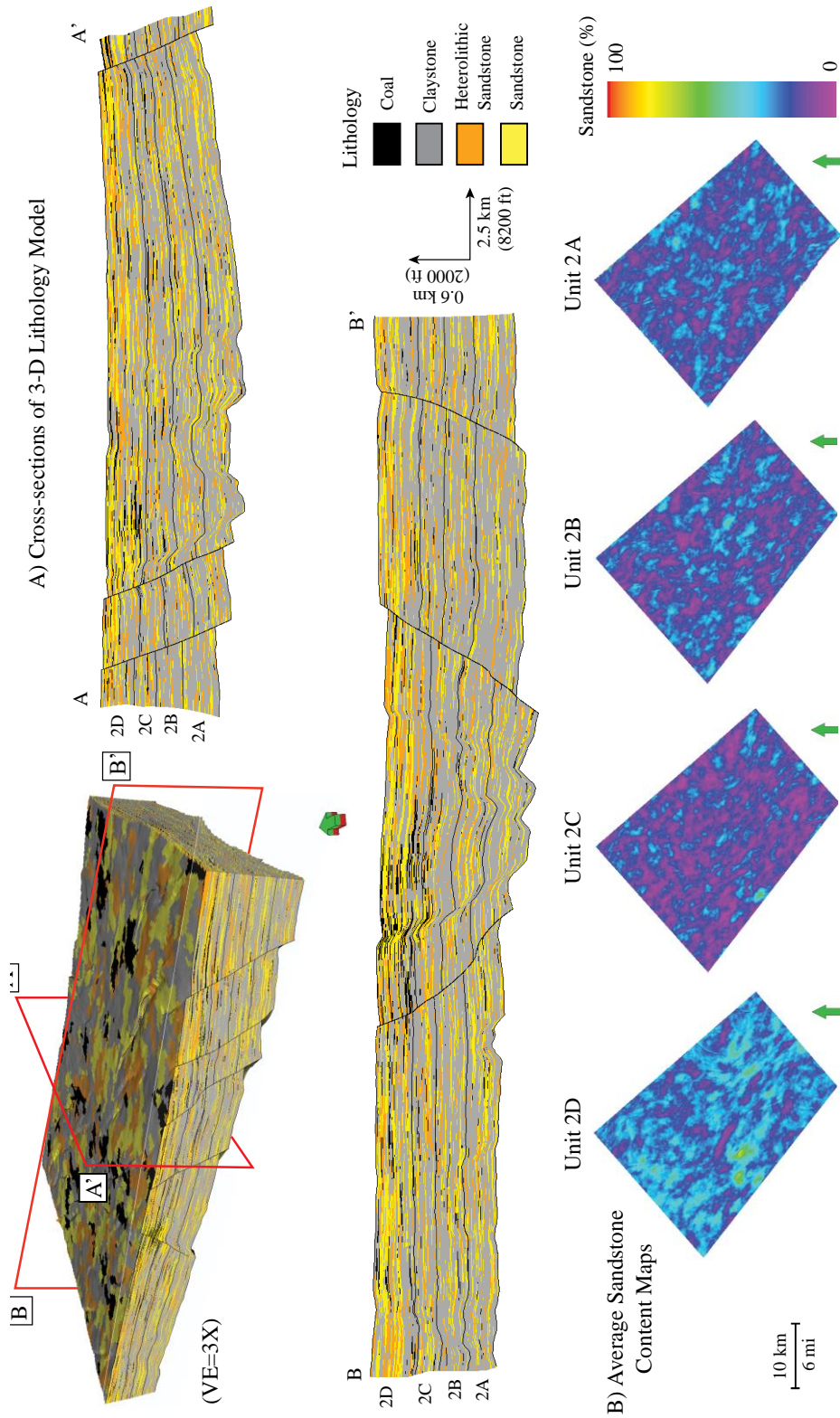


Figure 13. A) 3-D lithology model and its cross-sectional views. Note that sandstone content increase stratigraphically upward. The regressive cycle, occurring in unit 2D, has the highest sandstone content, while transgressive cycles, showing in units 2A-C, have a lower sandstone content. All figures are vertically exaggerated by three times (3X) their original size. B) The average sandstone content maps of units 2A-D.

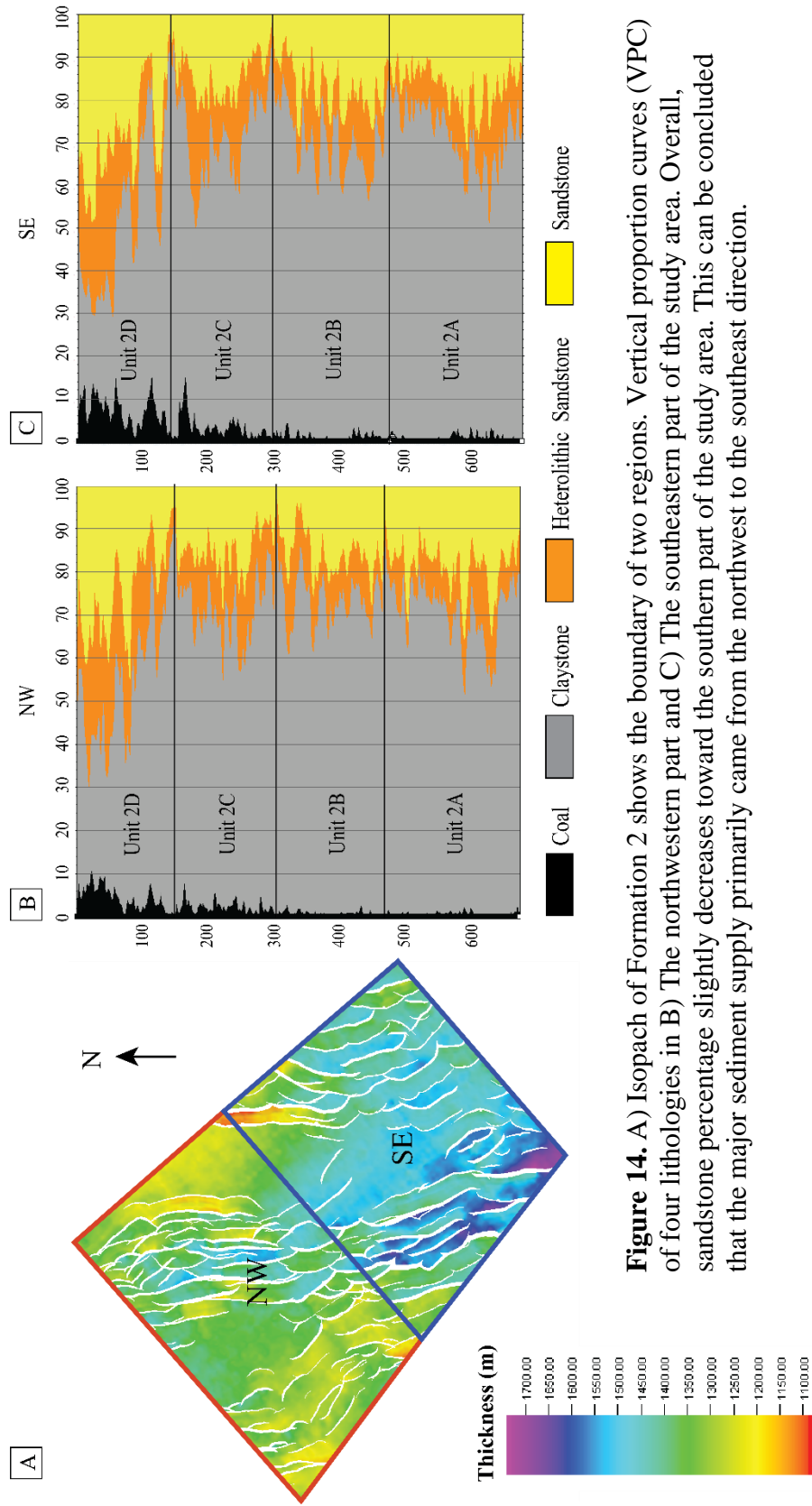


Figure 14. A) Isopach of Formation 2 shows the boundary of two regions. Vertical proportion curves (VPC) of four lithologies in B) The northwestern part and C) The southeastern part of the study area. Overall, sandstone percentage slightly decreases toward the southern part of the study area. This can be concluded that the major sediment supply primarily came from the northwest to the southeast direction.

Overall, the lithology distribution conforms significantly to the stratigraphic cycles as shown in Figure 12. The transgressive cycles, 2A, 2B, and 2C, have abundant claystone and less sandstone, whereas the regressive cycle, recorded in unit 2D, has a higher sandstone percent. In addition, unit 2D has the highest quantity of coal. The major direction of sediment supply is dominantly northwest to southeast, as observed from the changes in sandstone content between two regions in each unit (Figure 14).

Porosity, Permeability, and Pore Volume Distribution

Porosity and permeability models illustrate the spatial distributions that they are constrained by lithology model, upscaling petrophysical properties logs, input histogram of petrophysical properties, and variogram parameters.

Resulting from the effective porosity model (Figure 15), unit 2A has the lowest porosity range of 4-10% [mean = 13%], unit 2B has a slight increase in porosity range of 4-16% [mean = 14%], and unit 2C has the porosity range of 4-19% [mean = 16%]. In contrast to those three units, unit 2D has the highest porosity range of 8-23% [mean = 19%]. It can be observed that porosity increases stratigraphically upward, with an increasing amount of sandstone content especially in unit 2D (Appendix E-1).

Regarding the direction of sediment supply, the proximal area corresponding to the northwestern part of the study area is likely to have a better effective porosity than the distal area in the southeastern part of the study area.

The permeability model (Figure 16) was additionally constrained with the porosity model using a collected co-kriging algorithm and a correlation between porosity and permeability of core-plug analysis. Units 2A and 2B have the same

permeability range of ~2-84 mD [mean = 18%] while unit 2C has the lowest permeability range of ~0.04-9 mD [mean = 2%]. On the other hand, unit 2D has the greatest permeability range of ~5-177 mD [mean = 55%].

Based on a cross-plot between porosity and permeability (Figure 9) of core-plug data, sandstone lithofacies, including structureless sandstone, cross-bedded sandstone, parallel-laminated sandstone, and ripple cross-laminated sandstone, have higher permeability and porosity than heterolithic sandstone and claystone. From these observations, permeability distribution primarily increases corresponding to the amount of sandstone content. Therefore, it was not surprising that unit 2D with the greatest sandstone content has higher permeability and porosity distribution than units 2A-C.

As a result of changing the iteration numbers in lithology and porosity models (N=100), the pore volume distribution (Figure 17) was calculated in P10, P50, and P90 (P stands for Percentile) by Monte Carlo simulation. The unit of these percentiles is billion cubic meters (BCM). For pore volume distribution at P10-P50-P90, unit 2A has 11-12-13, unit 2B has 13-14-15, unit 2C has 16-17-18, and unit 2D has 19-20-21 BCM. The amount of pore volume increases primarily with the sandstone content and porosity distribution, in which unit 2D has the highest pore volumes, whereas units 2A-C exhibit a continuous decrease in pore volumes.

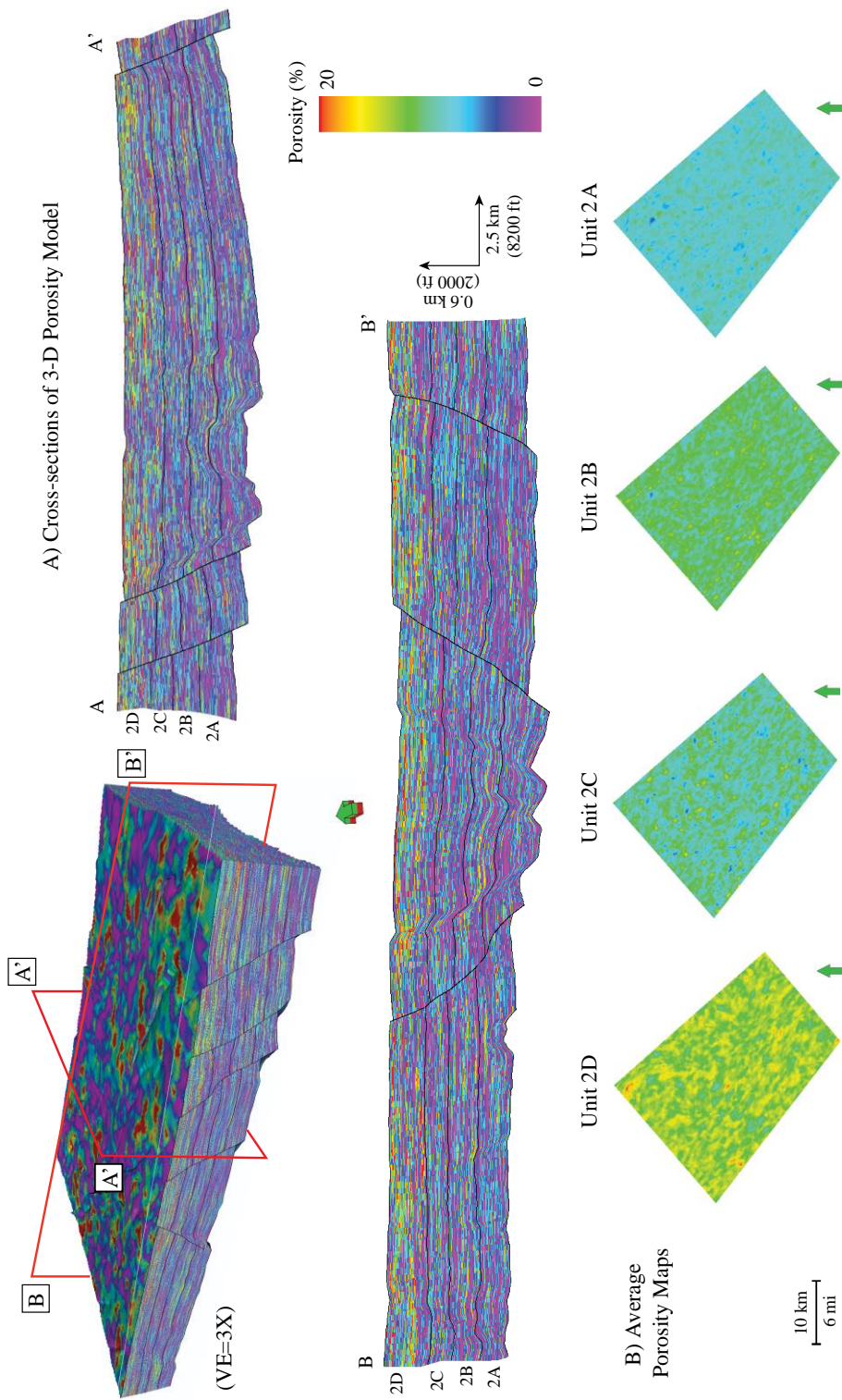


Figure 15. A) 3-D effective porosity model and its cross-sectional views. Note that porosity increases stratigraphically upward, which a regressive cycle of unit 2D has the highest effective porosity. All figures are vertically exaggerated by three times (3X) their original size. B) The average porosity maps of units 2A-D.

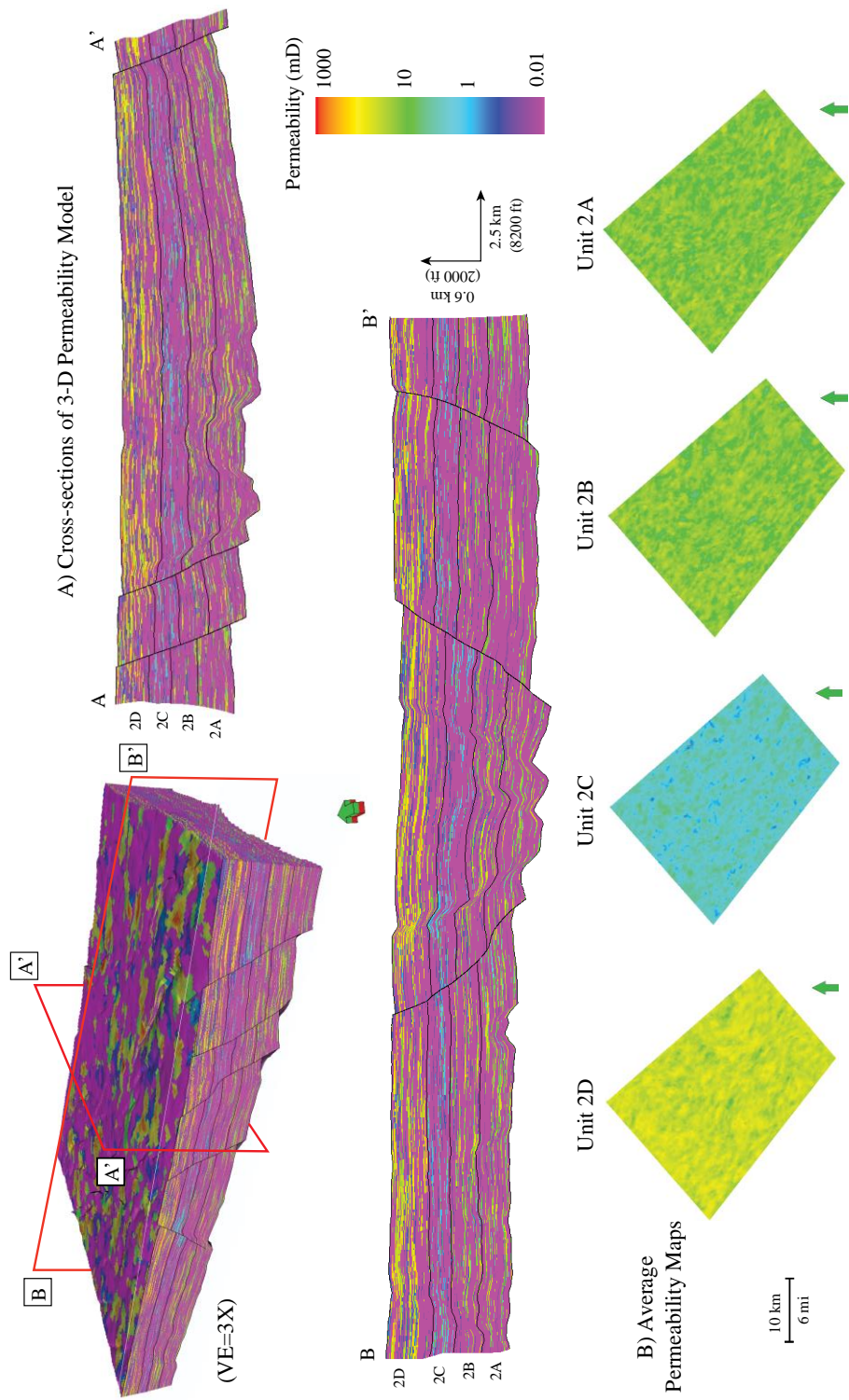


Figure 16. A) 3-D permeability model and its cross-sectional views. Note that permeability increases stratigraphically upward, which a regressive cycle of unit 2D has the highest permeability, while the transgressive cycles of units 2A-C have a low permeability especially unit 2C. All figures are vertically exaggerated by three times (3X) their original size. B) The average permeability maps of units 2A-D.

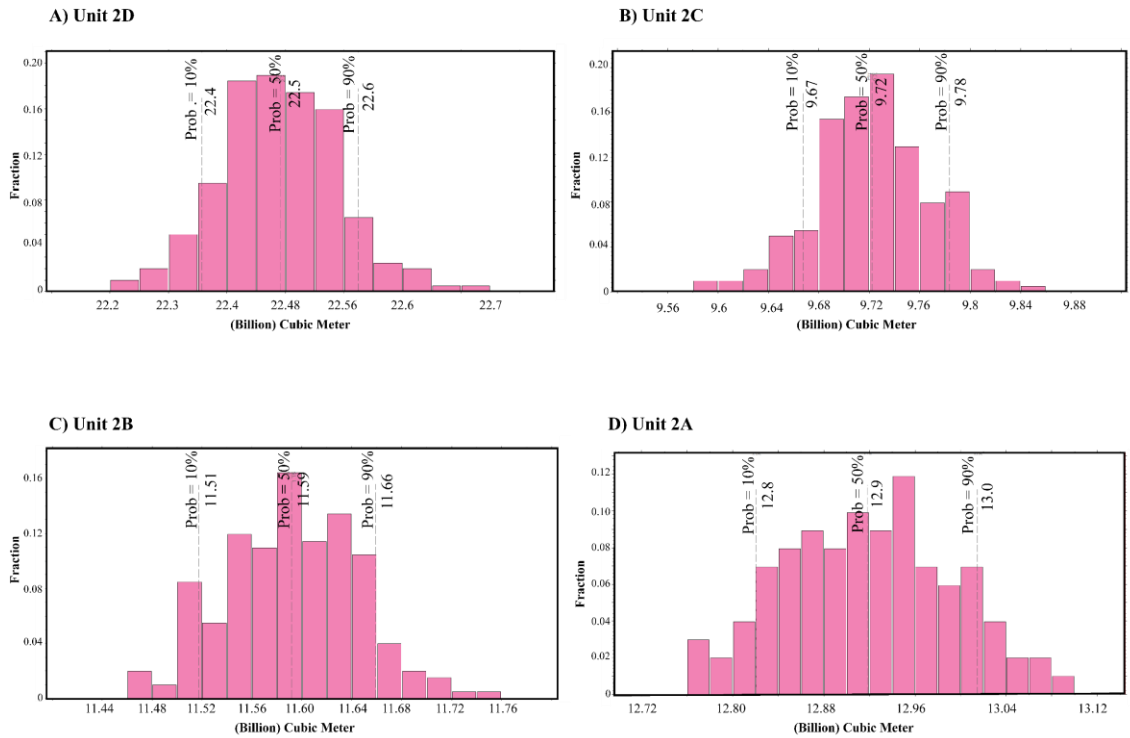


Figure 17. Pore volume distribution representing A) unit 2D, B) unit 2C, C) unit 2B, and D) unit 2A. The regressive cycle of unit 2D has the greatest amount of pore volumes, while the transgressive cycles, including units 2A-C, stratigraphically decrease upward in pore volumes, especially unit 2C.

Volumetric Estimations

The original gas-in-place (OGIP) was calculated in one of the future candidate platforms as prospective areas were provided by PTTEP (Appendix E-2). Using the input parameters (Table 4) and resulting from lithology and porosity models (N=100), the OGIP distribution was determined using the Monte Carlo simulation as shown in P10, P50, and P90 (P stands for percentile). The unit of these percentiles is billion standard cubic feet (Bscf). For the OGIP distribution at P10-P50-P90, unit 2A has 86-96-106, unit 2B has 117-130-142, unit 2C has 47-52-59, and unit 2D has 41-46-51 Bscf. It can be observed that units 2A and 2B are the major contributors to the OGIP resulting from the combination of stratigraphic and structural trap mechanisms. Despite unit 2D

having a high amount of sandstone and reservoir quality, it lacks a suitable structural trap mechanism as faults are dominantly losing slip near the top of unit 2D causing a low OGIP. Unit 2C with less sandstone content and low reservoir quality has the lowest OGIP. Overall, the OGIP number derived from the 3-D reservoir model is relatively consistent with the internal OGIP estimation made by PTTEP Company.

Discussion

Depositional Environment

Formation 2 contains nine key lithofacies that suggest fluvial and tidal depositional processes deposited in coastal-plain to marginal-marine environments. A tide-dominated delta is an analog depositional model for the study area, which illustrates a mix of fluvial and tidal processes (Figure 18). The deltaic environment contains three depositional regions, including the delta plain, the delta front, and the prodelta (Coleman and Prior, 1981). 1) The delta plain is a large subaerial region that consists of two sub-depositional environments including distributary channels and interdistributary areas. Tidal processes do not affect the upper delta plain, while fluvial processes and tidal processes also disturb the lower delta plain. 2) The delta front is an intertidal to a subtidal platform that fringes the delta plain and slopes gently seaward into the prodelta. Most of the sand transported through the distributary channels accumulate at the distributary mouth and forms distributary mouth bars. 3) The prodelta is the most distal part of the delta, where the suspended load (silt and clay) from the distributary channels is deposited.

Upward-fining successions consist of basal erosive lags through structureless sandstones, cross-bedded sandstones, and ripple cross-laminated sandstones with siltstone and claystone alterations (Figure 4). They are then covered by organic claystone with abundant root traces indicating the distributary channel deposits. These deposits are mainly located in the upper delta plain, where channel systems may have a high or low sinuosity depending on the slope gradient and grain size. Lithofacies successions suggest that sediment was transported by high-energy river currents. The

Depositional Environment

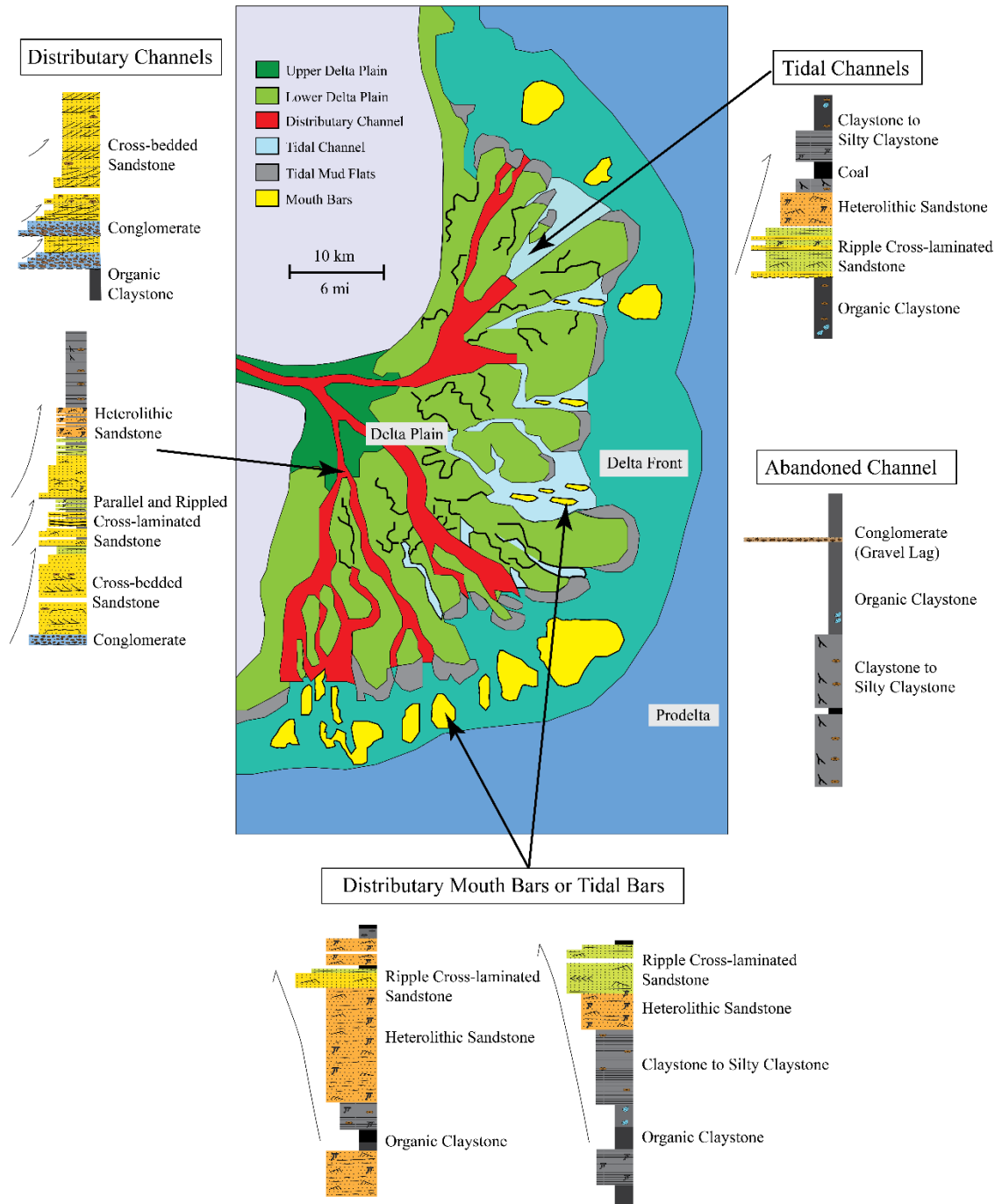


Figure 18. Analog model for depositional environments that shows the fluvial and tide-dominated deltaic deposits. These include the distributary channel, tidal channel, abandoned channel, distributary mouth bar, tidal bar, and tidal flat deposits ranging from delta plain and delta front (Modified from Allen and Chamber, 1998).

basal deposits contain abundant mudstone clasts that are floodplain deposits in origin and that were then eroded by distributary channels.

Thin gravel lags in organic claystones indicate abandoned-channel fill as a clay-plug (Figure 18). This could be an indication of delta-lobe switching caused by a decrease in current velocity, a high sedimentation rate, and a low-relief topography. In addition, the continuous rising of the sea level during the Early to Middle Miocene might have reduced slopes in distributary channels until they became inefficient. Consequently, the distributary channels migrated to the steeper slope area and formed new distributary channels (Olariu and Bhattacharya, 2006). This process is also known as the delta-lobe switching as is currently observed in the modern Mahakam Delta, Indonesia (Lambiase et al., 2016).

The upward-fining successions of muddy sandstone facies, including ripple cross-laminated sandstone and heterolithic sandstone grading into claystone and organic claystone, might represent tidal channels (Figure 18). In general, tidal channels occur in the lower delta plain, which shows a low relief topography and a tidal current that is strong enough to develop a tidal channel. Bi-directional cross-stratification in both fine-grained sandstones and heterolithic sandstones with abundant mudstone drapes also reveal a cyclic nature of tidal currents.

The upward-coarsening successions of heterolithic sandstone grading to ripple cross-laminated sandstone overlain on prodelta claystone could suggest distributary-mouth bars/tidal sand bars (Figure 18). The current velocity in the distributary channels diminishes when these channels enter the delta front. The bedload sands are transported through the distributary channel and form mouth bars at the channel end, whereas the

suspended clays bypass the distributary channels and are deposited in the prodelta. Sandstones generally consists of fine-grained sands with abundant small-scale current ripples showing the bi-directional cross-lamination. Moreover, there are numerous mudstone drapes in heterolithic sandstone, which create wavy and lenticular bedding suggesting tidal influence. Tidal currents possibly rework mouth bar sands during high tide and form tidal sand bars. There are abundant burrow traces, classified as a *Skolithos* ichnofacies, which significantly disrupt the original bedding of heterolithic sandstones.

The numerous coal beds formed in a swamp setting of the delta plain. Swamps generally support woody vegetation, while marsh supports non-woody plants, given the increasing salinity toward the shallow-marine habitat. Laminated and bioturbated claystones are the most abundant lithofacies observed in core samples, which contain significant root traces, burrows, and fossils. These observations might suggest marsh and tidal mudflat deposits.

Stratigraphic Framework

The stratigraphic framework of Formation 2 includes three regressive cycles of unit 2A-C and one regressive cycle of unit 2D, where the individual cycles are bounded by the MFS according to the Genetic Stratigraphic Sequence approach (Galloway, 1989). In terms of the global sea level cycles (Appendix A-2), the Early to Middle Miocene interval consists of five third-order sea-level cycles, when each cycle occurred approximately 1 to 3 million years. Vail et al. (1991) also described these third-order cycles as being largely controlled by glacio-eustasy.

Unit 2A is marked as a transition zone from the underlying fluvial-dominated Formation 1 that developed during the Last Glacial Maximum (LGM). During the Late Oligocene to Early Miocene, global sea level was approximately 123 m (404 ft) lower than the present-day sea level, which caused the continental shelf in Southeast Asia to be widely exposed and connected as a large landmass called Sundaland. The first rising of the eustatic sea level probably started around 19.6 Ma (Hanebuth et al., 2000) or during the Early Miocene. With a slow rising of eustatic sea level, the transgressive cycles of units 2A-C continuously developed by showing a back-stepping of facies pattern indicating landward movement of the shoreline (Figure 12). The maximum rising of eustatic sea level or the maximum landward extension of shoreline was possibly located near the top of unit 2C with the highest claystone content.

The regressive cycle of unit 2D was possibly caused by a combination of falling eustatic sea level and the local tectonic uplifting in the Malay Basin. Abreu and Anderson (1998) combined isotopic data from planktonic and benthic forams and indicated that the possible eustatic fall occurred between 12 and 14 Ma or during the Late Middle Miocene. Haq et al. (1987) also showed that the global sea level changed from a rising to a falling stage during the Late Middle Miocene (Appendix A-2). The eustatic sea level fall could have contributed to the strong regression and basinward shift of facies as recorded by unit 2D. Given the low-relief topography, small changes in sea level can produce a significant shift in shoreline position. In addition to the tectonic setting, the Malay Basin experienced compressional stress during the late middle Miocene or the deposition of unit 2D as recorded by the inversion structure (Appendix A-1). This tectonic setting might also have caused the regressive cycle of unit 2D. Until

a second pulse rising of the eustatic sea level occurred around 14.5 Mya or the late Middle Miocene, as described by Hanebuth et al. (2000), the Gulf of Thailand became a shallow-marine environment, as represented by Formation 3. The relationship between the stratigraphic cycles and the variations of depositional environments is difficult to determine based solely on well-log characteristics and the estimated lithology logs. In general, results from the stratigraphic analysis can be used to estimate the relative movement of shoreline position based on the stacking pattern of lithology.

Controls on Reservoir Quality and Productivity

The stratigraphic cycles, including the regression and the transgression, are primarily characterized on how the facies are distributed on VPC as shown in (Figure 12). A series of transgressive cycles occurring in units 2A-C exhibit an upward decrease of sandstone content toward the top of unit 2C, which possibly represents the maximum landward extent of the shoreline. On the other hand, the regressive cycle, unit 2D, has a progressive increase in sandstone content with a sudden decrease in claystone content. Regarding the sediment supply directions (Figure 14), the proximal area (the NW region) has greater sandstone content than the distal area (the SE region). Therefore, the variations of lithology distribution observed in Formation 2 result from a combination of stratigraphic framework and depositional setting.

Considering the spatial distributions of effective porosity, permeability, and pore volume, these reservoir qualities are principally controlled by stratigraphic cycles and facies distributions. In general, the effective porosity, permeability, and pore volume tends to increase with the amount of sandstone content. Unit 2D contains the highest

sandstone content and exhibits better reservoir quality than units 2A-C. However, the effective porosity tends to increase stratigraphically upward, whereas unit 2A, as it is located at the bottommost stratigraphic section, has the lowest porosity.

Referring to a cross-plot between porosity against permeability (Figure 9) of core-plug analysis, sandstone lithofacies, including structureless sandstone, cross-bedded sandstone, parallel-laminated sandstone, and ripple cross-laminated sandstone, show a wide range of porosities (6-23%) and permeabilities (0.05-800 mD). This could be explained by the internal heterogeneities in all lithofacies as observed in the core samples, which are varied in grain size, sorting, roundness, and sedimentary structure. In addition, heterolithic sandstone exhibit very low porosity (5-12%) and permeability (less than 0.1 mD), which can be related to the abundance of mud drapes and bioturbations as commonly seen in the core samples. Coal and claystone do not contain any significant reservoir quality.

The combination of stratigraphic and structural components are major mechanisms for hydrocarbon accumulation in this area. Even though unit 2D has the highest sandstone content and the best reservoir quality, it contains the lowest amount of OGIP given the lack of a structure component for trapping the hydrocarbon. Whereas, units 2A-B, having lower sandstone content and reservoir quality than unit 2D, are the main contribution to OGIP resulting from the larger fault displacement developing in this stratigraphic section. Unit 2C, including the lowest sandstone content and reservoir quality, also has the lowest volume of OGIP. According to all observations showing in this study, units 2A-B are considered to be the primary targets for the future development plan in this area.

Conclusions

The Early to Middle Miocene Formation 2 consists of nine dominant lithofacies that were deposited in fluvial and tide-dominated deltaic environments. The lithofacies include 1) coal, 2) organic claystone, 3) bioturbated and laminated claystone, 4) heterolithic sandstone, 5) parallel-laminated sandstone, 6) ripple cross-laminated sandstone 7) cross-bedded sandstone, 8) structureless sandstone, and 9) conglomerate. The sedimentary structures and facies successions observed in core samples indicate the deposition of the distributary channel, tidal channel, distributary mouth bar, tidal bar, swamp, and tidal flat settings.

To estimate rock types in non-cored wells, two methods of electrofacies classification are used, namely, Artificial-Neural Networks (ANNs) and K-means clustering analysis. The overall accuracy of lithofacies prediction obtained from both techniques is below 50%, and only laminated and bioturbated claystone has a user's accuracy of more than 80%. The confusion matrices reveal that coal, organic claystone, and heterolithic claystone are mostly predicted as laminated and bioturbated claystone, whereas parallel-laminated sandstone, structureless sandstone, and conglomerate are completely unclassified. This suggested that the vertical resolution of well logs is insufficient to fully capture the internal-variability of lithofacies as observed in core samples. Therefore, these nine lithofacies were combined into four lithologies: 1) coal, 2) claystone, 3) heterolithic sandstone, and 4) sandstone for mapping purposes. Using the same well-log inputs, the ANNs technique achieved the best overall accuracy, at 86%, while the K-means clustering method produced the highest overall accuracy of

only 69%. Regarding to these results, lithology logs were estimated using the ANNs for non-cored wells.

Using the derivative trend analysis (DTA) of GR logs is the most effective method to establish a sequence-stratigraphic framework. The Formation 2 forms a subset of a large first-order transgressive sequence that includes the underlying Formation 0, Formation 1, and the overlying Formation 3. The Formation 2 consists of five third-order stratigraphic cycles named, from deepest to shallowest, units 2A-E. The distinct and laterally extensive claystone representing the maximum flooding surfaces separate these units. This study focuses on four units, 2A-D, of which units 2A-C represent a continuous transgression and landward shift of facies. The top of unit 2C probably shows the maximum landward extent of the shoreline. Unit 2D indicates a major regression and basin-ward shift of facies resulting from the combination between the global sea level fall and the local tectonic uplifting in this region.

Constrained by core samples, lithology logs from 94 wells, and 3-D seismic data, 3-D reservoir models illustrated the spatial distribution of lithologies, major faults, porosities, and pore volumes of the fluvial and tide-dominated deltaic deposits. A lithology model, constructed by a sequential indicator simulation, illustrates the spatial distribution of lithologies and their relation to the stratigraphic framework. The increase of sandstone percent relates to the regressive cycle of unit 2D, while transgressive cycles of units 2A-C have a lower sandstone percentage. The regressive cycle of unit 2D has higher porosity and permeability than the transgressive cycles of unit 2A-C. The highest pore volume is in unit 2D, while unit 2C has the lowest pore volume. From these observations, it can be concluded that the sequence stratigraphy plays an

important role in the variation of lithology and reservoir quality distribution in Formation 2.

References

- Abdi, H., and L. Williams, 2010, Principal component analysis: Wiley Interdisciplinary Reviews Computational Statistics, v. 2, p. 433-459.
- Abreu, V. S., and J. B. Anderson, 1998, Glacial eustasy during the Cenozoic, Sequence stratigraphic implications: AAPG Bulletin, Vol. 82, No. 7 (July 1998), p. 1385-1400.
- Allen, G., and L. C. J. Chambers, 1998, Sedimentation in the modern and Miocene Mahakam delta, Jakarta, Indonesia: Indonesian Petroleum Association, 236 p.
- Allen, D. B., and M. J. Pranter, 2016, Geologically constrained electrofacies classification of fluvial deposits, An example from the Cretaceous Mesaverde group, Uinta and Piceance basins: AAPG Bulletin, v. 100, no. 12, p. 1775-1801.
- Antonenko, P., D. Toy, and S. Niederhauser, 2012, Using cluster analysis for data mining in educational technology research: Educational Technology Research and Development, v. 60, no. 3, p. 383-398.
- Ashena R., and G. Thonhauser, 2015, Application of Artificial Neural Networks in Geoscience and Petroleum Industry, In: C. Cranganu, H. Luchian, M. Breaban, (Eds.), Artificial Intelligent Approaches in Petroleum Geosciences: Springer, p. 127-166.
- Carney, S., D. C. Barr, S. N. Chai, L. A. Leal, and M. F. A. Bakar, 2008, Reservoir characterization of the Middle Miocene reservoirs of the North Malay Basin, Malaysia Thailand Joint Development Area (MTJDA): Society of Petroleum Engineers, doi:10.2118/116311-MS.
- Carney, S., I. A. Aziz, W. Martins, A. Low, and J. Kennedy, 2010, Reservoir characterization of the Mio-Pliocene reservoirs of block PM301 in the North Malay Basin: Society of Petroleum Engineers, doi:10.2118/131017-MS.
- Catuneanu, O., W. E. Galloway, C. G. S. T. C. Kendall, A. D. Miall, H. W. Posamentier, A. Strasser, and M. E. Tucker, 2011, Sequence Stratigraphy, Methodology and Nomenclature: Newsletters on Stratigraphy, v. 44, no. 3, p. 173-245.
- Chopra, S., and K. J. Marfurt, 2007, Seismic attributes for prospect identification and reservoir characterization: Society of Exploration Geophysicists (SEG), Tulsa, OK, v. 11, 464 p.
- Coleman, J. M., and D. B. Prior, 1981, Deltaic environments of deposition, In: Scholle, P. A., and D. Spearing (Eds.), Sandstone depositional environments: AAPG Memoir, v. 31, p. 139-178.

- Cornel, O., and J. P. Bhattacharya, 2006, Terminal distributary channels and delta front architecture of river-dominated delta systems: *Journal of Sedimentary Research*, v. 76, no. 2, p. 212-233.
- Deng, X., Q. Liu, Y. Deng, and S. Mahadevan, 2016, An improved method to construct basic probability assignment based on the confusion matrix for classification problem: *Information Sciences*, v. 340–341, p. 250-261.
- Deutsch, C. V., 2006, A sequential indicator simulation program for categorical variables with point and block data, *Block SIS: Computers and Geosciences*, v. 32, p. 1669–1681.
- Ding, C., and X. He, 2004, Principal component analysis and effective K-means clustering, *Society for Industrial and Applied Mathematics: 21st Proceedings of the SIAM International Conference on Data Mining, Banff, Canada*, p. 497-501.
- Dong, Y., J. Hou, Y. Liu, Y. Wang, J. Zhao, Y. Shi, and J. Zou, 2015, A back propagation artificial neural network application in lithofacies identification: *11th International Conference on Natural Computation (ICNC)*, p. 1028-1033.
- Galloway, W. E., 1989, Genetic stratigraphic sequences in basin analysis I, Architecture and genesis of flooding-surface bounded depositional units: *AAPG Bulletin*, v. 73, p. 125-142.
- Guo, H., 2011, A Simple algorithm for fitting a gaussian function (DSP Tips and Tricks): *Signal Processing Magazine, IEEE*, v. 28, no. 5, p. 134-137.
- Hanebuth, T. J. J., K. Stattegger, and P. M. Grootes, 2000, Rapid flooding of the Sunda shelf, A late-glacial sea level record: *Science*, v. 288, p. 1033–1035.
- Hanebuth, T. J. J., H. K. Voris, Y. Yokoyama, Y. Saito, Yoshiki, and J. Okuno, 2011, Formation and fate of sedimentary depocentres on Southeast Asia's Sunda Shelf over the past sea level cycle and biogeographic implications: *Earth Science Reviews*, v. 104, no. 1, p. 92-110.
- Haq, B. U., J. Hardenbol, and R. R. Vail, 1987, Chronology of fluctuating sea levels since the Triassic (250 million years ago to present): *Science*, v. 235, p. 1156-1167.
- Kanungo, T., D. Mount, N. Netanyahu, C. Piatko, R. Silverman, and A. Wu, 2002, An efficient K-means clustering algorithm, Analysis and implementation, *Pattern Analysis and Machine Intelligence: IEEE Transactions on Pattern Analysis and Machine Intelligence*, v. 24, no. 7, p. 881-892.

- Kumar, B., and M. Kishore, 2006, Electrofacies classification – a critical approach: 6th International conference and exposition on petroleum geophysics, Kolkata, India, p. 822-825.
- Kummerdsiri, K., B. Ainsworth, A. Mitchell, and G. Backy, 2013, Integrated stratigraphic and structural evolution of a fluvial-dominated, tide-influenced marginal marine system, the North Malay Basin, Gulf of Thailand (abs.): AAPG Annual Convention and Exhibition, Pittsburgh, Pennsylvania, May 19-22, 2013, <http://www.searchanddiscovery.com/abstracts/html/2013/90163ace/abstracts/kum.htm>, (accessed February 4, 2017)
- Lambiase, J., R. S. Riadi, N. Nirisal, and S. Husein, 2016, Transgressive successions of the Mahakam Delta Province, Indonesia: Geological Society, London, Special Publications, v. 444, no. 1, p. 335-348.
- Leo, C. T. A. M., 1997, Exploration in the Gulf of Thailand in deltaic reservoirs, Related to the Bongkot Field: Geological Society, London, Special Publications, v. 126, p. 77-87.
- Madon, M. B. H., 1995, Tectonic evolution of the Malay and Penyu Basins, Offshore Peninsular Malaysia: Ph.D's thesis, University of Oxford, 325 p.
- Madon, M. B. H., 1997, Analysis of tectonic subsidence and heat flow in Malay Basin, Offshore Peninsular Malaysia: Geological Society of Malaysia Bulletin, v. 41, p. 95-108.
- Madon, M. B., R. Bt. Abd. Karim, and R. W. H. Fatt, 1999a, Tertiary Stratigraphy and Correlation Schemes, Chapter 6: Petroleum Geology and Resources of Malaysia, p. 114-133.
- Madon, M. B. H., P. Abolins, M. J. B. Hoesni, and A. B. Ahmad, 1999b, Malay Basin, In: Selley R., and L. K. Meng, (Eds.): The Petroleum Geology and Resources of Malaysia, p. 173-217.
- Madon, M. B., J. S. Yang, P. Abolins, M. Y. Redzuan, and B. Z. Azmi, 2006, Petroleum system of the northern Malay Basin: Geological Society Malaysian Bulletin, v. 49, p. 125-134.
- Morley, C. K., 2001, Combined escape tectonics and subduction rollback back arc extension: A model for the Tertiary rift basins in Thailand, Malaysia, and Laos: Journal of the Geological Society, London, v. 158, p. 461-474.
- Morley, C. K., and R. Westaway, 2006, Subsidence in the super-deep Pattani and Malay Basins of Southeast Asia, A coupled model incorporating lower-crustal flow in response to post-rift sediment loading: Basin Research, v. 18, no. 1, p. 51-84.

- Petchdong, S., 2008, Controls on reservoir quality in a depositional framework of Formation 2, South Bongkot Area, North Malay Basin, Gulf of Thailand: *Bulletin of Earth Sciences of Thailand*, v. 3, p. 5-8.
- Polachan, S., 1986, Oil Potential in the Gulf of Thailand: Offshore Technology Conference, p. 255-259.
- Pubellier, M., and C.K. Morley, 2014, The basins of Sundaland (SE Asia), Evolution and boundary conditions: *Marine and Petroleum Geology*, v. 58, p. 555-578.
- Purnima, B., and A. Kumar, 2014, A clustering technique based on elbow method and K-means in WSN: *International Journal of Computer Applications (0975-8887)*, v. 105, no. 9 (November 2014), p. 17-24.
- Pyrzcz, M. J., and C. V. Deutsch, 2014, *Geostatistical Reservoir Modeling*, 2nd ed.: Oxford University Press, 433 p.
- Setiawan, A. S., M. H. Simatupang, A. Rachmadi, C. Jiraratchwaro, and M. F. M. Pushiri, 2016, Brown field optimization to maximize gas recovery in Muda Central Field of Joint Development Area, North Malay Basin: *International Petroleum Technology Conference*, doi:10.2523/IPTC-18700-MS.
- Shoup, R. C., R. J. Morley, T. Swiecicki, and C. Stuart, 2012, Tectono-stratigraphic framework and Tertiary paleogeography of Southeast Asia, Gulf of Thailand to South Vietnam Shelf: AAPG Search and Discovery Article #30246, http://www.searchanddiscovery.com/pdfz/documents/2012/30246shoup/ndx_shoup.pdf. html, (accessed January 30, 2018).
- Tapponnier, P., G. Peltzer, A.Y. L. Dain, R. Armijo, and P. Cobbold, 1982, Propagating extrusion tectonics in Asia, New insights from simple experiments with plasticine: *Geology*, v. 10, p. 611-616.
- Tavakkoli, M., R. Kharrat, and S. Inaloo, 2010, SGS versus Collocated Cokriging Petrophysical Modeling, A Comparative Study in a Heterogeneous Gas Condensate Carbonate Reservoir: *Society of Petroleum Engineers*, doi:10.2118/127381-MS.
- Ting, K. M., 2011, Confusion matrix, In: Sammut, C., and G. I. Webb (Eds.), *Encyclopedia of machine learning*, 1st ed.: New York, Springer, 209 p.
- Vail, P. R., F. Audemard, S. A. Bowman, P. N. Eisner, and C. Perez-Cruz, 1991, The stratigraphic signatures of tectonics, eustasy, and sedimentology, An overview, In: Einsele G., W. Ricken, A. Seilacher (Eds.), *Cycles and events in stratigraphy*: Springer-Verlag, Berlin, p. 617-659.

Watcharanantakul, R., and C.K. Morley, 2000, Syn-rift and post-rift modeling of the Pattani Basin, Thailand, Evidence for a ramp-flat detachment: *Marine and Petroleum Geology*, v. 17, no. 8, p. 937-958.

Wethington, N., 2017, Stratigraphic Architecture of the Mississippian Limestone through integrated electrofacies classification, Hardtner Field area, Kansas and Oklahoma, Master's thesis, University of Oklahoma, Norman, Oklahoma, 103 p.

Table 1. Horizontal and vertical variogram range by zone for lithology model

Unit/Zone	Lithology	Azimuth	Major Horizontal Range (m)	Minor Horizontal Range (m)	Vertical Range (m)	Lithology (%)
2D	Coal	310	2000	2000	12	6
	Claystone	310	2000	2000	15	50
	Heterolithic Sandstone	310	1700	800	13	19
	Sandstone	310	2200	1000	15	25
2C	Coal	310	1500	1500	10	2
	Claystone	310	2000	2000	20	71
	Heterolithic Sandstone	310	1300	700	8	13
	Sandstone	310	1600	800	10	14
2B	Coal	310	1500	1500	8	1
	Claystone	310	2000	2000	18	72
	Heterolithic Sandstone	310	1500	700	9	11
	Sandstone	310	1700	800	12	16
2A	Coal	310	1500	1500	8	1
	Claystone	310	2000	2000	18	72
	Heterolithic Sandstone	310	1500	700	9	10
	Sandstone	310	1700	800	11	18

Table 2. Horizontal and vertical variogram range by zone for effective porosity and permeability models. These ranges are decreased from lithology modeling to account for internal variability within lithologies.

Unit/Zone	Lithology	Azimuth	Major Horizontal Range (m)	Minor Horizontal Range (m)	Vertical Range (m)	Permeability Range Min-Max (mD)
2D	Coal	310	1000	1000	8	0
	Claystone	310	1500	1500	7	0
	Heterolithic Sandstone	310	1300	600	7	0-0.0.5
	Sandstone	310	1600	800	8	10-1000
2C	Coal	310	900	900	7	0
	Claystone	310	1500	1500	10	0
	Heterolithic Sandstone	310	1000	500	5	0-0.2
	Sandstone	310	1200	500	5	0.2-40
2B	Coal	310	900	900	5	0
	Claystone	310	1500	1500	8	0
	Heterolithic Sandstone	310	1000	500	6	0.01-0.3
	Sandstone	310	1300	500	6	0.17-250
2A	Coal	310	900	900	5	0
	Claystone	310	1500	1500	8	0
	Heterolithic Sandstone	310	1000	500	7	0.02-0.0.5
	Sandstone	310	1200	500	6	0.52-400

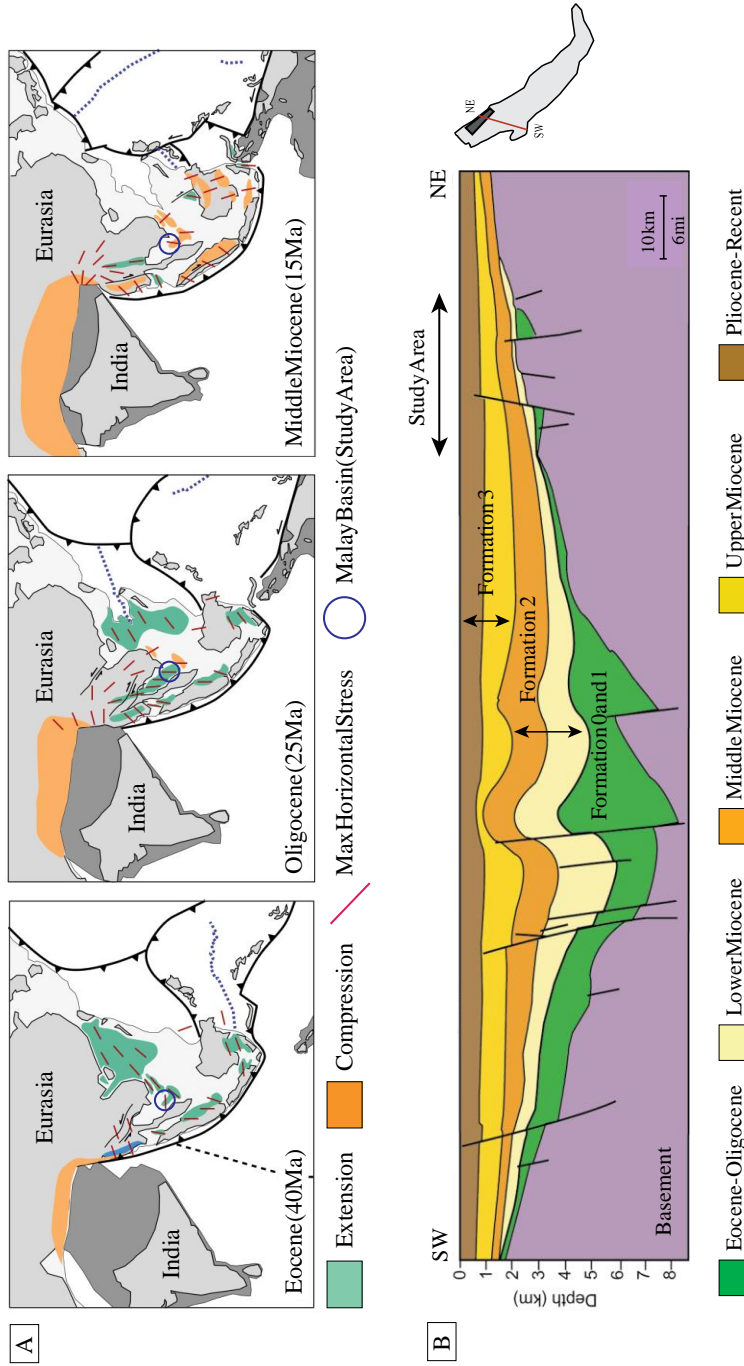
Table 3. Summary of the dominant lithofacies present in the early to middle Miocene Formation 2 from four cored wells in the study area (Figure 3). There are nine lithofacies, which are grouped into 4 main lithologies. This grouping is based on common log character responses in order to differentiate classes for electrofacies classification.

Lithology	Lithofacies	Description	Relative log responses	Depositional Process
Coal	Coal	Black to very dark gray, commonly broken and covered by sulfur on the surface, no sedimentary structure or bioturbation	Moderate radioactivity (GR 80-130 API), very low bulk density, very high neutron porosity, very slow sonic	Peat accumulation and coalification
	Organic Claystone	Dark gray to black claystone, abundant parallel carbonaceous laminations, locally fossiliferous, and generally denser than coal	High radioactivity (GR > 130 API), high bulk density, high neutron porosity, and moderate sonic	Low energy setting, suspension of fine-grained sediments
Claystone	Laminated and Bioturbated Claystone	Medium to dark gray claystone grading into silty claystone, parallel-carbonaceous laminations, and slightly lenticular siltstone, locally fossiliferous and root traces	High radioactivity (GR > 130 API), high bulk density, moderate neutron porosity, and moderate sonic	Low energy setting, suspension of fine-grained sediments
	Poorly-bedded and Bioturbated Heterolithic Sandstone	Brownish-gray to medium gray heterolithic sandstone, fine-to fine-grained sand, moderate to well sorted, sub-rounded to rounded. Wavy to flaser beddings interbedded with abundant mud lamination and mud drapes, possible Skolithos burrowing, and local fossiliferous	Moderate radioactivity (GR 100-140 API), high bulk density, moderate neutron porosity, and moderate sonic	Low energy setting, flood-ebb tidal currents with intervening slackwater suspensions causing a bundle sequence pattern
Sandstone	Parallel-laminated Sandstone	Light to medium gray sandstone, very fine-to medium-grained sand, moderate to well sorted, sub-rounded to sub-angular, and generally parallel laminations, and mud drapes	Moderate radioactivity (GR 100-130 API), moderate bulk density, moderate neutron porosity, and moderate sonic	Low energy setting with tide-influenced deposition, mud laminations falling out from suspension during a slack tide
	Ripple Cross-laminated Sandstone	Light to medium gray sandstone, very fine-to fine-grained sand, low to moderate sorting, and sub-rounded to sub-angular. Ripple cross-lamination generally dipping in opposite directions. Locally herringbone cross-stratification. Commonly vertical-shaped burrowing.	Moderate radioactivity (GR 100-130 API), moderate bulk density, moderate neutron porosity, and moderate sonic	Low energy setting with different current directions, possibly indicates the tidal currents (flood-ebb tides)
	Cross-bedded Sandstone	Light to medium gray sandstone, medium-to coarse-grained sand, moderate to well sorted, and subrounded to subangular. Generally, include a trough cross-bedding. No bioturbation.	Low radioactivity (GR 50-90 API), low bulk density, moderate neutron porosity, and slow sonic	High-energy, bedload transported by unidirectional fluvial current
	Structureless Sandstone	Light to medium gray sandstone, medium-to coarse-grained sands, moderate to well sorted, sub-rounded to rounded. No obvious sedimentary structure and bioturbation.	Low radioactivity (GR 50-90 API), low bulk density, moderate neutron porosity, and slow sonic	High-energy, bedload transported by unidirectional fluvial current
Conglomerate	Clast-supported conglomerate (orthoconglomerate) containing granule-to pebble-grained of mudstone rip-up clasts, angular to rounded, and poor to moderate sorting, strongly react to hydrochloric (HCL) acid		Low radioactivity (GR 50-90 API), high bulk density, moderate neutron porosity, and moderate sonic	High-energy, bedload transported by unidirectional fluvial current

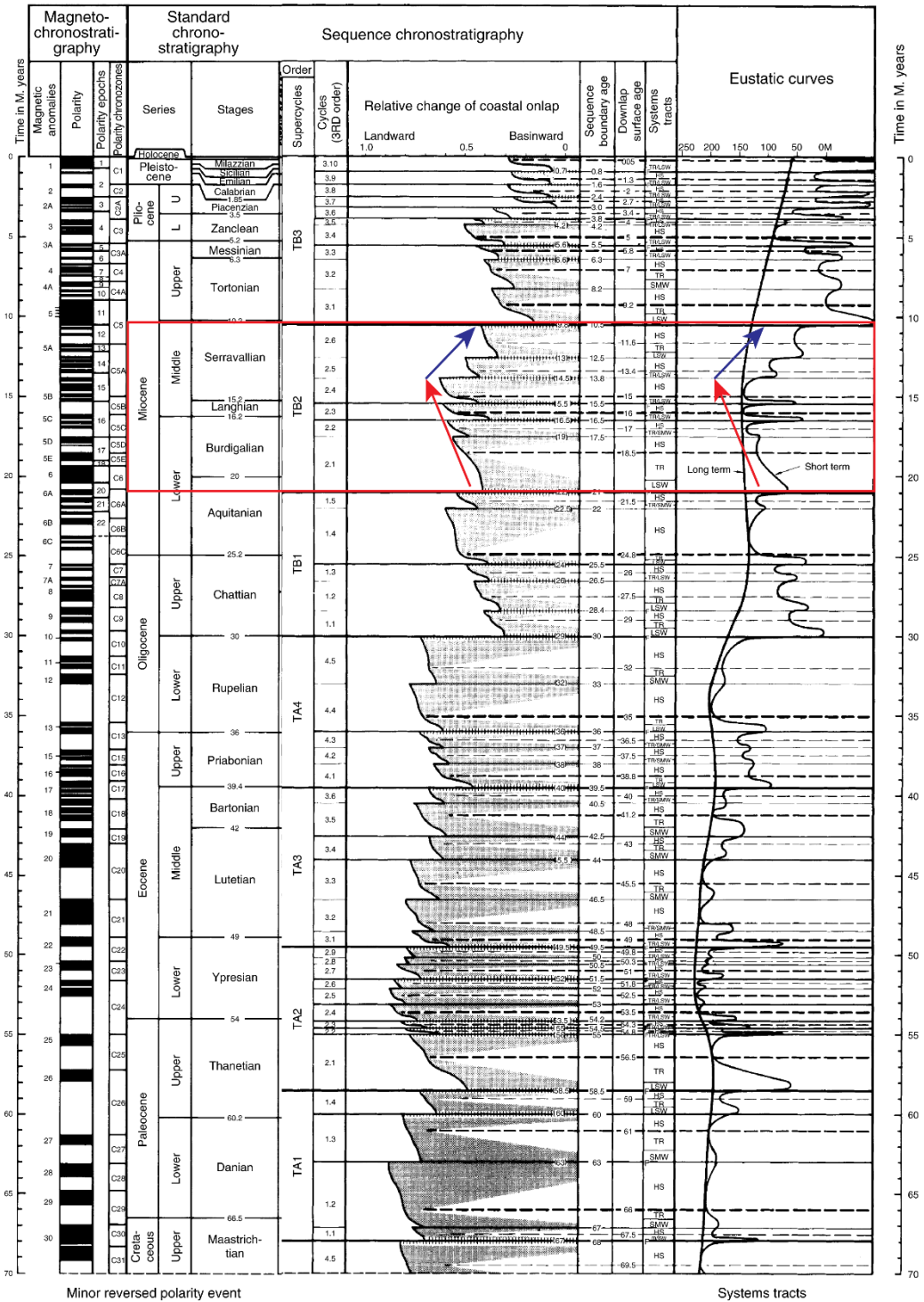
Table 4. Summary of parameters used for OGIP estimation. The prospective areas are defined in P10 and P90 cases as presented in Appendix E-2. Filling ratio means the total number of net pays divided by the total number of net sands in each stratigraphic unit estimating from well results. Bg is a function of temperature and pressure resulting from PVT database. P50 OGIP is 324 bscf, which units 2A and 2B are the major contributors resulting from the combination of stratigraphic and structural trap.

Unit/Zone	Parameter	Low	Mid	High
2D	Area (km ³)	7.5	-	14.3
	Filling Ratio (%)	0.05	0.15	0.30
	Bg	0.006	0.0065	0.007
	OGIP (Bscf)	41	46	51
2C	Area (km ³)	12.8	-	19.1
	Filling Ratio (%)	0.10	0.35	0.65
	Bg	0.004	0.0045	0.005
	OGIP (Bscf)	47	52	59
2B	Area (km ³)	9.5	-	18.2
	Filling Ratio (%)	0.10	0.35	0.65
	Bg	0.003	0.0035	0.004
	OGIP (Bscf)	117	130	142
2A	Area (km ³)	6.8	-	13.3
	Filling Ratio (%)	0.10	0.35	0.65
	Bg	0.002	0.0025	0.003
	OGIP (Bscf)	86	96	106
Total OGIP (Bscf)		291	324	358

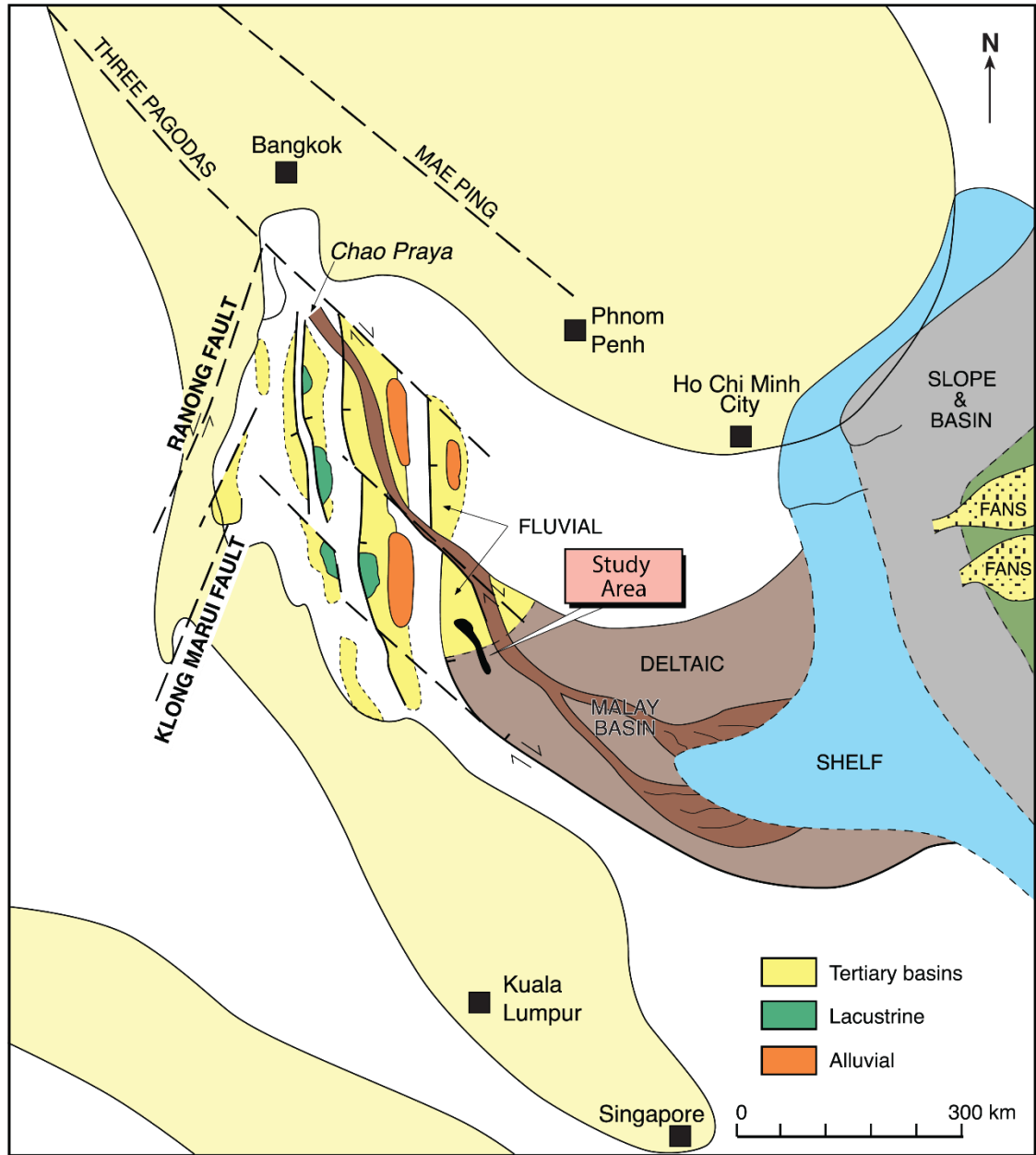
Appendix A: Geological Setting



Appendix A-1. (A) Tectonic restorations of Southeast Asia during 50-5 Ma to illustrate the basin evolution and relationship with tectonic events of the region (modified after Hall, 2012 and Pubellier and Morley, 2014). The Malay Basin was developed during 40 Ma (Middle Eocene) after a collision between India and Eurasia continental plates. The basin experienced a change of extensional stress direction, superimposing N-S trending Oligocene faults on the older E-W trend faults in the Eocene syn-rift sequence. A significant change in stress regime from extension to compression mainly occurred around 15 Ma (Middle Miocene), when inversion took place over a broad area of the Malay Basin. (B) A cross-section through the northern part of Malay Basin show a well-developed inversion structure in basin center, while the study area is dominantly controlled by normal faults.



Appendix A-2. Sea level curve for Early to Middle Miocene epoch is outlined in red (Modified from Haq et al., 1987). It shows that the global sea level during this time was changed from a rising (blue arrow) stage to a falling (red arrow) stage.







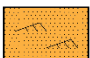

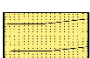

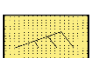










Appendix A-3. Paleogeography of the Gulf of Thailand during the Miocene, showing a deltaic system fed by the Chao Praya river in the north, and prograding towards the southeast and east (Leo, 1997).

Appendix B: Core Descriptions

Appendix B-1. Core Descriptions

The major lithofacies exhibited by the Early to Middle Miocene Formation 2 are identified through detailed core description of six core intervals covering 182.5 m (598.8 ft) from 4 cored wells (Figure 3). The legend of the core description is presented in the following.

Lithofacies	
 Coal	 Burrows
 Organic Claystone	 Root traces
 Claystone to Silty Claystone	 Gastropods and Pelecypods
 Heterolithic Sandstone	 Sideriet nodules
 Parallel-laminated sandstone	 Stylolites
 Ripple cross-laminated Sandstone	 Parallel-laminations
 Cross-bedded Sandstone	 Ripple Cross-laminations
 Structureless Sandstone	 Trough Cross-beddings
 Conglomerate	 Fining-upward Succession
	 Coarsening-upward Succession

Cored Well : A
Core Depth : 2452.0-2479.62 m
Core Length : 27.0 m
Unit : 2A

Depth m	Pebble	Granule	Sand					Silt	Clay	Sorting			Bioturbation			Lithology	Description	Structures
			VC	C	M	F	Vf			P	M	W	L	M	H			
2452																	Trough cross-bedding	
2453																	Trough cross-bedding	
2454																	Amalgamation surface at 2451.1 m	
2455														Preservation				
2456																	Trough cross-bedding	
2457																		
2458																	Amalgamation surface at 2458.4 m	
2459																		
2460																		
2461																		
2462																		
2463																		
2464																	Trough cross-bedding	

2452.0-2468.8 m: Sandstone, light to medium gray, fine to coarse grained sand, moderately to well sorted, mostly trough cross-bedding, generally found carbonaceous material lamination, more siderite nodules especially near the base of the interval

Depth m	Pebble	Granule	Sand					Silt	Clay	Sorting			Bioturbation			Lithology	Description	Structures
			VC	C	M	F	Vf			P	M	W	L	M	H			
2465																		
2466																		
2467																	Trough cross-bedding	
2468																		
														Preservation Sandstone			Erosional surface	
2469														Sandstone	2468.8-2471.1 m: Stacking multiple distributary channel, mudstone pebble conglomerate grading to sandstone, light to medium gray, mudstone clasts are generally pebble size, brown to yellowish orange and gray, some covered by sulphur, angular to rounded, reaction with HCL, sandstone is light to medium gray, medium to very coarse grained sand, moderately well sorted, trough cross-bedding, erosional surface at base		Trough cross-bedding	
2470														Conglomerate			Rip-up clasts Erosional surface	
2471														Sandstone			Trough cross-bedding	
														Conglomerate			Rip-up clasts Erosional surface	
2472														Organic Claystone	2471.1-2472.5 m: Coaly mudstone, dark to very dark gray, locally found pyrite nodules at 2472.43 m			
2473														Heterolithic sandstone				
2474														Silty claystone	2472.5-2474.5 m: Silty claystone grading to heterolithic sandstone toward the top, light to medium gray, heterolithic sandstone is v.fine grained sand, poorly to moderately sorted, subrounded, abundance siderite nodules, silty claystone is light to medium gray, more root traces/bioturbation in silty claystone, strong reaction with HCL (possible bioclast fragments)			
2475														Silty claystone				
2476														Organic Claystone	2475.4-2477.5 m: Organic claystone, medium to very dark gray, abundance coaly root traces			
2477																		
2478														Silty Claystone				
2479														Heterolithic sandstone	2477.5-2479.62 m: Fining upward, grading from heterolithic sandstone to silty claystone, heterolithic sandstone is medium gray, generally found root traces, abundance siderite nodules, burrowed, locally parallel lamination near the base		Ripple Cross-lamination	
2480																		

Cored Well : B
Core Depth : 2466.5-2497.5 m
Core Length : 28.7 m
Unit : 2B

Depth m	Pebble Granule	Sand					Silt Clay	Sorting			Bioturbation			Lithology	Description	Structures
		VC	C	M	F	Vf		P	M	W	L	M	H			
2466																
2467							λ?							Silty Claystone	2466.5-2471.5 m: silty claystone, medium to dark gray, stratification are disrupted by root traces, generally found siderite nodules	
2468						λ?										
2469						λ										
2470						λ										
2471																
2472														Heterolithic sandstone interbedded with silty claystone	2471.5-2473.6 m: heterolithic sandstone interbedded with claystone, vf grained sand, sandstone is medium gray and claystone is dark gray, vf grained sand, poorly laminated sandstone is generally disrupted by burrowing	Way Bedding Bioturbation
2473														Sandstone interbedded with silty claystone	2472.4-2475.2 m: fining upward, sandstone grading to sandstone interbedded with silty claystone in the top, v.fine-med grained sand, sandstone is light gray and claystone is very dark gray, parallel lamination, ripple cross-lamination in sandstone, possible soft-sediment deformation near the contact between sandstone interbedded with claystone, locally bioturbation, thick mud drape near the base	Ripple cross-lamination Soft-sediment deformation
2474														Sandstone	Poorly bedded mud drape Poorly bedded mud drape	
2475																
2476														Sandstone interbedded with silty claystone	2475.2-2477.2 m: fining upward, sandstone grading to sandstone interbedded with silty claystone in the top, fine-med grained sand, sandstone is light gray and silty claystone is very dark gray, generally found mud lamination, ripple cross-lamination in sandstone, local bioturbation, thick mud drape near the base	Ripple cross-lamination
2477														Sandstone		

Depth m	Pebble Granule	Sand					Silt Clay	Sorting			Bioturbation	Lithology	Description	Structures
		V	C	M	F	Vf		P	M	W				
2478												Sandstone		Trough cross-bedding
2479												Preservation	2477.2-2482.93 m: conglomerate grading to sandstone in the upper part, fining upward, sandstone is light gray to medium gray while conglomerate sandstone is medium gray, sandstone is very fine to coarse grained, trough and planar cross-bedding, locally found stylolites	Trough cross-bedding
2480														Trough cross-bedding
2481												Conglomerate	conglomerate containing rounded to angular rip-up mud pebbles with erosional contact at base	Erosional Contact
2482														Trough cross-bedding
2483												Conglomerate		Erosional surface
2484												Sandstone	2482.93-2485.35 m: sandstone, light-medium gray, medium to coarse grained, well to moderately sorted, subrounded to subangular, trough cross-bedding, locally contain big claystone clast, pebble size, amalgamation surface at base	Trough cross-bedding
2485														Amalgamation surface
2486												Preservation 2485.83-2486.0 m	2485.35-2487.9 m: sandstone, light-medium gray, fine-medium grained, moderately well sorted, subrounded, small to moderate scale planar cross-bedding, locally found stylolite layers causing by pressure solution, sharp contact at base	Trough cross-bedding
2487												Preservation 2487.18-2487.32 m		Trough cross-bedding
2488												Organic claystone	2487.9-2489.39 m: coaly claystone, dark to very dark, generally found parallel lamination of carbonaceous material	Sharp contact Parallel lamination
2489														
2490												Conglomerate	2489.35-2489.42 m: conglomerate, medium to dark gray, contain claystone pebbles (avg size: 4 mm, rounded to subangular) in silty to sandy matrix	-

Depth m	Pebble Granule	Sand					Silt Clay	Sorting			Bioturbation	Lithology	Description	Structures
		V	C	M	F	Vf		P	M	W				
2491												Organic claystone claystone	2487.9-2489.39 m: coaly claystone to claystone, dark to very dark, generally found parallel lamination of carbonaceous material, pelecypod molds at 2492.15 m	Parallel lamination
2492														
2493							λ					Silty Claystone		
2494							λ [?]							
2495							λ					Coaly claystone, Coal	2492.63-2497.50 m: silty claystone to clayey siltstone, medium gray to dark gray, generally found root traces and siderite nodules, coal layer at 2495.17-2495.20 m.	Bioturbation
2496							λ					Silty Claystone		
2497							λ [?]							
2498							λ [?]							

Well : B
 Core Depth : 2239.5 - 2293.0 m
 Core Length : 53.5 m
 Unit : 2C

Depth m	Sand					Silt Clay	Sorting			Bioturbation	Lithology	Description	Structures
	VC	C	M	F	Vf		P	M	W				
2239													
2240													
2241													
2242													
2243													
2244													
2245													
2246													
2247													
2248													
2249													
2250													
2251													

Depth m	Sand					Silt Clay	Sorting			Bioturbation	Lithology	Description	Structures	
	V	C	M	F	Vf		P	M	W					L
2252												Silty claystone		
2253												Claystone		
2254												Silty claystone		
2255												Silty claystone		
2256												Coal	2256.0 - 2256.8 m. dark gray to black, coal and coaly claystone, generally broken coal	-
2257												Silty claystone	2256.8-2257.4 m. medium to dark gray, increase sand content toward to the base, local coaly root traces, poorly laminated by borrowing or rooting	-
2258												Heterolithic sandstone	2257.4-2261.07 m. light to medium gray, vf-fine grained sand, heterolithic sandstone, abundant mud drape, bi-directional ripple cross-lamination, flaser to wavy bedding, generally bioturbated, gradational contact at base	Flaser to wavy Bedding Bi-directional cross-lamination
2259												Sandstone	2257.4-2261.07 m. light to medium gray, fine-med grained sand, sandstone, generally found mud lamination, local rip-up clast claystone, ripple cross-lamination, some poor lamination disrupted by burrowing, erosional surface at base	Parallel lamination Ripple cross-lamination
2260												Sandstone	2257.4-2261.07 m. light to medium gray, fine-med grained sand, sandstone, generally found mud lamination, local rip-up clast claystone, ripple cross-lamination, some poor lamination disrupted by burrowing, erosional surface at base	Erosional surface
2261												Sandstone	2257.4-2261.07 m. light to medium gray, fine-med grained sand, sandstone, generally found mud lamination, local rip-up clast claystone, ripple cross-lamination, some poor lamination disrupted by burrowing, erosional surface at base	Erosional surface
2262												Claystone	2261.07-2262.4 m. medium to dark gray, claystone, predominantly massive bedded, generally found siderite nodules, abundance shell fossils between 2263.3-2263.5 m with 5 mm-2 cm diameter size of gastropod/pelecypod fossils	
2263												Claystone	2261.07-2262.4 m. medium to dark gray, claystone, predominantly massive bedded, generally found siderite nodules, abundance shell fossils between 2263.3-2263.5 m with 5 mm-2 cm diameter size of gastropod/pelecypod fossils	
2264												Organic claystone	2263.9-2264.15 m. dark to very dark gray	
2265												Sandstone	2264.15-2265.8 m. light gray, coarsening upward sandstone, fine-med grained sand, abundance mud drape, parallel laminations, ripple cross-lamination, herring bone cross-bedding, tabular cross-bedding, mostly bioturbated	Parallel lamination

Depth m	Sand					Silt Clay	Sorting			Bioturbation	Lithology	Description	Structures	
	VC	C	M	F	Vf		P	M	W					L
2266													Herringbone cross-bedding Tabular cross-bedding	
2267												Heterolithic sandstone interbedded with claystone	2265.8-2267.8 m. light yellowish gray, vf grained sand, abundance mud drape, parallel lamination, ripple cross-lamination, moderately-heavily bioturbated toward to the base	Ripple cross-lamination Parallel lamination
2268												Silty claystone		Parallel lamination
2269												Silty claystone		
2270												Silty claystone		
2271													2268-2275 m., medium-dark gray, silty claystone to claystone, parallel lamination, generally found siderite nodules, locally observed pelecypod fossils between 2271.8-2272.1 m	
2272												Organic claystone		
2273														
2274												Clayey siltstone		
2275												Organic claystone		
2276												Coal	2275-2277.1 m. dark gray to black, coaly claystone grading to coal toward the base, generally found carbonaceous mud lamination, coal commonly broken	
2277												Silty claystone		Parallel lamination
2278														
2279													2277.1-2281.0 m. medium to dark gray, silty claystone to claystone, generally found mud lamination disrupted by burrowing, abundance siderite nodules.	

Depth m	Sand					Silt Clay	Sorting			Bioturbation	Lithology	Description	Structures	
	V	C	M	F	Vf		P	M	W					L
2280												Claystone		
2281												Coal	2280.9-2281.0 m. black broken coal	
2282												Claystone	2281-2282.6 m. fining upward, heterolithic sandstone interbedded with claystone grading to claystone toward the top, heterolithic sandstone is light to medium gray, v.fine grained sand, poorly moderately sorted, heavily burrowed traces, poorly laminated	Ripple cross-lamination
												Heterolithic sandstone interbedded with claystone		Ripple cross-lamination
												Organic claystone	2282.6-2282.8 m. Organic claystone, dark gray	-
2283												Sanstone	2282.81-2283.55 m: sandstone, light gray - light brown, sandstone, med-fine grained, poorly to moderately sorted, sub angular-sub rounded, generally found ripple cross-lamination and parallel mud lamination	Ripple cross-lamination
2284												Heterolithic sandstone	2283.55-2288.8 m. heterolithic sandstone, light gray-medium gray, vf grained sand, generally found mud drape lamination, and bi-directional ripple cross-lamination, flaser to more lenticular bedding toward the base, stratification is locally disrupted by burrows	Ripple cross-lamination
2285											Flaser bedding			
2286											Flaser bedding			
2287											Wavy to Lenticular Bedding			
2288											Wavy to Lenticular Bedding			
2289												Silty Claystone	2288.8-2289.6 m. medium to dark gray, silty claystone, generally found mud lamination disrupted by burrowing, abundance siderite nodules	Parallel lamination
2290												Coal	2289.6-2291 m. coal and organic claystone, black to very dark gray, coal grading to coaly claystone, observed broken coal	-
2291												Organic claystone		
2292												Heterolithic Sandstone	2291-2293 m. light-medium gray, heterolithic sandstone mixed with bioturbated claystone, sand is v.fine grained sand, moderately to poorly sorted, abundant parallel mud lamination, mud drape, and ripple cross-lamination, bidirectional ripple-cross lamination, abundant burrowed traces and stratification locally disrupted by burrowing	Flaser to Wavy Bedding Ripple Cross-lamination
2293														

Cored Well : C
Core Depth : 3384.5-3400.5 m
Core Length : 16.0 m
Unit : 2A

Depth m	Febble Granule	Sand					Silt Clay	Sorting			Bioturbation			Lithology	Description	Structures
		VC	C	M	F	Vf		P	M	W	L	M	H			
3385														Organic Claystone	3384.5-3392.1 m: organic claystone, dark to very dark, core samples generally broken, sharp contact at base	
3386																
3387																
3388																
3389																
3390																
3391																
3392													Heterolithic Sandstone		Wavy bedding	
3393													Sandstone Preservation Sandstone Preservation 3393.1-3393.5 m.	3392.1-3396.7 m: coarsening upward, silty claystone grading to heterolithic sandstone, silty claystone is medium to dark gray, generally found clay lamination, siderite nodules, heterolithic sandstone is medium gray, very fine grained sand, moderately-well sorted, rounded generally found bi-directional ripple cross-lamination with mud drape, more mud drape toward the top, abundance bioturbation traces/burrow, gradational contact at base	Ripple cross-lamination	
3394													Sandstone		Ripple cross-lamination	
3395													Silty claystone		Bi-directional ripple cross-lamination	
3396													Organic Claystone Claystone	3396.7-3397.9 m: fining upward, sandstone, light gray, fine to very fine grained sand, moderately-well sorted, rounded, few ripple cross-lamination, no burrow traces, gradind to silty claystone, claystone with abundance root traces, and organic claystone toward the top, erosional surface at base	Gradational contact	
3397													Silty Claystone Sandstone Preservation 3397.1-3397.5 m. Sandstone		Ripple cross-lamination	
															Erosional surface	

Depth	m	Pebble	Granule	Sand					Silt	Clay	Sorting			Bioturbation			Lithology	Description	Structures
				VC	C	M	F	Vf			P	M	W	L	M	H			
3398																			
3399																			
3400																			
3401																			

Cored Well : C
 Core Depth : 3063.7-3082.11 m
 Core Length : 18.41 m
 Unit : 2B

Depth m	Pebble	Granule	Sand					Silt	Clay	Sorting			Bioturbation			Lithology	Description	Structures
			VC	C	M	F	Vf			P	M	W	L	M	H			
3064																		
3065																		
3066																		
3067																		
3068																		
3069																		
3070																		
3071																		
3072																		
3073																		
3074																		
3075																		
3076																		

Depth	Pebble	Granule	Sand					Silt	Clay	Sorting			Bioturbation	Lithology	Description	Structures
			VC	C	M	F	Vf			P	M	W				
3077																
3078														Organic claystone	3077-3080.86 m: organic claystone, dark to v.dark gray, commonly found siderite nodules	
3079																
3080																
3081													Coal	3080.86-3082.11 m: fining upward, silty claystone grading to organic claystone, and coal toward the top, silty claystone and organic claystone is dark gray, coal is broken with sulphur on top		
													Organic claystone			
3082													Silty claystone			

Cored Well : D
 Core Depth : 2781-2817 m
 Core Length : 36 m
 Unit : 2C

Depth m	Pebble	Granule	Sand					Silt	Clay	Sorting			Bioturbation			Lithology	Description	Structures
			VC	C	M	F	Vf			P	M	W	L	M	H			
2781																		
2782																		
2783															Sandstone	2781-2785.5 m: sandstone, coarsening upward, light-medium gray, vf-med grained sand, poor-mod sorting, sub angular-sub rounded, generally found bi-directional ripple cross-lamination, some disrupted by slightly-moderately bioturbation	Bi-directional Ripple cross-lamination	
2784																		
2785																		
2786																		
2787																	Wavy Bedding	
2788																	Wavy Bedding	
2789															Heterolithic Sandstone			
2790																	Wavy Bedding	
2791																		
2792																		
2793																	Wavy Bedding	

Cores were reassembled after falling on rig floor

Depth m	Pebble	Granule	Sand					Silt	Clay	Sorting			Bioturbation			Lithology	Description	Structures
			VC	C	M	F	Vf			P	M	W	L	M	H			
2794																		
2795																	Wavy Bedding	
2796														Heterolithic Sandstone				
2797																	Wavy Bedding	
2798																		
2799																		
2800														Sandstone interbedded with	2800-2802.4 m: sandstone, light-medium gray, fine grained, moderately to well sorted, subrounded to rounded, generally sandstone interbedded with claystone in the upper part and more ripple cross-lamination toward the base, locally thick mud drape, siderite nodules, sharp contact at base	Bi-directional Ripple cross-lamination		
2801													Sandstone					
2802																	Sharp contact	
2803														Silty Claystone	2802.4-2803.4 m: silty claystone toward the base, medium to dark gray, generally found carbonaceous material, siderite nodules			
2804														Claystone	2803.4-2810.1 m: massive claystone grading to coaly claystone and coal toward to the base, medium-dark gray, commonly found siderite nodules			
2805																		
2806																		
2807																		
2808																		
2809														Organic claystone				

Depth m	Pebble	Granule	Sand					Silt	Clay	Sorting			Bioturbation			Lithology	Description	Structures
			VC	C	M	F	Vf			P	M	W	L	M	H			
2810															Coal			
2811															Silty claystone	2810-2815 m: silty claystone grading to coaly claystone toward the base, medium gray to dark gray, generally found siderite nodules and local root traces		
2812																		
2813																		
2814														Organic claystone	2813.4-2815 m: coal grading to coaly claystone, dark to very dark gray, local broken coal			
2815														Coal				
2815														Clayey siltstone	2815-2815.6 m: silty claystone, medium to dark gray, generally found siderite nodules, generally found carbonaceous lamination, sharp contact at base			
2816														Heterolithic Sandstone				
2816														Sandstone	2815.6-2817 m: sandstone, light to medium gray, very fine-fine grained, poorly-moderately sorted, subangular-subrounded, generally found ripple cross-lamination	Ripple cross-lamination		
2817																		

Appendix B-2. Lithofacies Descriptions and Interpretations

1) Coal

Definition

This facies is generally observed as a black to very dark-gray coal as shown in Figure 8-1. Core samples are commonly broken and covered by sulfur mineral that probably originated from the pyrite nodules. There is no obvious sedimentary structure and bioturbation presenting in this rock type. Coal beds are generally thin and stratigraphically above claystone that contains abundant of root traces. The wireline log responses of coal lithofacies show a very distinctive character including a moderate radioactivity (GR 80-130 API), very low bulk density, very high neutron porosity, and very slow sonic (long transit-time).

Interpretation

Coal generally deposited in a swampy depositional environment that contains abundant remnants of trees. Once these trees are buried, they are heated and compressed to form coal. Resulting of palynological and palynofacies analysis found the *Polypodioidites perrucatus* and *Polypodioidites usmensis* pollens, these pollens suggest a shallow water depth and more oxic depositional setting. In addition, the presence of rare *Pediastrum* indicates lakes or ponds, but there is no indicator of marine influence.

2) Organic claystone

Definition

Organic claystone is commonly found as a dark gray to black color (Figure 8-1). This lithofacies has an abundant carbonaceous material and it is significantly denser

than coal. In addition, it locally consists of abundant gastropod and pelecypod fossils that were accumulated in the certain interval. Organic claystone is stratigraphically above coal lithofacies and below sharp-based sandstone. Thin bed gravel lag with the basal erosional surface is locally observed in organic claystone. Organic claystone can be recognized in well-log responses by a high radioactivity (GR>130 API), high bulk density, high neutron porosity, and moderate sonic (moderate transit-time).

Interpretation

The abundances of fine-grained sediments and organic material, as well as the presence of pelecypod and gastropod fossils, indicate that organic claystone was deposited in a low energy setting such as a swamp in upper delta plain. Furthermore, a gravel lag in organic claystone probably suggests an abandoned channel deposit that was filled with clay plug. There are abundant *Pteridophyte* spores and unicellular fungal spores, which usually represent a fluvial setting with slightly shallow water depth. In addition, rare *Acrostichum speciosum* spores also indicate some degrees of tidal and/or marine influence. The depositional setting of organic claystone might be located toward the upper limit of marine influence.

3) *Laminated and bioturbated claystone*

Definition

Laminated and bioturbated claystone is the most abundant lithofacies almost 40% of the core samples. It generally consists of medium to dark gray homogeneous claystone grading into silty claystone. Sedimentary structures mainly include thin (1-3 mm) to very thin (<1 mm) parallel-carbonaceous laminations and some lenticular siltstones. The original laminations are significantly disrupted by burrowing and

rooting. It is locally found both gastropod and pelecypod fossils. Furthermore, there are abundant siderite nodules resulting from pyrite replacement fossil shells form as an elongate shape parallel to bedding. Siderite nodule is a common diagenetic or post-depositional feature in sedimentary rocks. This lithofacies tends to coarsen upward, with the upper contacts grading into overlying heterolithic sandstone lithofacies. In addition, bioturbated claystone to clayey siltstone is stratigraphically above organic claystone or coal lithofacies. Well-log responses of this lithofacies generally occur as a high radioactivity (GR >130 API), high bulk density, moderate neutron porosity, and moderate sonic (moderate transit-time). Resulting from porosity and permeability measurement in core-plug samples reveal that claystone to silty claystone lithofacies does not have any significant reservoir quality. Even though their porosity ranges between 3-9%, permeability is totally less than 0.01 mD.

Interpretation

The presence of fine-grained sediments and parallel-carbonaceous laminations and bioturbations in this lithofacies suggests a low-energy setting. These fine-grained sediments are transported as suspension material in the water column and then they are deposited. The presence of local root traces and bioturbations may indicate the oxic condition.

4) Heterolithic Sandstone

Definition

The heterolithic sandstone lithofacies is composed of very fine-to fine-grained sand, moderate to well sorting, and sub-rounded to rounded. This facies is commonly observed as brownish-gray to medium gray in color. Sedimentary structures include thin

beds (3-10 cm) of wavy to flaser beddings interbedded with abundant mud drapes. Furthermore, it can be observed small-scale ripple cross-laminations, which they occasionally show a bi-directional stratification. The original bedding is highly disrupted by burrowing and rooting as well as it contains some remnants of gastropod fossils. In some intervals, it is easily observed the vertical burrowing structures as presented in Figure 8-1. Heterolithic sandstone is stratigraphically below a laminated claystone to silty claystone lithofacies in a coarsening-upward succession, however, it can be underlain by ripple cross-laminated sandstone in a fining upward succession. In wireline log responses, heterolithic sandstone is relatively low porosity along with moderate to high radioactivity (GR 100-140 API), high bulk density, moderate neutron porosity, and moderate sonic (moderate transit-time). These characters are very similar to claystone and silty claystone lithofacies. These observations significantly correspond to the porosity and permeability measurement in core plug samples. The analysis indicates that heterolithic sandstone has a low reservoir quality, which porosity ranges between 5-12% and permeability is generally less than 0.1 mD.

Interpretation

This lithofacies strongly suggests a tidal process as it presents several exclusive features of tidal deposits including mud drapes, wavy and flaser beddings, and bi-directional cross-stratification. The depositional process requires a combination of a relatively high energy and a relatively low energy conditions that commonly show a cyclic in nature. Flood-ebb currents with intervening slackwater suspensions predominantly create a bundle sequence pattern as observed in the heterolithic sandstone. The presence of vertical burrowing in Figure 8-1 probably represents the

Skolithos ichnofacies, which the original form is approximately vertical cylinder in both J- and U-shaped. The burrow-infilled showing in dark color may also be affected by the presence of tidal currents, which sediments moving near the seabed were trapped in the open burrows. The *Skolithos* trace fossils usually found in a shallow water depth of a marginal marine setting including deltaic or estuarine environments.

5) *Parallel-laminated sandstone*

Definition

Parallel-laminated sandstone is mostly observed near the upper part of a fining upward succession. This facies is generally found as a light to medium gray sandstone that grain sizes range from very fine-to medium-grained sand, moderate to well sorted, and sub-rounded to sub-angular. There are abundant parallel-mud laminations that commonly less than 1 cm (0.03 ft). In addition, mud drapes are commonly observed in this sandstone facies. Bioturbation is generally absent. In wireline logs, this facies is a moderate radioactivity (GR 100-130 API), moderate bulk density, moderate neutron porosity, and moderate sonic (transit-time). The result of porosity and permeability measurement in core samples also indicate that porosity in parallel-laminated sandstone facies is about 15 to 17%, while permeability is generally below 1 mD.

Interpretation

The presence of fine-grained sediments, parallel mud-laminations, and mud drapes in this lithofacies suggests a relatively low energy setting. This evidence probably indicates a tide- influenced deposition, which mud laminations and mud drapes fallen out from suspension in water during slack tide. Therefore, this facies is

interpreted as a late stage of fluvial deposit in distributary channel with some tidal influences. The depositional environment could be located in lower delta plain.

6) Ripple cross-laminated sandstone

Definition

Ripple cross-laminated sandstone generally occurs as light to medium gray in color. It consists of very fine-to fine-grained sand, low to moderate sorting, and sub-rounded to sub-angular. Ripple cross-laminations are a key sedimentary structure that occurs on a very small-scale cross-lamination commonly less than 1 cm (0.03 ft). Asymmetrical ripples and most of them generally dip in opposite directions. Herringbone cross-stratification is locally observed in this facies as presented in Figure 8-2. Sandstone contains abundant mud laminations that mostly form a flaser bedding. In addition, the original bedding is commonly disrupted by a vertical shape burrowing. In general, ripple cross-lamination sandstone lithofacies can be found in both fining-and coarsening-upward successions. This facies usually overlies on claystone with a basal erosional surface in fining-upward succession as well as there is often overlain by poorly-bedded heterolithic sandstone lithofacies in a coarsening-upward succession. In wireline logs, this facies is characterized by a moderate radioactivity (GR 100-130 API), moderate bulk density, moderate neutron porosity, and moderate sonic (transit-time). The measurement of core plug samples indicates that ripple cross-laminated sandstone lithofacies has a very wide range of both porosity and permeability. Porosity generally ranges from 4% to 21%, while permeability varies from 5 to about 40 mD.

Interpretation

The presence of fine-grained sediments, opposite dipping of ripple cross-laminations, and abundant burrowing traces in this lithofacies suggests a low energy with different current directions. Ripple cross-laminations causing a flaser bedding commonly exhibits bi-directional cross-stratifications that might indicate tidal currents (flood-ebb tides). Therefore, this facies is interpreted as tidal channel-filled in fining-upward succession and distributary mouth bar deposit in coarsening-upward succession. These kinds of depositions are mainly located between lower delta plain to delta front area.

7) *Cross-bedded sandstone*

Definition

This facies is a light to medium gray sandstone that grain sizes vary from medium-to coarse-grained sand, moderate to well sorted, and subrounded to subangular. The individual thickness is approximately 2-3 m (6.6-9.8 ft). Trough cross-bedding is a key sedimentary structure, which bed sets generally occur on a small scale ranging from 1-2 m (3.3 to 9.8 ft). There are usually formed as the inclined dark layers of fine-grained carbonaceous material and locally interrupted by reactivation surfaces. Bioturbation is generally absent. Typically, trough cross-bedding sandstone is stratigraphically above basal conglomerate containing abundant claystone rip-up clasts in a fining-upward succession. In well-logs, this lithofacies is recognized by a low radioactivity (GR 50-90 API), low bulk density, moderate neutron porosity, and slow sonic (slow transit-time). These log characters also suggest that cross-bedded sandstone has a good reservoir

quality as observed from porosity and permeability testing in core samples. It has a wide range of porosity between 12-24%, while permeability also varies from about 2 mD to almost 450 mD.

Interpretation

The presence of coarser grain sediments and cross-bedding structures in this lithofacies suggests a relatively high energy current regime for sedimentation. The lack of mud drapes and laminations is no obvious indication of a tidal dominance. Therefore, this facies is interpreted as a fluvial deposit of distributary channel, which mainly occurs in the upper delta plain. The cross-bedding appears to be predominantly pointed to a downstream direction. This facies is considered to be the most important reservoir within early to middle Miocene Formation 2.

8) *Structureless sandstone*

Definition

This facies occurs as a light to medium gray sandstone that grain sizes are composed of medium to coarse-grained sands, moderate to well sorting, and sub-rounded to rounded. There is no obvious sedimentary structure, so this facies is named as structureless sandstone. Bioturbation is totally absent. Claystone rip-up clasts are locally found inside this facies. Generally, structureless sandstone is described stratigraphically above trough cross-bedded sandstone and forms a well-defined fining upward succession. In wireline logs, structureless sandstone is characterized by a low radioactivity (GR 50-90 API), low bulk density, moderate neutron porosity, and slow sonic (slow transit-time). It can be observed a cross-over between neutron porosity and bulk density curves. These responses are very similar to cross-bedded sandstone. In

addition, porosity and permeability measurement in core samples show that structureless sandstone has a high porosity ranging from 14 to 22%, while permeability also ranges from 25 to almost 450 mD.

Interpretation

The presence of coarser grain sediments with well sorting and the lack of mud laminations and bioturbations in structureless sandstone facies indicates sedimentation in a setting with more constant high energy currents. According to facies successions in core samples, this facies is stratigraphically above cross-bedded sandstone. Therefore, structureless sandstone is interpreted as same as cross-bedded sandstone that represents fluvial deposits of distributary channel. This depositional environment is located in the upper delta plain.

9) Conglomerate

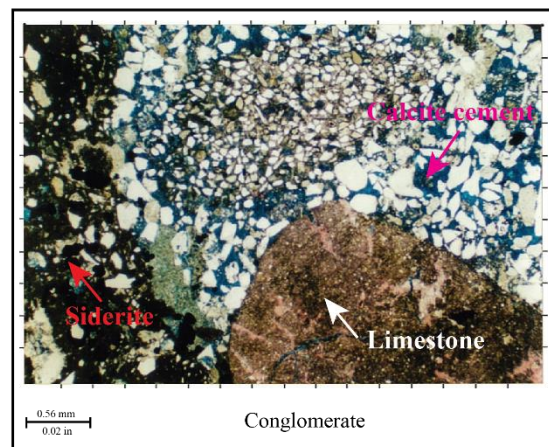
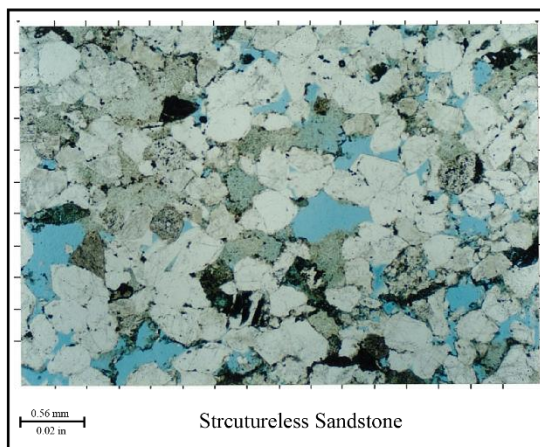
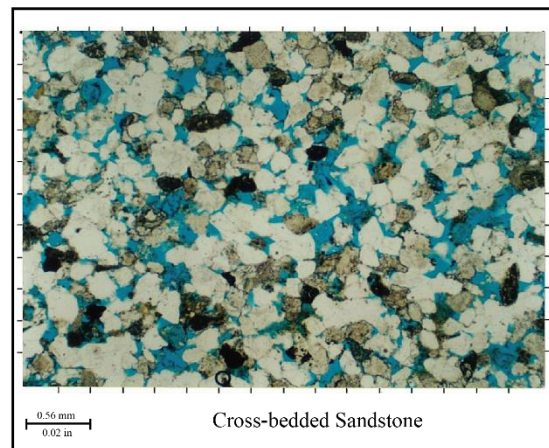
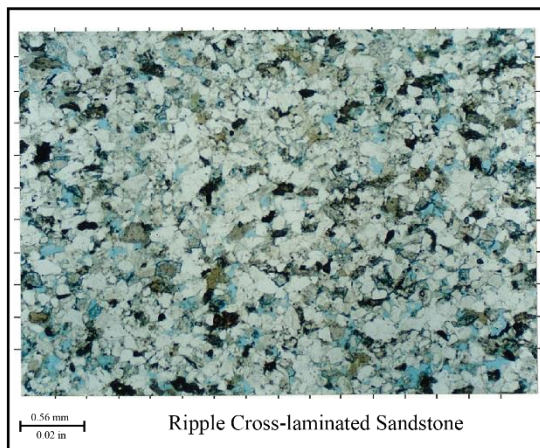
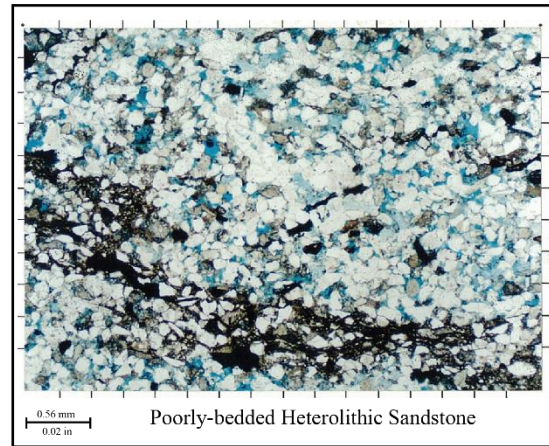
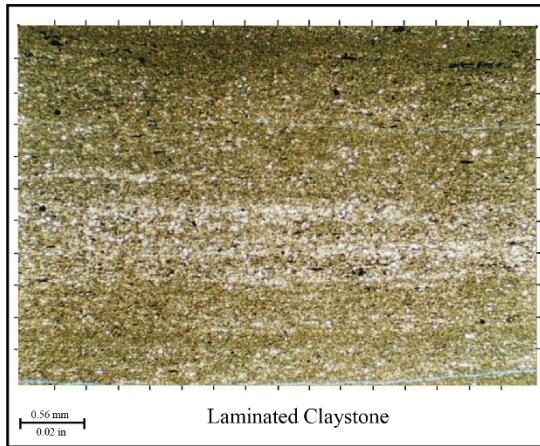
Definition

This facies is a clast-supported conglomerate (orthoconglomerate) containing granule to pebble-grained of mudstone. These clasts are gray to reddish brown claystone color, angular to rounded, and poor to moderate sorting. They are commonly cemented by carbonate that strongly reacts to hydrochloric (HCL) acid. The main composition of these clasts observed in photomicrographs is quartz, while rock fragments mainly consist of limestone, dolostone, claystone, and siderite (Figure 9). In addition, cementation is predominantly composed of siderite and ferroan calcite. The wireline log characters of conglomerate facies are recognized by a low radioactivity (GR 50-90 API), high bulk density, moderate neutron porosity, and moderate sonic (moderate transit-time). It can be observed that bulk density value presenting in the

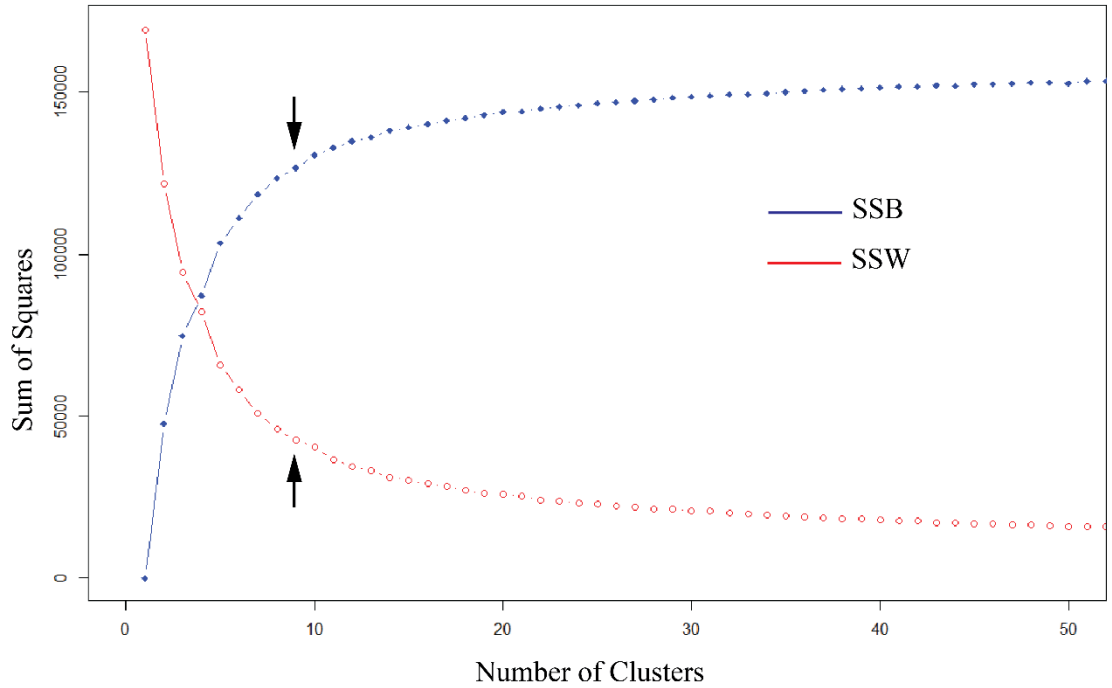
conglomerate is moderately higher than cross-bedded sandstone and structureless sandstone. Conglomerate lithofacies has a basal erosional surface and it is stratigraphically below trough cross-bedded sandstones and structureless sandstone in a fining upward succession. Moreover, this facies can be found as a thin gravel lag bed, approximately 5 cm (0.16 ft) thick, within organic claystone facies.

Interpretation

This facies is interpreted as a mixed-load fluvial deposit, which commonly formed near the thalweg as a channel lag. The sediment clasts are in contact with the sediment beds and move by traction. Mudstone clasts are probably derived from channel undercutting of floodplain sediments. In addition, the gravel lag bed occurring within organic claystone could represent the channel lag over the abandoned channel. Therefore, conglomerate facies is interpreted as fluvial deposits of distributary channels in upper delta plain.



Appendix B-3. Representative thin-section photomicrographs.



Appendix B-4. The plot of Sum-of-Squares Between (SSB) and Sum-of-Squares Within (SSW) against the number of clusters (K). A SSW plot indicates the cumulative distance of each point to its centroid with increasing K values. As more classes are added (increasing K), the distance between centroids and data points significantly decreases. A SSB plot compares the cumulative distance between centroids to the global mean centroid, with increasing K values. The optimal K value is at the inflection point where the slope of the SSW and SSB plots decrease, known as the elbow point (arrows). In this study, the elbow point does not show a sharp decline; therefore, the number of clusters (K) is selected at 9.

ANNs Predicted Lithofacies 45% overall accuracy	Actual Lithofacies								
	Coal	Organic Claystone	Laminated and Bioturbated Claystone	Heterolithic Sandstone	Parallel-laminated Sandstone	Ripple Cross-laminated Sandstone	Cross-bedded Sandstone	Structureless Sandstone	Conglomerate
Coal	2	0	0	0	0	0	0	0	0
Organic Claystone	1	7	42	0	0	0	0	0	0
Laminated and Bioturbated Claystone	15	30	143	33	4	3	0	0	0
Heterolithic Sandstone	0	2	11	35	14	4	2	0	0
Parallel-laminated Sandstone	0	0	0	0	0	0	0	0	0
Ripple Cross-laminated Sandstone	0	0	0	0	9	4	27	14	3
Cross-bedded Sandstone	0	0	0	0	9	7	3	0	0
Structureless Sandstone	0	0	0	0	0	0	0	0	0
Conglomerate	0	0	0	0	0	0	0	0	0
User's Accuracy (%)	11%	18%	73%	51%	0%	22%	9%	0%	0%

K-means Predicted Lithofacies 43% overall accuracy	Actual Lithofacies								
	Coal	Organic Claystone	Laminated and Bioturbated Claystone	Heterolithic Sandstone	Parallel-laminated Sandstone	Ripple Cross-laminated Sandstone	Cross-bedded Sandstone	Structureless Sandstone	Conglomerate
Coal	0	0	0	0	0	0	0	0	0
Organic Claystone	1	14	51	0	0	0	0	0	0
Laminated and Bioturbated Claystone	15	19	96	4	0	0	0	0	0
Heterolithic Sandstone	0	4	43	34	2	0	0	0	0
Parallel-laminated Sandstone	2	2	6	30	22	16	3	0	0
Ripple Cross-laminated Sandstone	0	0	0	0	0	0	0	0	0
Cross-bedded Sandstone	0	0	0	0	12	2	11	9	1
Structureless Sandstone	0	0	0	0	0	0	18	5	2
Conglomerate	0	0	0	0	0	0	0	0	0
User's Accuracy (%)	0%	36%	49%	50%	61%	0%	34%	36%	0%

Appendix B-5. Lithofacies confusion matrices for each electrofacies classification method using the GR and RESD input assemblage.

ANNs Predicted Lithofacies 52% overall accuracy	Actual Lithofacies								
	Coal	Organic Claystone	Laminated and Bioturbated Claystone	Heterolithic Sandstone	Parallel-laminated Sandstone	Ripple Cross-laminated Sandstone	Cross-bedded Sandstone	Structureless Sandstone	Conglomerate
Coal	10	1	2	0	0	0	0	0	0
Organic Claystone	1	6	24	0	0	0	0	0	0
Laminated and Bioturbated Claystone	7	30	166	38	2	0	0	0	0
Heterolithic Sandstone	0	2	4	29	9	1	0	0	0
Parallel-laminated Sandstone	0	0	0	0	0	0	0	0	0
Ripple Cross-laminated Sandstone	0	0	0	0	11	5	24	14	3
Cross-bedded Sandstone	0	0	0	1	14	12	8	0	0
Structureless Sandstone	0	0	0	0	0	0	0	0	0
Conglomerate	0	0	0	0	0	0	0	0	0
User's Accuracy (%)	56%	15%	85%	43%	0%	28%	25%	0%	0%

K-means Predicted Lithofacies 47% overall accuracy	Actual Lithofacies								
	Coal	Organic Claystone	Laminated and Bioturbated Claystone	Heterolithic Sandstone	Parallel-laminated Sandstone	Ripple Cross-laminated Sandstone	Cross-bedded Sandstone	Structureless Sandstone	Conglomerate
Coal	0	0	0	0	0	0	0	0	0
Organic Claystone	0	0	0	0	0	0	0	0	0
Laminated and Bioturbated Claystone	13	36	128	11	1	0	1	0	0
Heterolithic Sandstone	0	2	67	57	13	9	20	0	0
Parallel-laminated Sandstone	0	0	0	0	0	0	0	0	0
Ripple Cross-laminated Sandstone	0	0	0	0	0	0	0	0	0
Cross-bedded Sandstone	5	1	1	0	22	9	11	9	1
Structureless Sandstone	0	0	0	0	0	0	0	5	2
Conglomerate	0	0	0	0	0	0	0	0	0
User's Accuracy (%)	0%	0%	65%	84%	0%	0%	34%	36%	0%

Appendix B-6. Lithofacies confusion matrices for each electrofacies classification method using the GR, RESD, and RHOB input assemblage.

ANNs Predicted Lithofacies 47% overall accuracy	Actual Lithofacies								
	Coal	Organic Claystone	Laminated and Bioturbated Claystone	Heterolithic Sandstone	Parallel-laminated Sandstone	Ripple Cross-laminated Sandstone	Cross-bedded Sandstone	Structureless Sandstone	Conglomerate
Coal	10	0	2	0	0	0	0	0	0
Organic Claystone	1	5	32	0	0	0	0	0	0
Laminated and Bioturbated Claystone	7	30	162	45	6	0	0	0	0
Heterolithic Sandstone	0	3	0	17	1	0	0	0	0
Parallel-laminated Sandstone	0	0	0	0	0	0	0	0	0
Ripple Cross-laminated Sandstone	0	0	0	0	9	5	25	14	3
Cross-bedded Sandstone	0	1	0	6	20	13	7	0	0
Structureless Sandstone	0	0	0	0	0	0	0	0	0
Conglomerate	0	0	0	0	0	0	0	0	0
User's Accuracy (%)	56%	13%	83%	25%	0%	28%	22%	0%	0%

K-means Predicted Lithofacies 48% overall accuracy	Actual Lithofacies								
	Coal	Organic Claystone	Laminated and Bioturbated Claystone	Heterolithic Sandstone	Parallel-laminated Sandstone	Ripple Cross-laminated Sandstone	Cross-bedded Sandstone	Structureless Sandstone	Conglomerate
Coal	8	0	1	0	0	0	0	0	0
Organic Claystone	0	0	0	0	0	0	0	0	0
Laminated and Bioturbated Claystone	9	30	111	0	0	0	0	0	0
Heterolithic Sandstone	1	6	81	53	7	1	0	0	0
Parallel-laminated Sandstone	0	2	1	0	1	0	0	0	0
Ripple Cross-laminated Sandstone	0	0	0	0	0	0	0	0	0
Cross-bedded Sandstone	0	1	2	15	28	17	32	14	3
Structureless Sandstone	0	0	0	0	0	0	0	0	0
Conglomerate	0	0	0	0	0	0	0	0	0
User's Accuracy (%)	44%	0%	57%	78%	3%	0%	100%	0%	0%

Appendix B-7. Lithofacies confusion matrices for each electrofacies classification method using the GR, RESD, RHOB, and NPOR input assemblage.

ANNs Predicted Lithofacies 48% overall accuracy	Actual Lithofacies								
	Coal	Organic Claystone	Laminated and Bioturbated Claystone	Heterolithic Sandstone	Parallel-laminated Sandstone	Ripple Cross-laminated Sandstone	Cross-bedded Sandstone	Structureless Sandstone	Conglomerate
Coal	12	0	2	0	0	0	0	0	0
Organic Claystone	1	5	39	0	0	0	0	0	0
Laminated and Bioturbated Claystone	5	30	151	36	2	0	0	0	0
Heterolithic Sandstone	0	3	3	27	6	0	0	0	0
Parallel-laminated Sandstone	0	0	0	0	0	0	0	0	0
Ripple Cross-laminated Sandstone	0	0	1	0	3	2	24	14	3
Cross-bedded Sandstone	0	1	0	5	25	16	8	0	0
Structureless Sandstone	0	0	0	0	0	0	0	0	0
Conglomerate	0	0	0	0	0	0	0	0	0
User's Accuracy (%)	67%	13%	77%	40%	0%	11%	25%	0%	0%

K-means Predicted Lithofacies 43% overall accuracy	Actual Lithofacies								
	Coal	Organic Claystone	Laminated and Bioturbated Claystone	Heterolithic Sandstone	Parallel-laminated Sandstone	Ripple Cross-laminated Sandstone	Cross-bedded Sandstone	Structureless Sandstone	Conglomerate
Coal	4	0	0	0	0	0	0	0	0
Organic Claystone	0	0	3	0	0	0	0	0	0
Laminated and Bioturbated Claystone	14	34	98	2	0	0	0	0	0
Heterolithic Sandstone	0	2	92	48	6	1	0	0	0
Parallel-laminated Sandstone	0	2	0	0	2	0	1	1	0
Ripple Cross-laminated Sandstone	0	0	0	0	0	0	0	0	0
Cross-bedded Sandstone	0	1	3	18	28	17	31	13	3
Structureless Sandstone	0	0	0	0	0	0	0	0	0
Conglomerate	0	0	0	0	0	0	0	0	0
User's Accuracy (%)	22%	0%	50%	71%	6%	0%	97%	0%	0%

Appendix B-8. Lithofacies confusion matrices for electrofacies classification method using the GR, RESD, RHOB, NPOR, and DT input assemblage.

ANNs Predicted Lithologies 73% overall accuracy	Actual Lithology			
	Coal	Claystone	Heterolithic Sandstone	Sandstone
Coal	46	2	0	0
Claystone	6	176	12	6
Heterolithic Sandstone	2	26	8	8
Sandstone	10	30	8	62
User's Accuracy (%)	72%	75%	29%	82%

K-means Predicted Lithologies 60% overall accuracy	Actual Lithology			
	Coal	Claystone	Heterolithic Sandstone	Sandstone
Coal	0	0	0	0
Claystone	16	154	2	4
Heterolithic Sandstone	12	36	16	2
Sandstone	36	44	10	70
User's Accuracy (%)	0%	66%	57%	92%

Appendix B-9. Lithology confusion matrices for electrofacies classification method using the GR and RESD input assemblage.

ANNs Predicted Lithologies 81% overall accuracy	Actual Lithology			
	Coal	Claystone	Heterolithic Sandstone	Sandstone
Coal	48	2	0	0
Claystone	6	202	10	6
Heterolithic Sandstone	0	8	16	12
Sandstone	10	22	2	58
User's Accuracy (%)	75%	86%	57%	76%

K-means Predicted Lithologies 61% overall accuracy	Actual Lithology			
	Coal	Claystone	Heterolithic Sandstone	Sandstone
Coal	8	2	0	0
Claystone	50	154	2	4
Heterolithic Sandstone	4	68	24	14
Sandstone	2	10	2	58
User's Accuracy (%)	13%	66%	86%	76%

Appendix B-10. Lithology confusion matrices for electrofacies classification method using the GR, RESD, and RHOB input assemblage.

ANNs Predicted Lithologies 85% overall accuracy	Actual Lithology			
	Coal	Claystone	Heterolithic Sandstone	Sandstone
Coal	50	2	0	0
Claystone	6	214	10	6
Heterolithic Sandstone	0	4	18	10
Sandstone	8	14	0	60
User's Accuracy (%)	77%	91%	64%	79%

K-means Predicted Lithologies 69% overall accuracy	Actual Lithology			
	Coal	Claystone	Heterolithic Sandstone	Sandstone
Coal	42	2	0	0
Claystone	6	166	8	2
Heterolithic Sandstone	2	46	10	14
Sandstone	14	20	10	60
User's Accuracy (%)	66%	71%	36%	79%

Appendix B-11. Lithology confusion matrices for electrofacies classification method using the GR, RESD, RHOB, and NPOR input assemblage.

ANNs Predicted Lithologies 86% overall accuracy	Actual Lithology			
	Coal	Claystone	Heterolithic Sandstone	Sandstone
Coal	50	2	0	0
Claystone	10	216	10	8
Heterolithic Sandstone	0	0	18	6
Sandstone	4	16	0	62
User's Accuracy (%)	78%	92%	64%	82%

K-means Predicted Lithologies 64% overall accuracy	Actual Lithology			
	Coal	Claystone	Heterolithic Sandstone	Sandstone
Coal	10	4	0	0
Claystone	38	172	8	2
Heterolithic Sandstone	0	42	12	10
Sandstone	16	16	8	64
User's Accuracy (%)	16%	74%	43%	84%

Appendix B-12. Lithology confusion matrices for electrofacies classification method using the GR, RESD, RHOB, NPOR, and DT input assemblage.

Appendix C: Stratigraphic and Structural Framework

Appendix C-1. Well-log attribute analysis

Seismic attributes have been commonly used in the petroleum industry to enhance the information that might preserve in a traditional seismic image, leading to a better geological or geophysical interpretation of the data (Chopra and Marfurt, 2007). On the other hand, a conventional well-log has become less popular to emphasize or extract any preserved geological information. Therefore, this study examines log-attribute to highlight the significant geological detail by using Derivative Trend Analysis (DTA) in the petrophysical module of *Techlog* software.

The principal concept of this analysis is to highlight the log signatures that are hardly observed from the actual measurement values in each certain log. Gamma-ray (GR) is one of the most useful logs for lithology interpretation and sequence stratigraphic analysis, and it is acquired in all wells within the study area. GR log contains much geological information such as lithologies, facies successions, and depositional environments. This is very crucial information for reservoir characterization study.

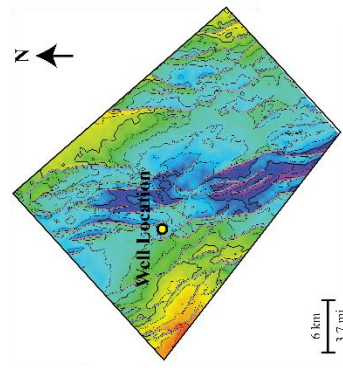
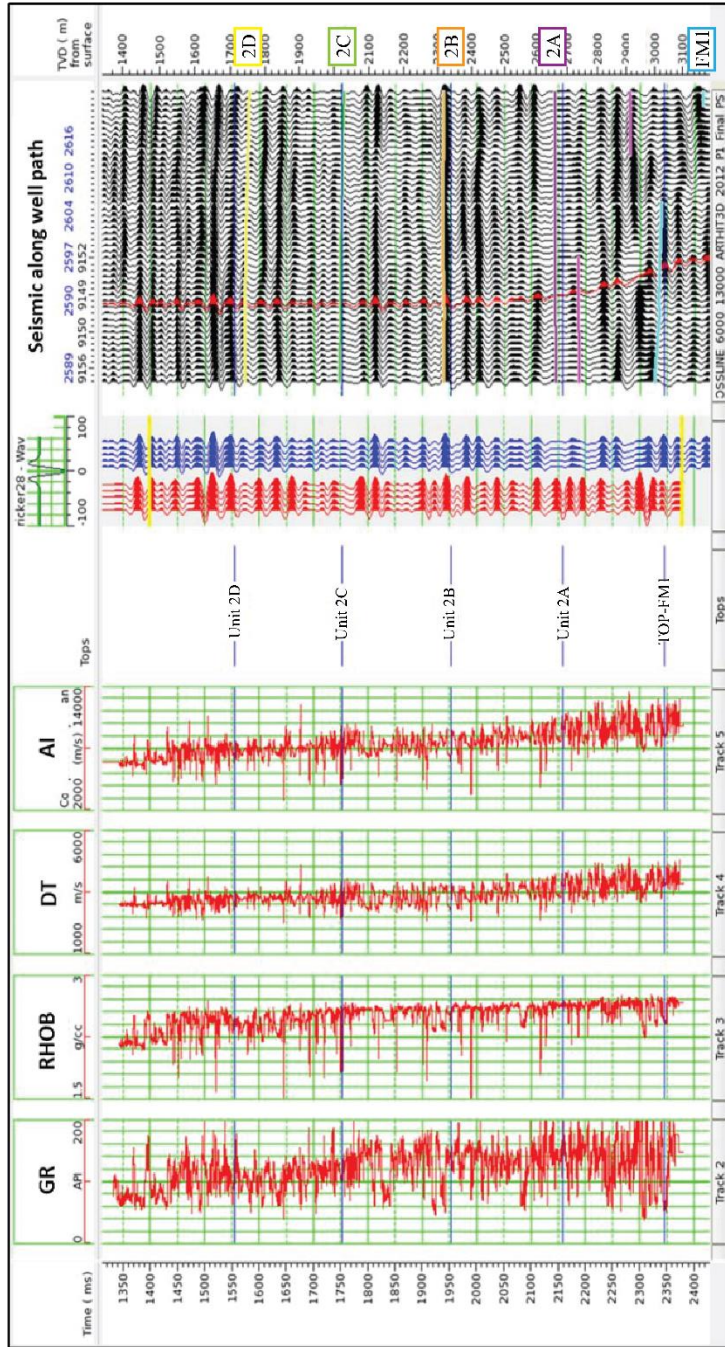
The DTA process consists of two important steps, in which the first step is to define the appropriate frequency or window for smoothing. This is also known as a Gaussian smoothing function, which is widely used in the fields of signal and graphics software to reduce the random noise (Guo, 2011). In smoothing process, the data points within a user-defined smoothing window are modified as a weighted average of its neighboring points. The filter attenuates high-frequency “noise” while keeping lower frequency trends, resulting in smoothing log curves. As long as the true underlying

value is smooth, then the true value will not be distorted. The second step is to differentiate how this smoothed curve changes by using the central-difference method;

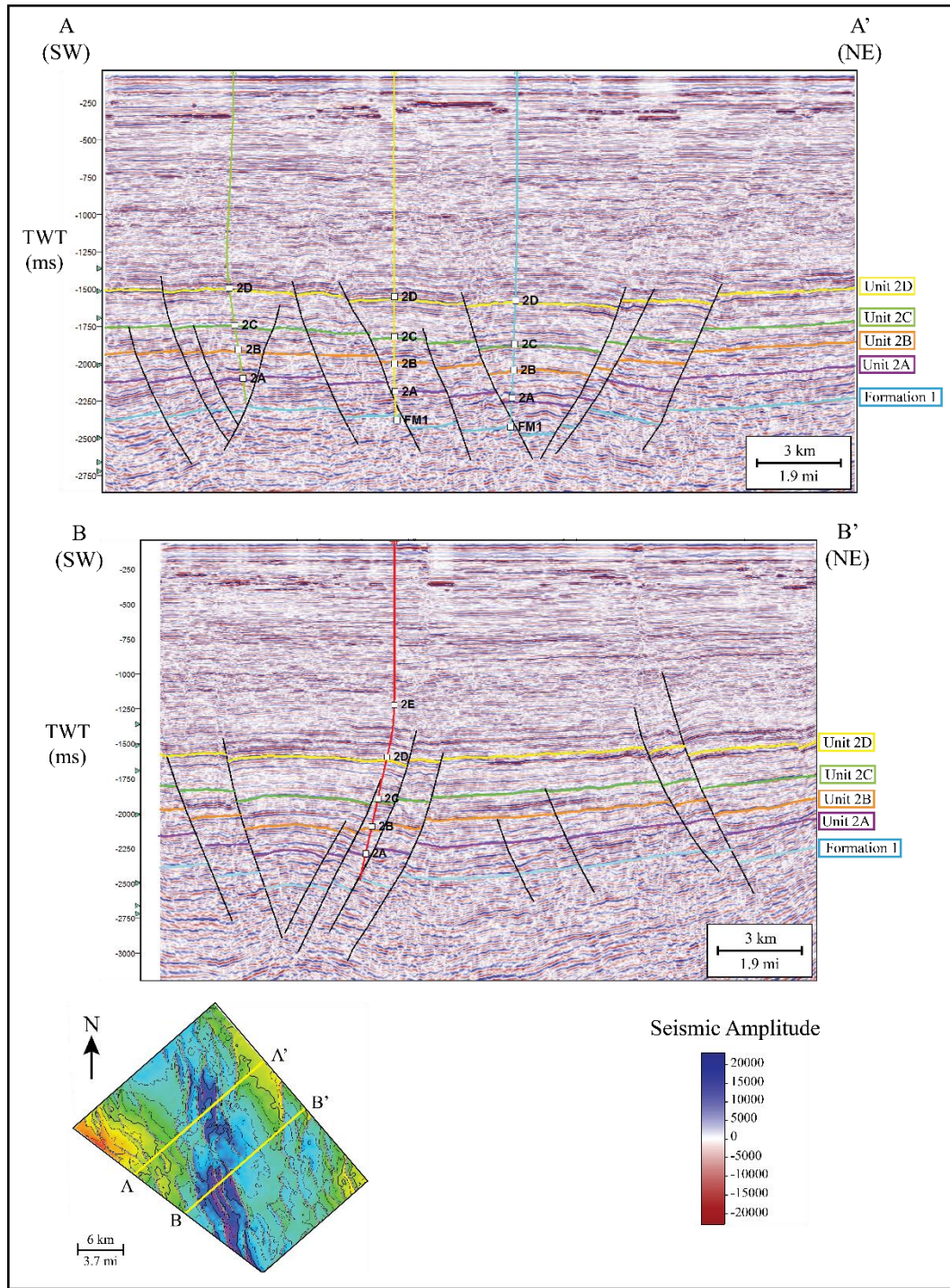
$$\text{Derivative}(i) = \frac{(\text{Value}(i + 1) + \text{Value}(i - 1))}{(\text{Depth}(i + 1) - \text{depth}(i - 1))}$$

This method basically determines the slope changing between nearby points on a smoothed curve. Once the derivative at each point is calculated, a curve will result in either a positive trend or a negative trend. A positive trend curve corresponds to a decreasing upward of the original curve, whereas a negative trend curve correlates to an increasing upward of the original curve (Wethington, 2017). In addition, the magnitude of the derivative curve also emphasizes how fast the original curve is changing.

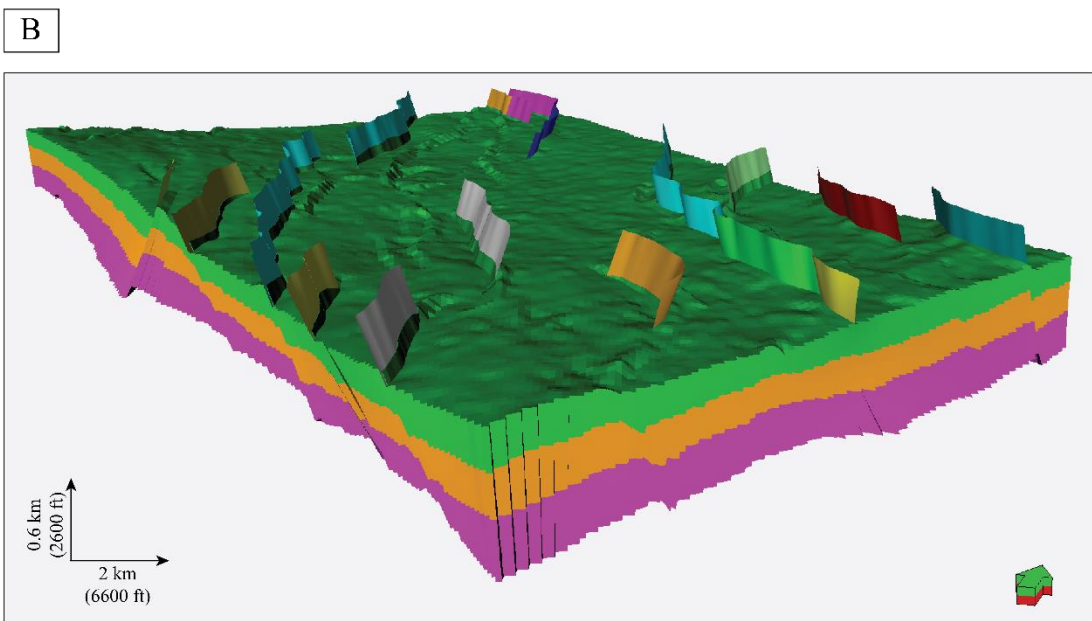
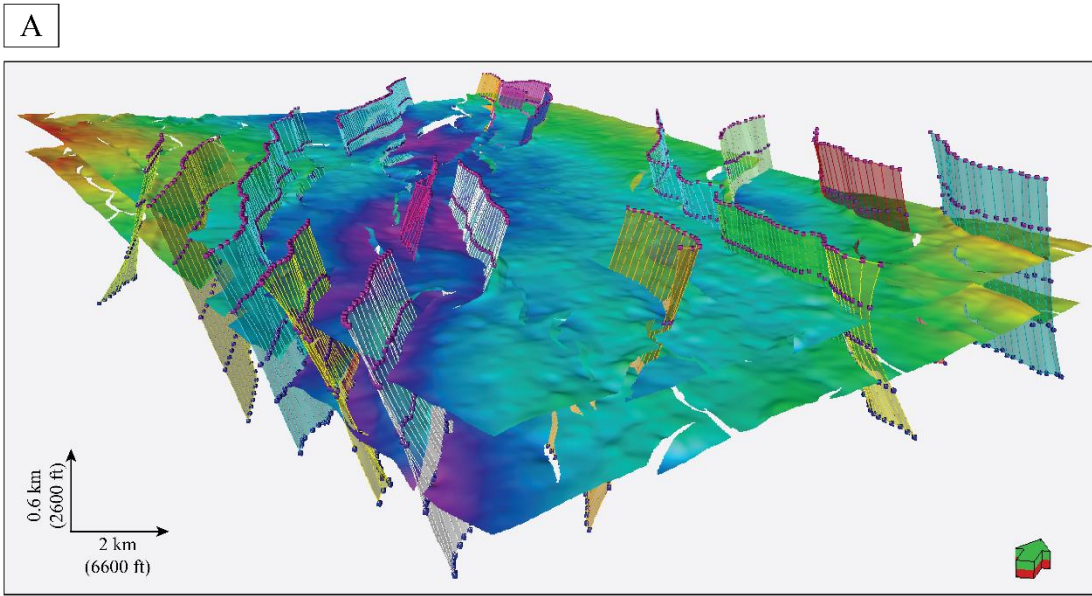
In the context of this study area, the low GR values indicate to sandstone lithology while the high GR values relate to claystone lithology. Consequently, the decreasing-upward of GR values may indicate the cleaning-upward motif that clay content decreases upwards. In contrast, the increasing-upward of GR values could suggest the fining-upward motif that clay content increases upward. The marine flooding surfaces are recognized as an abrupt-upward increase in clay content.



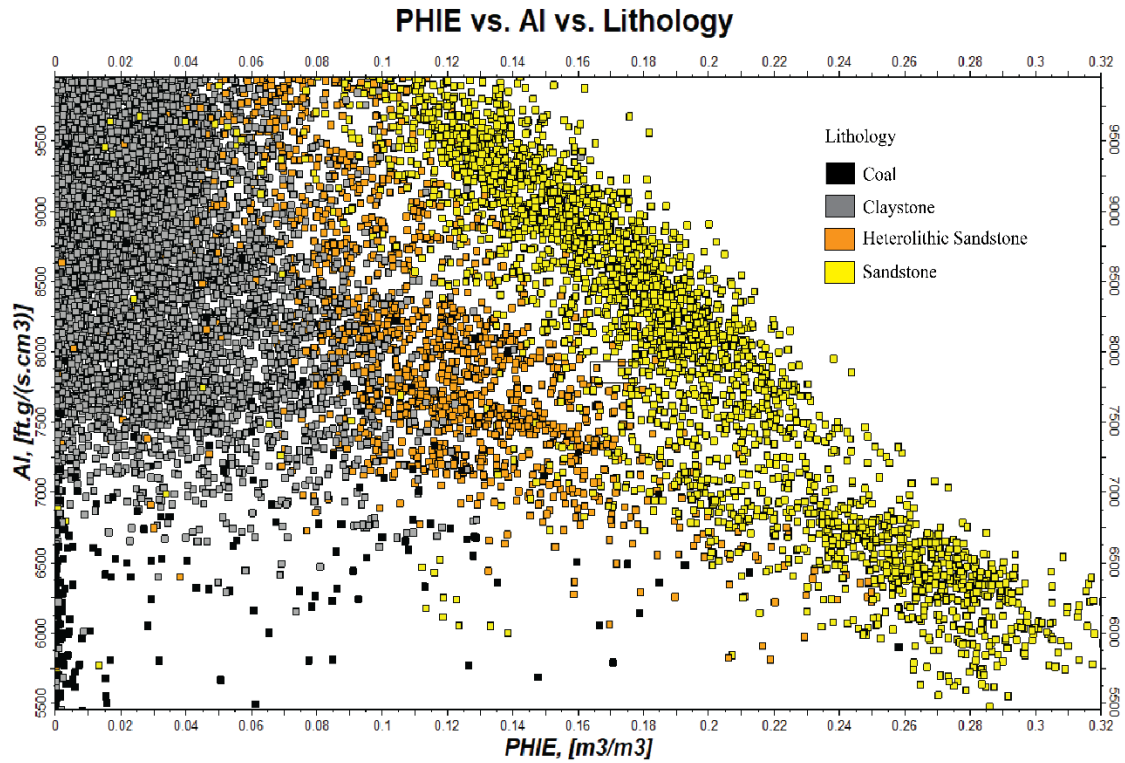
Appendix C-2. A synthetic seismogram is calculated by using velocity from VSP first arrival time and well-log, including gamma ray (GR), bulk density (RHOB), sonic (DT), and acoustic impedance (AI). 3-D seismic has a good tie with synthetic seismogram, which the maximum correlation is 0.505 and correlation window is 1400-2350 msec.



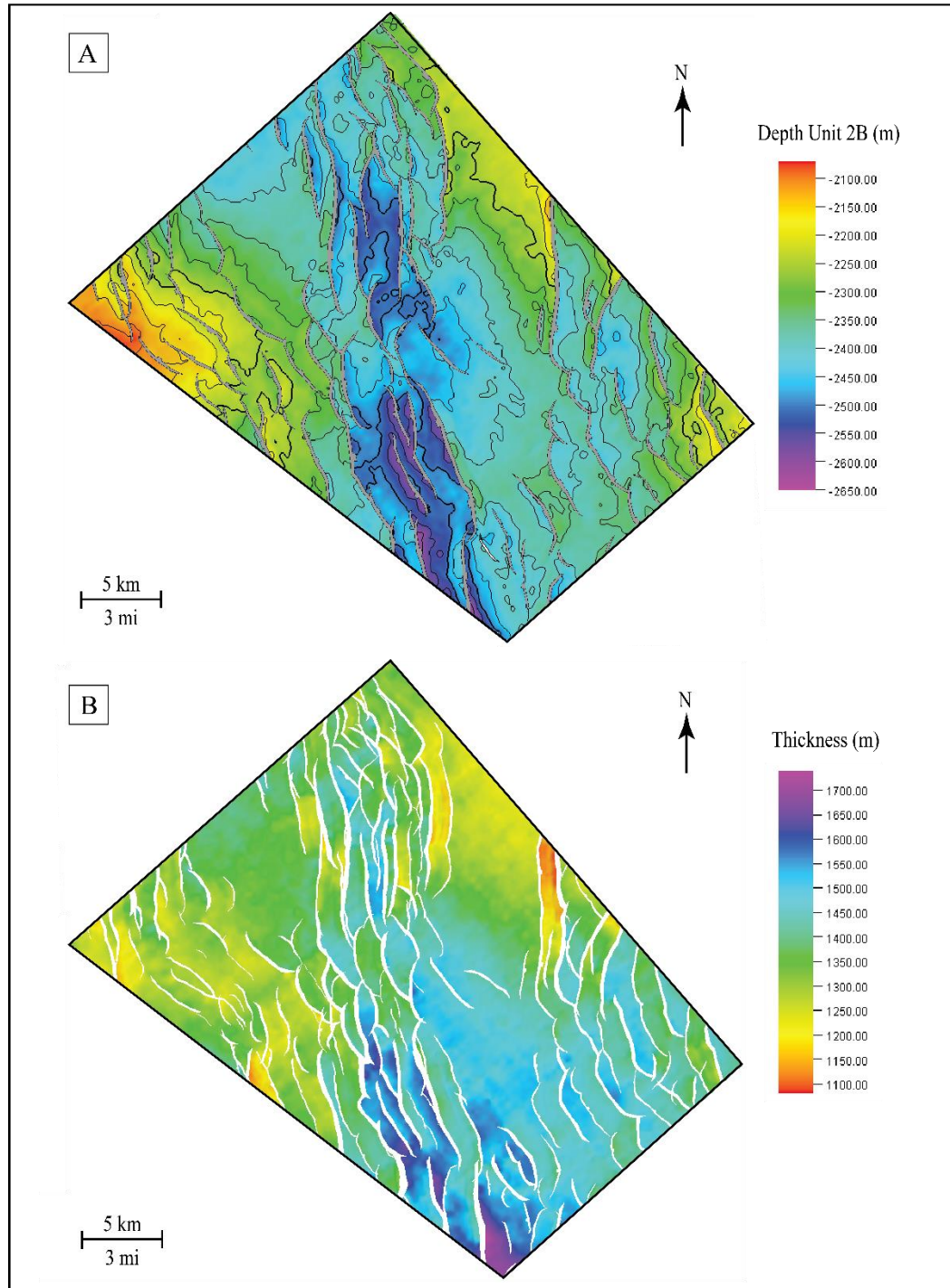
Appendix C-3. Seismic cross-sections with wells that are used for a wells-to-seismic tie in commercial software. These cross-sections include the interpreted faults provided by PTTEP and five horizons representing the tops of the units 2D-A and Formation 1.



Appendix C-4. A structural framework A) incorporates the major faults and depth-surface maps. B) 3-D grid shows a vertical offset after including some normal faults. These grid cells are parallel with the fault surfaces and they do not contain any negative cell or upside-down orientation.



Appendix C-5. A cross-plot of acoustic impedance versus porosity (as calculated from the sonic and density logs) and color coded by lithology does not indicate a relationship between sandstone and acoustic impedance value. All lithologies, including coal, claystone, heterolithic sandstone, and sandstone, are overlapped with each other at the same acoustic impedance values.

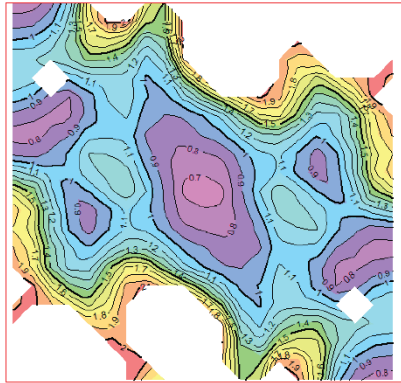


Appendix C-6. A) Structural-contour map of unit 2B based on seismic and well-log data shows the structural pattern and the increasing in elevation depth toward the central graben structure. B) The isopach map of the focusing interval illustrates the overall thickness gradually increasing from the central graben trend toward the southern part of the study area.

Appendix D: Variogram

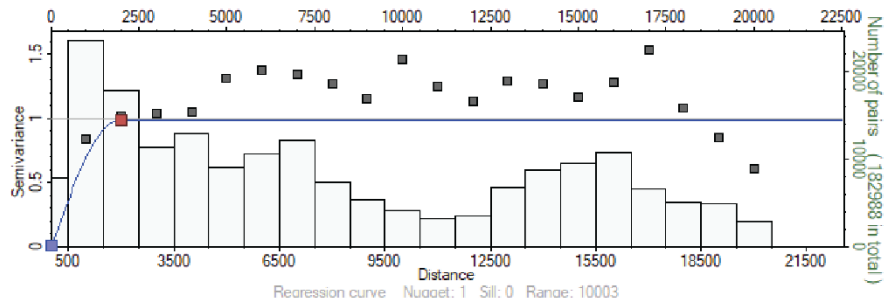
Appendix D-1

Variogram Map

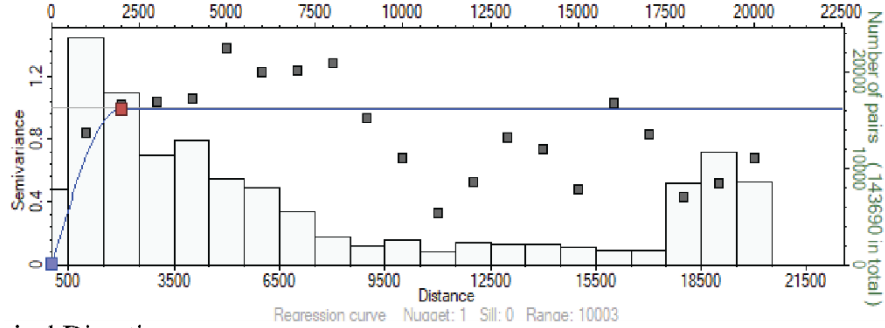


Unit 2D: Coal	
Azimuth (deg)	310
Major range (m)	2000
Minor range (m)	2000
Vertical range (m)	12

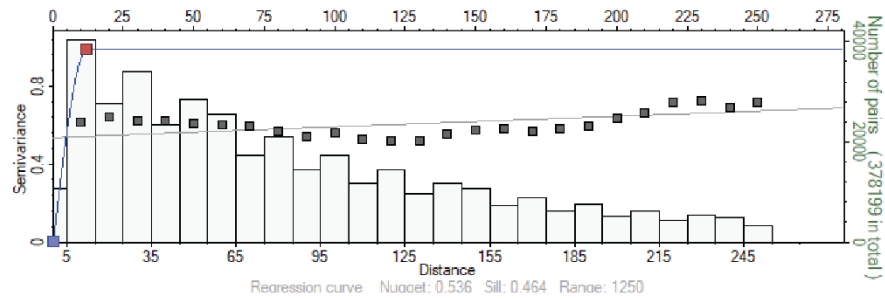
Major Direction



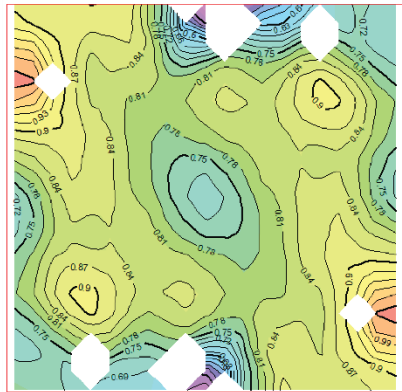
Minor Direction



Vertical Direction

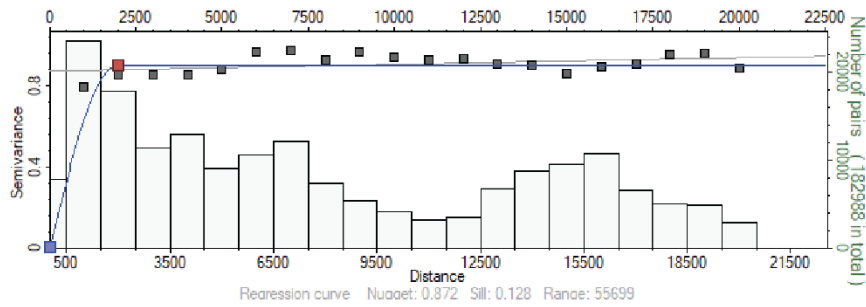


Variogram Map

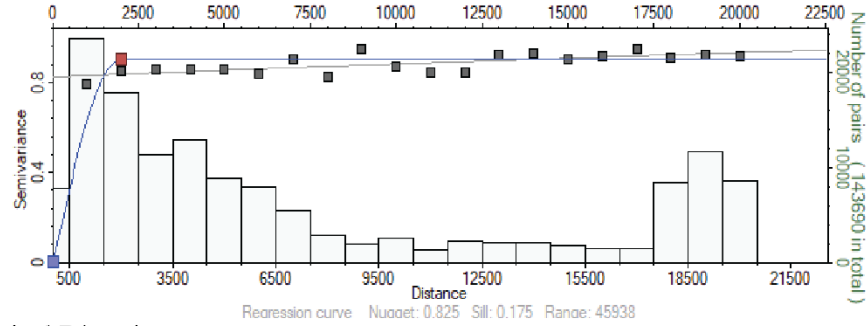


Unit 2D: Claystone	
Azimuth (deg)	310
Major range (m)	2000
Minor range (m)	2000
Vertical range (m)	15

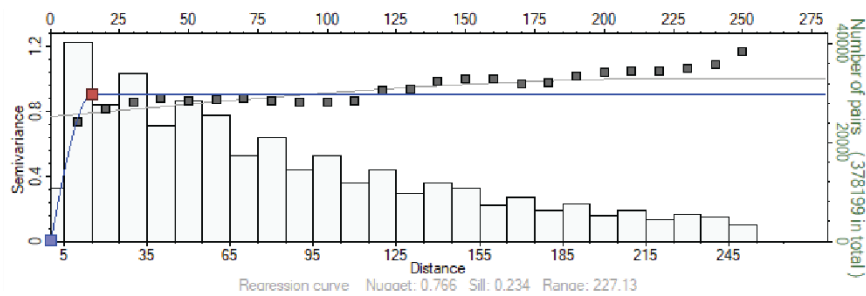
Major Direction



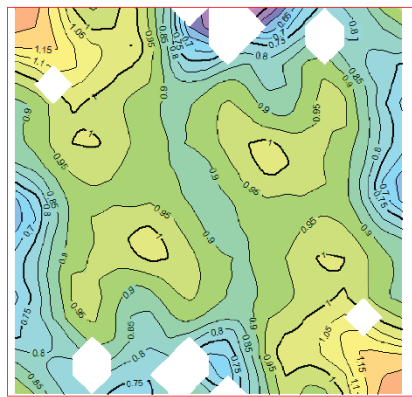
Minor Direction



Vertical Direction

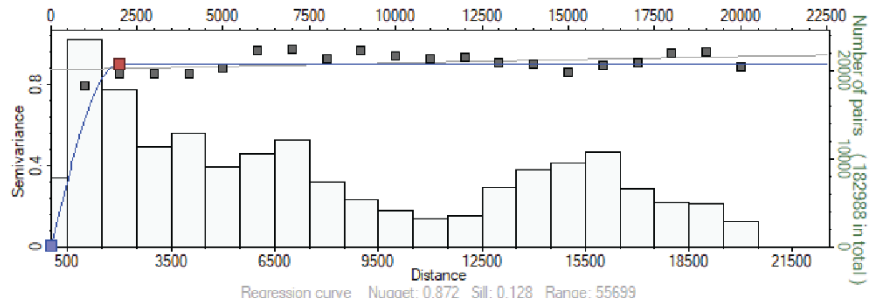


Variogram Map

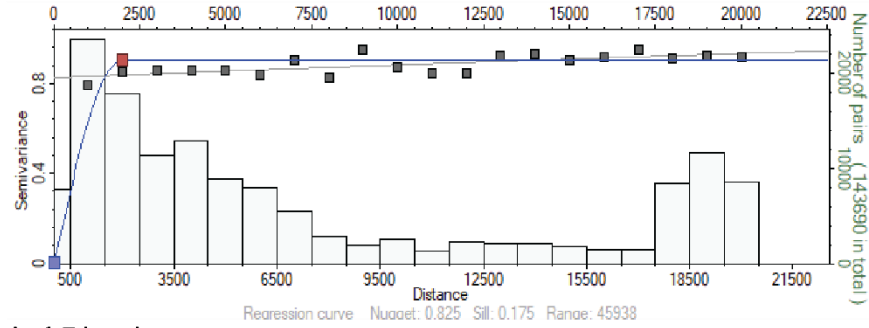


Unit 2D: Heterolithic Sandstone	
Azimuth (deg)	310
Major range (m)	1700
Minor range (m)	800
Vertical range (m)	13

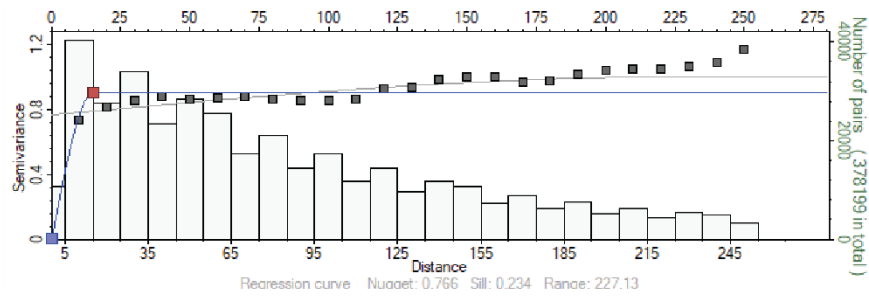
Major Direction



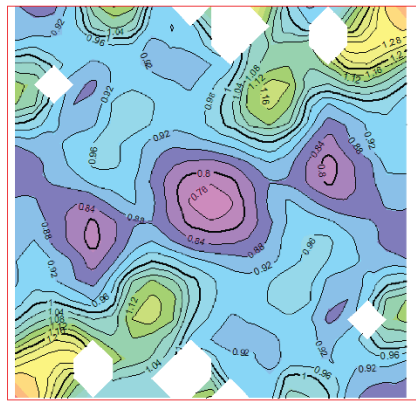
Minor Direction



Vertical Direction

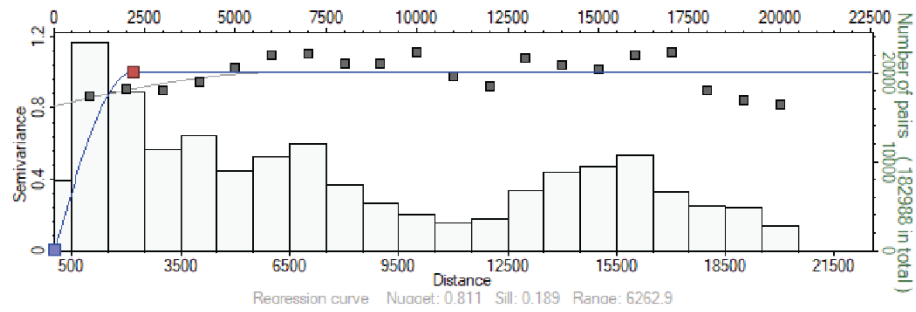


Variogram Map

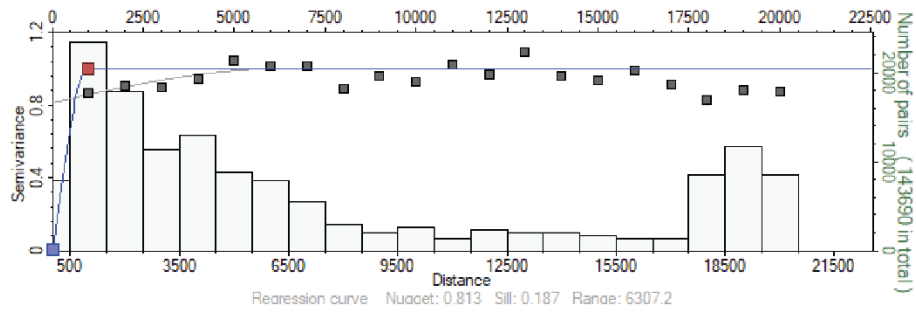


Unit 2D: Sandstone	
Azimuth (deg)	310
Major range (m)	2200
Minor range (m)	1000
Vertical range (m)	15

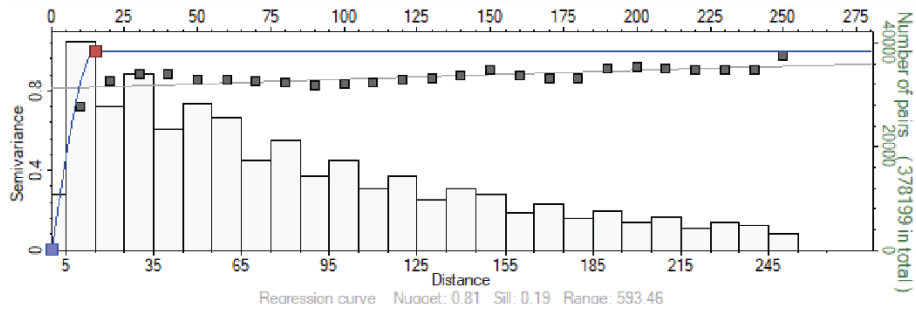
Major Direction



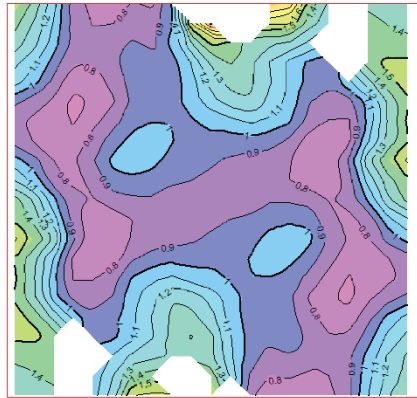
Minor Direction



Vertical Direction

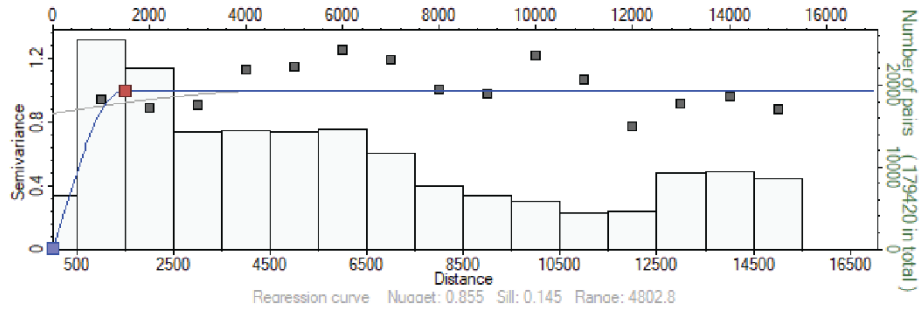


Variogram Map

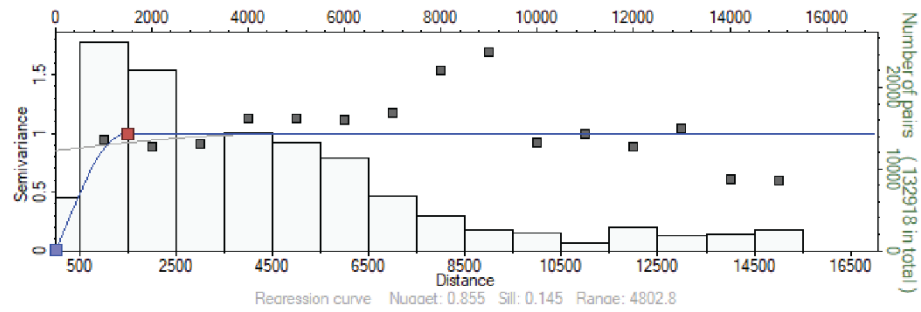


Unit 2C: Coal	
Azimuth (deg)	310
Major range (m)	1500
Minor range (m)	1500
Vertical range (m)	10

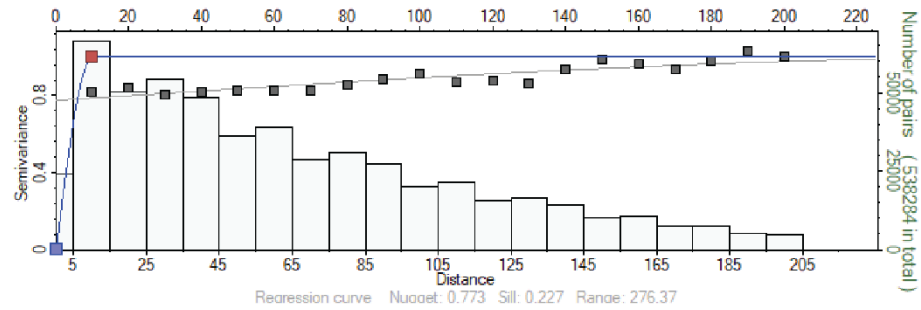
Major Direction



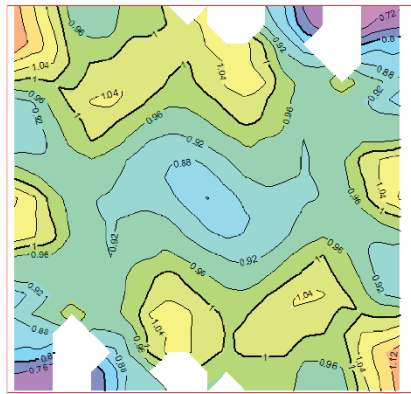
Minor Direction



Vertical Direction

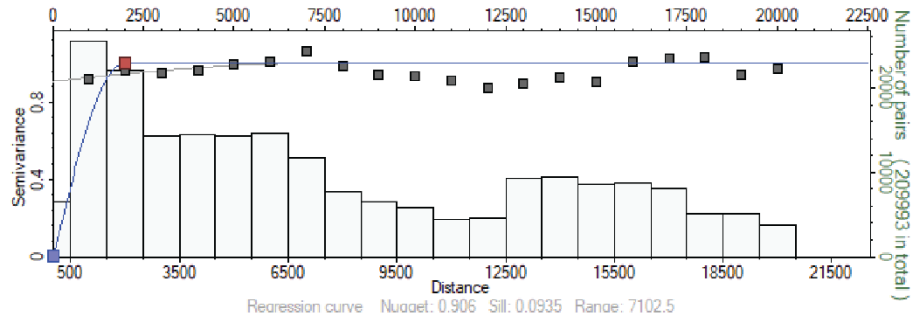


Variogram Map

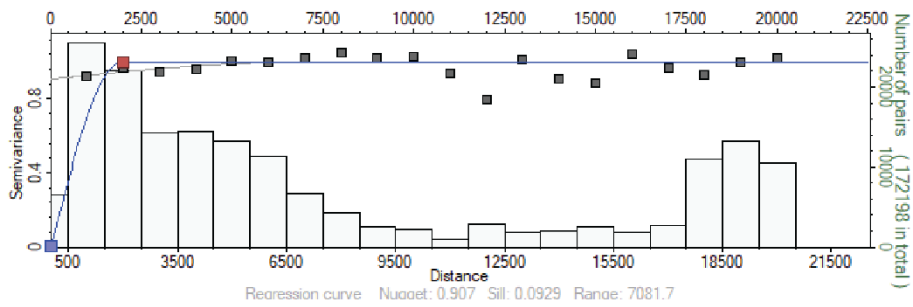


Unit 2C: Claystone	
Azimuth (deg)	310
Major range (m)	2000
Minor range (m)	2000
Vertical range (m)	20

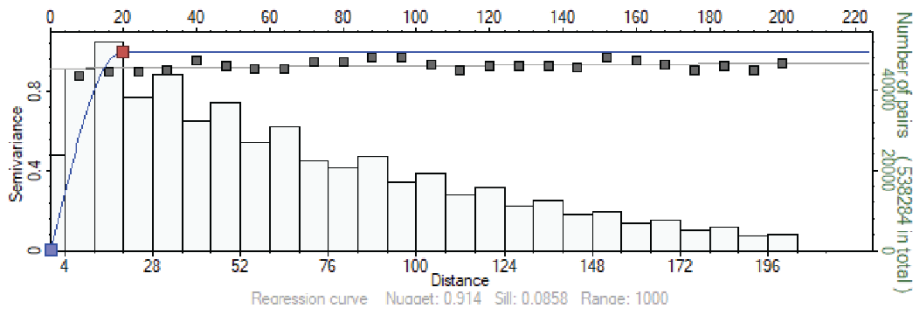
Major Direction



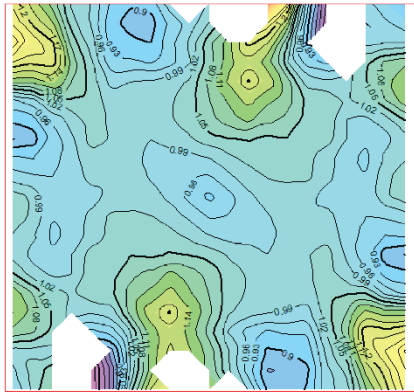
Minor Direction



Vertical Direction

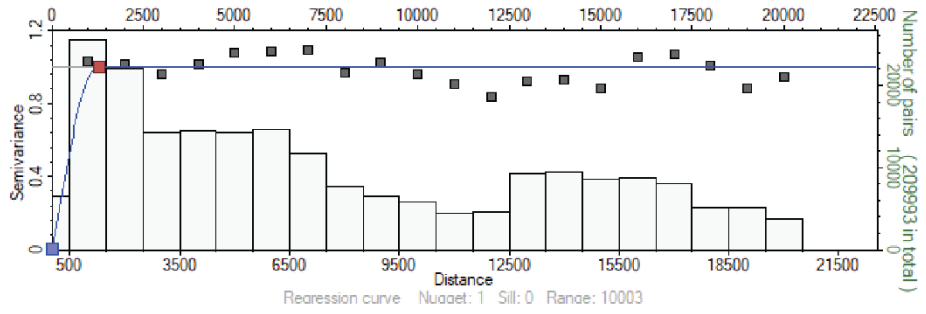


Variogram Map

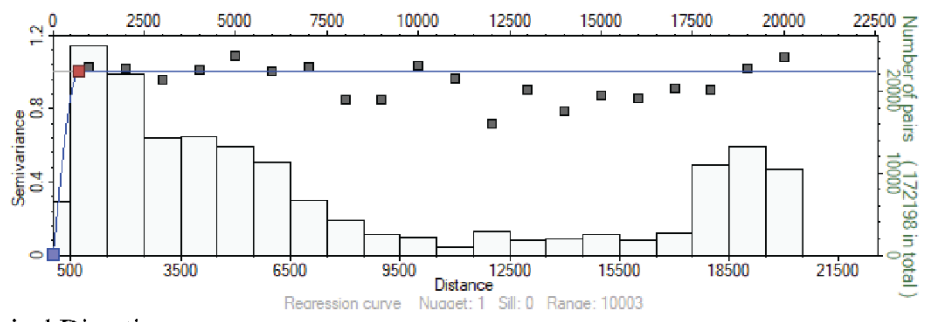


Unit 2C: Heterolithic Sandstone	
Azimuth (deg)	310
Major range (m)	1300
Minor range (m)	700
Vertical range (m)	8

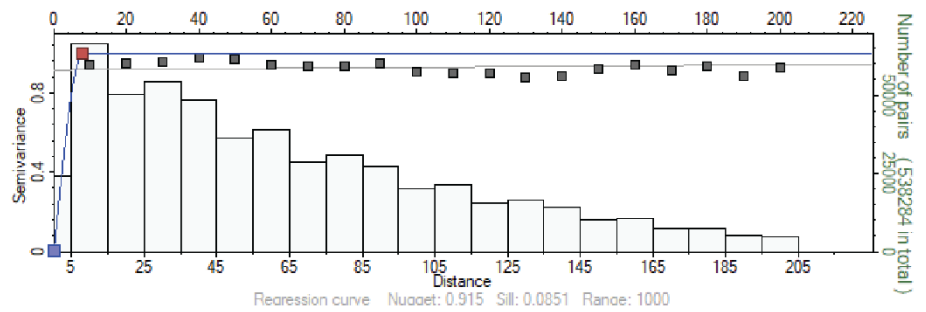
Major Direction



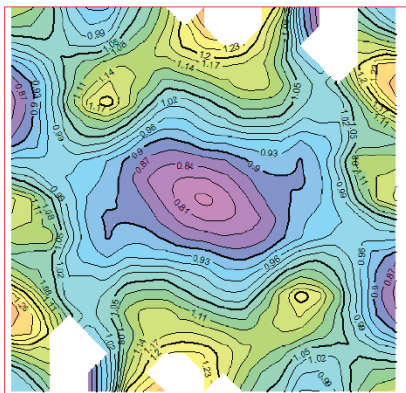
Minor Direction



Vertical Direction

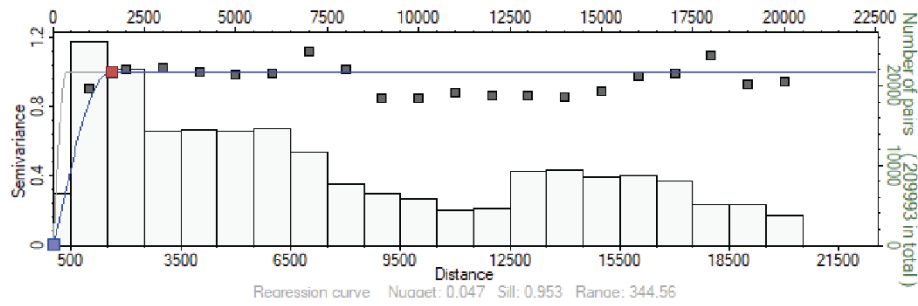


Variogram Map

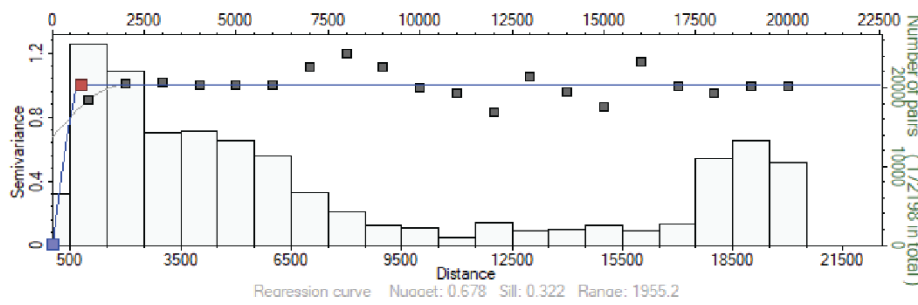


Unit 2C: Sandstone	
Azimuth (deg)	310
Major range (m)	1600
Minor range (m)	800
Vertical range (m)	10

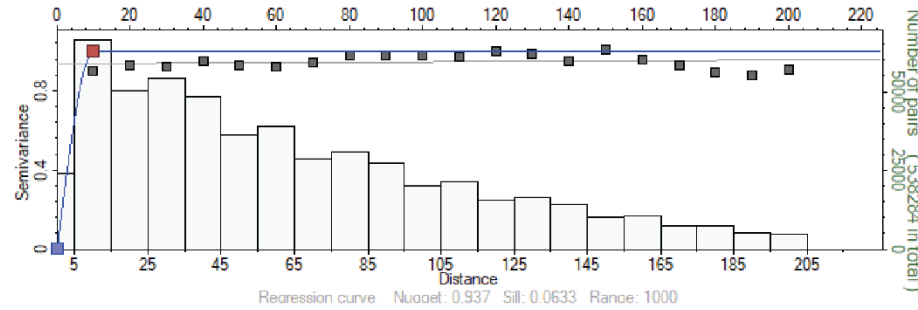
Major Direction



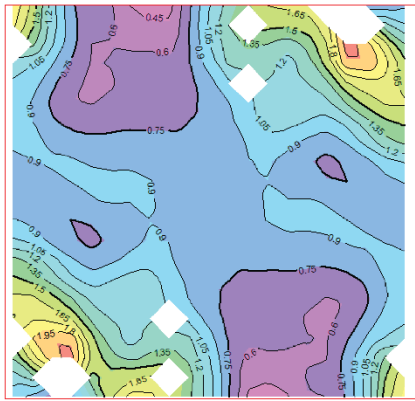
Minor Direction



Vertical Direction

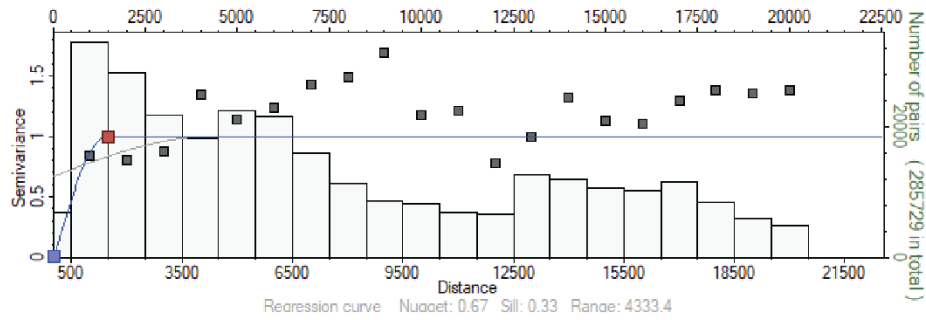


Variogram Map

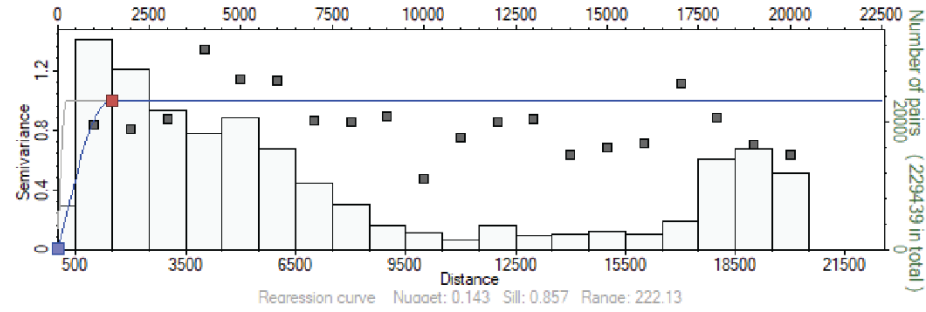


Unit 2B: Coal	
Azimuth (deg)	310
Major range (m)	1500
Minor range (m)	1500
Vertical range (m)	8

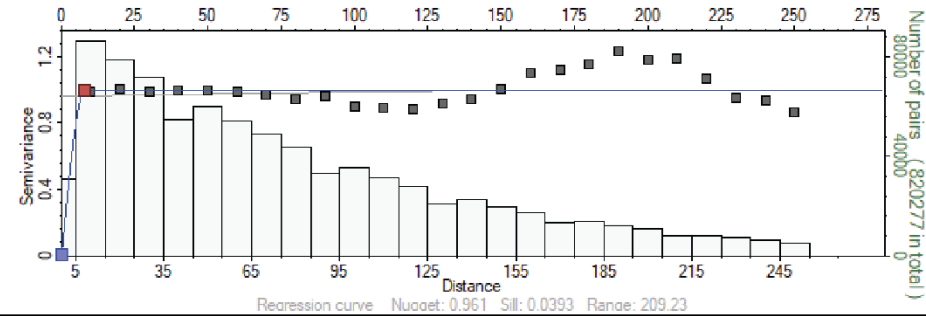
Major Direction



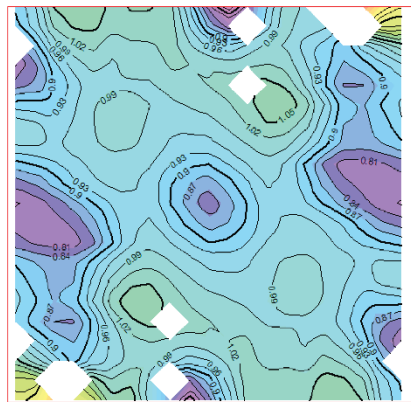
Minor Direction



Vertical Direction

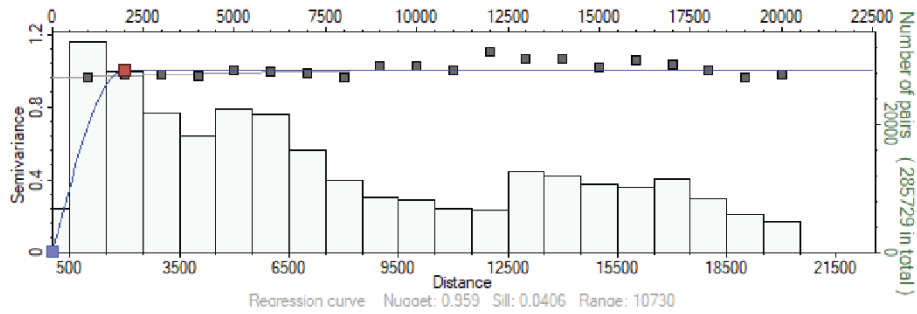


Variogram Map

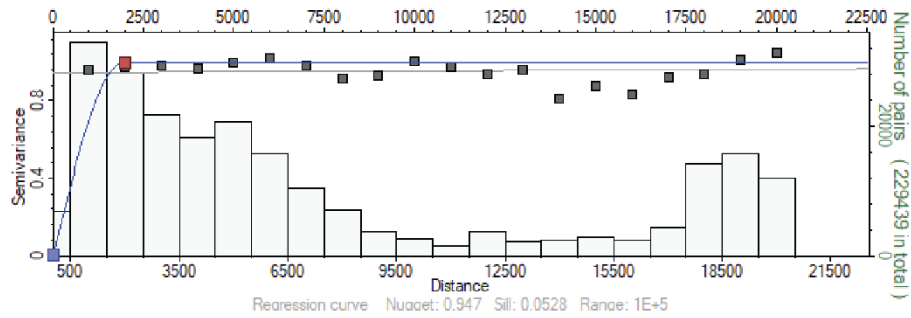


Unit 2B: Claystone	
Azimuth (deg)	310
Major range (m)	2000
Minor range (m)	2000
Vertical range (m)	18

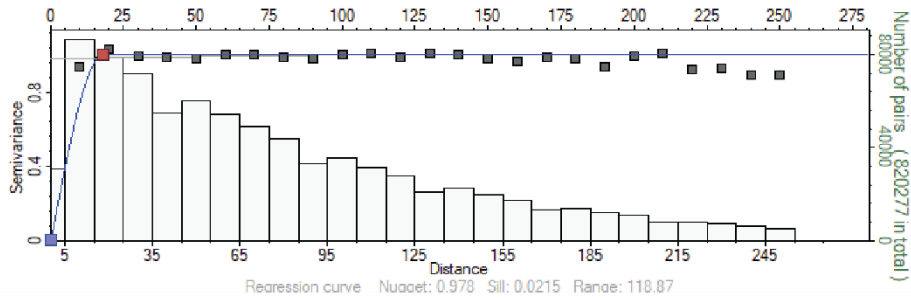
Major Direction



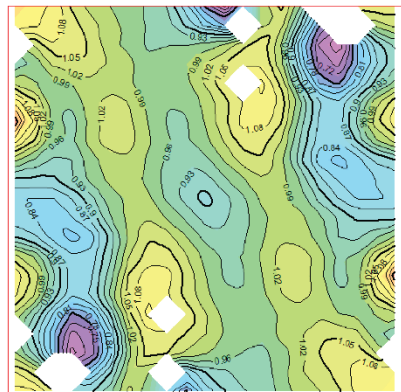
Minor Direction



Vertical Direction

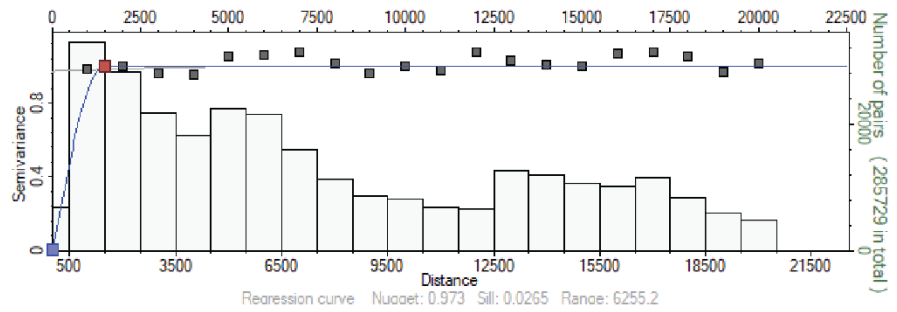


Variogram Map

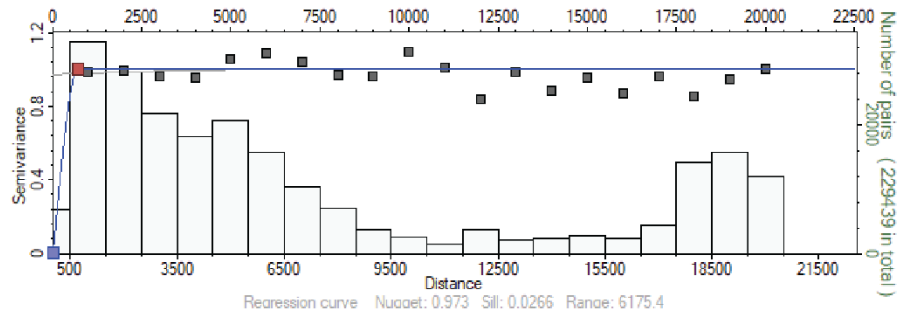


Unit 2B: Heterolithic Sandstone	
Azimuth (deg)	310
Major range (m)	1500
Minor range (m)	700
Vertical range (m)	9

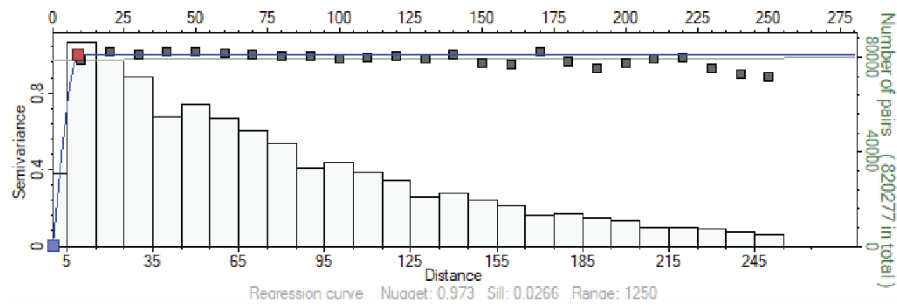
Major Direction



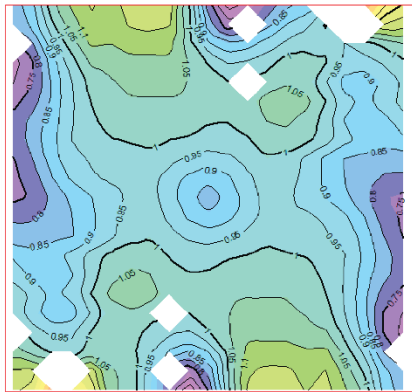
Minor Direction



Vertical Direction

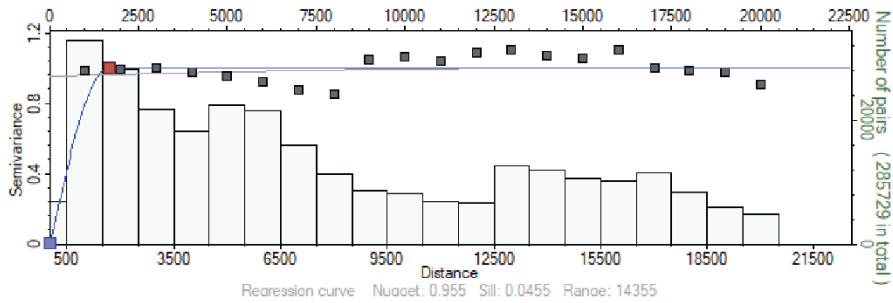


Variogram Map

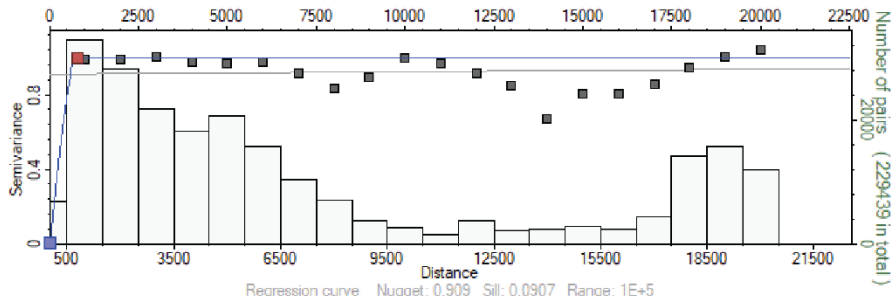


Unit 2B: Sandstone	
Azimuth (deg)	310
Major range (m)	1700
Minor range (m)	800
Vertical range (m)	12

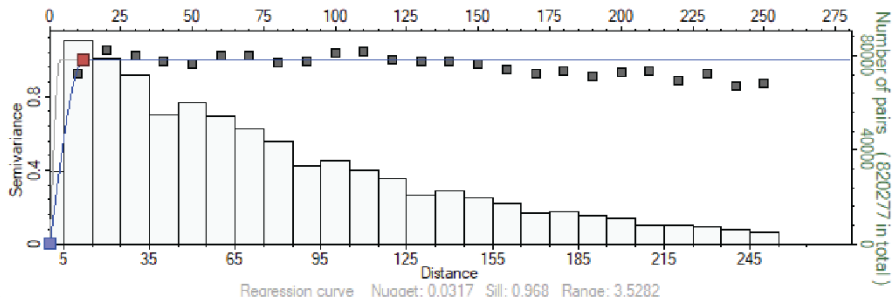
Major Direction



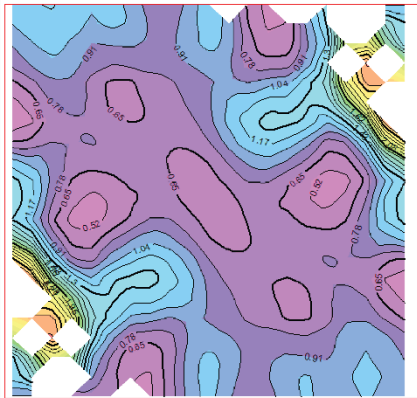
Minor Direction



Vertical Direction

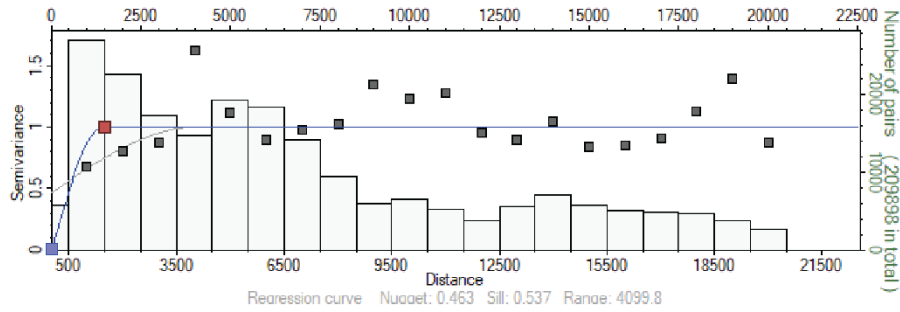


Variogram Map

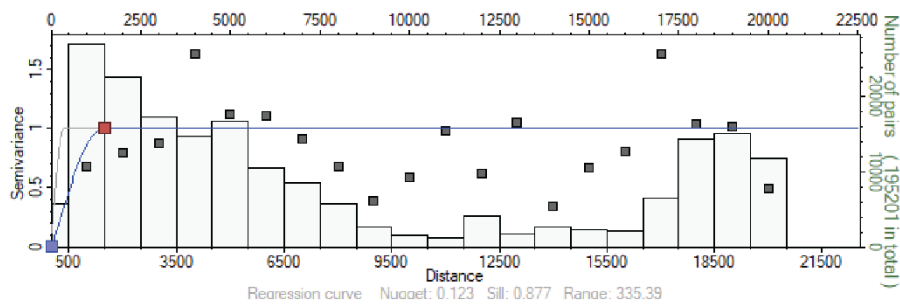


Unit 2A: Coal	
Azimuth (deg)	310
Major range (m)	1500
Minor range (m)	1500
Vertical range (m)	8

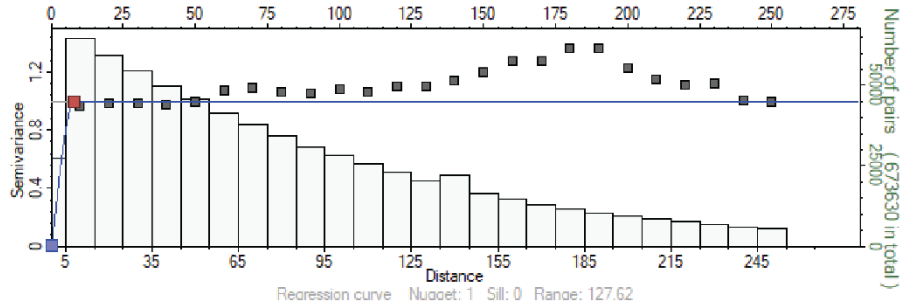
Major Direction



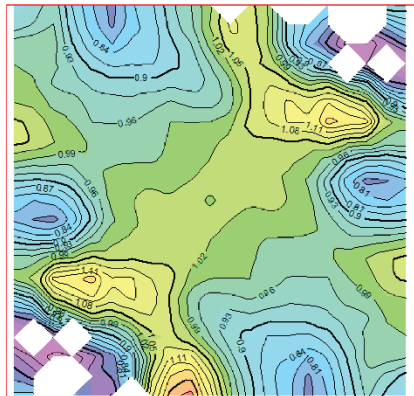
Minor Direction



Vertical Direction

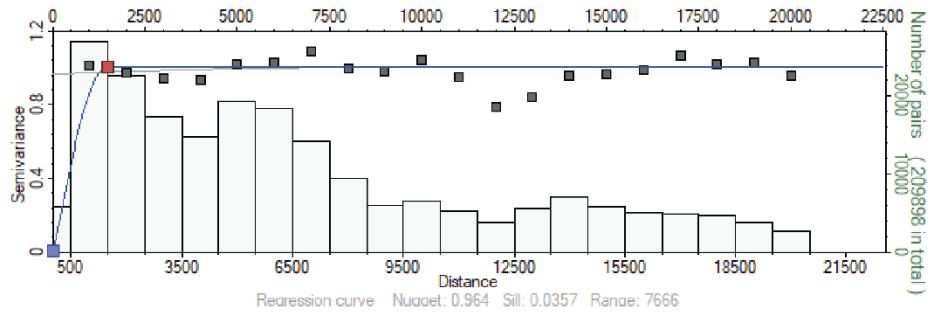


Variogram Map

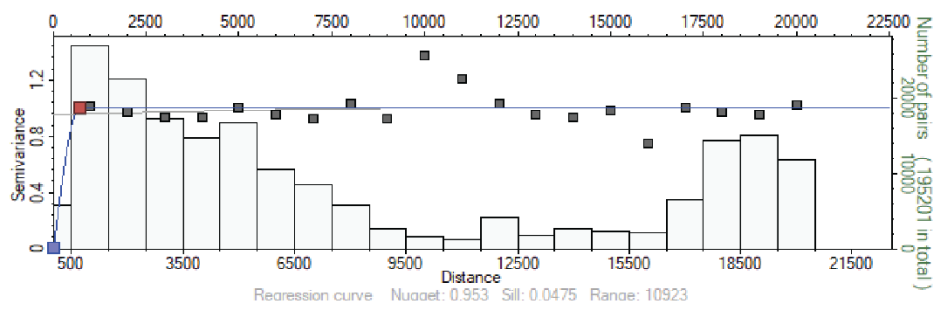


Unit 2A: Heterolithic Sandstone	
Azimuth (deg)	310
Major range (m)	1500
Minor range (m)	700
Vertical range (m)	9

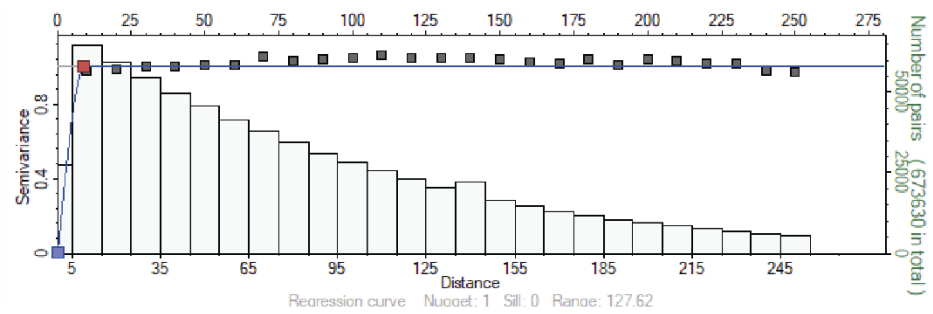
Major Direction



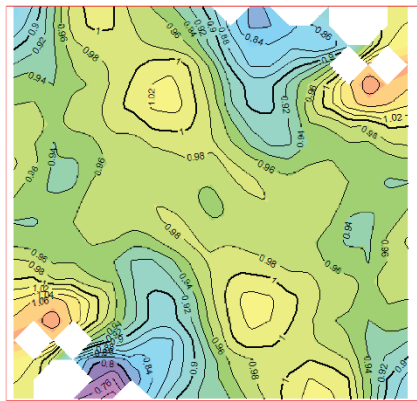
Minor Direction



Vertical Direction

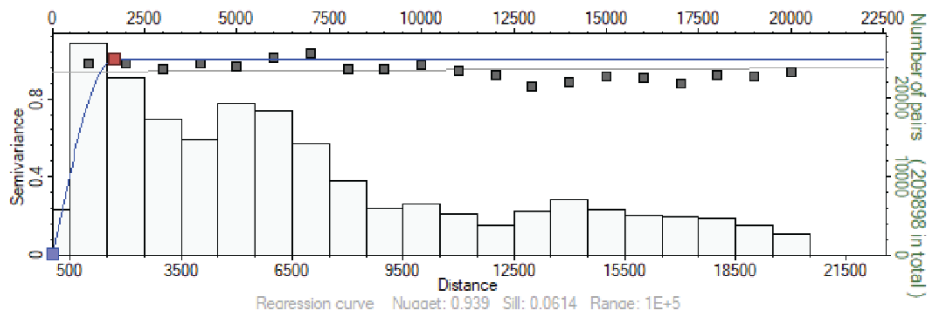


Variogram Map

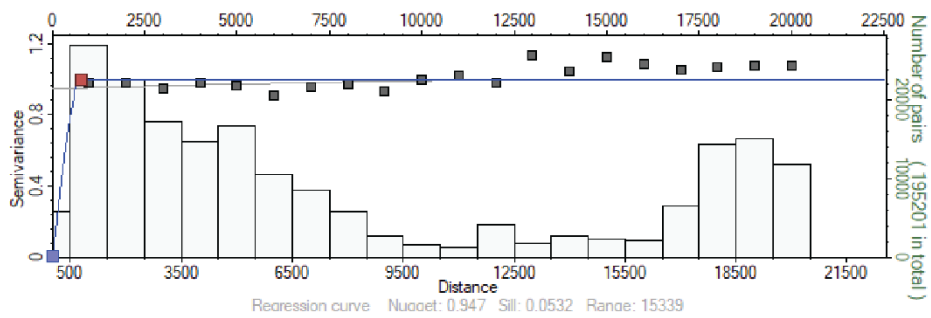


Unit 2A: Sandstone	
Azimuth (deg)	310
Major range (m)	1700
Minor range (m)	800
Vertical range (m)	11

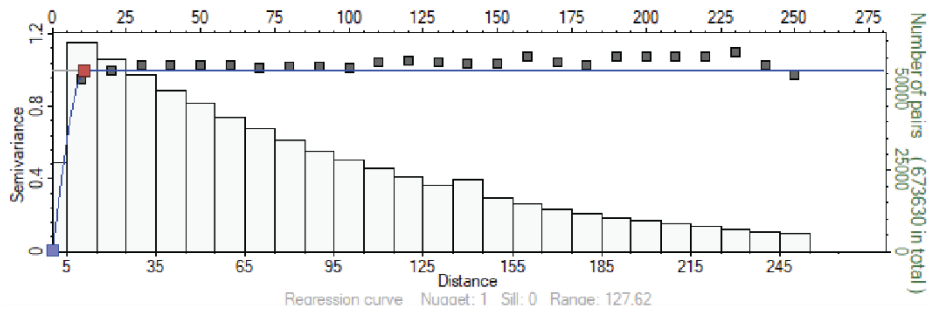
Major Direction



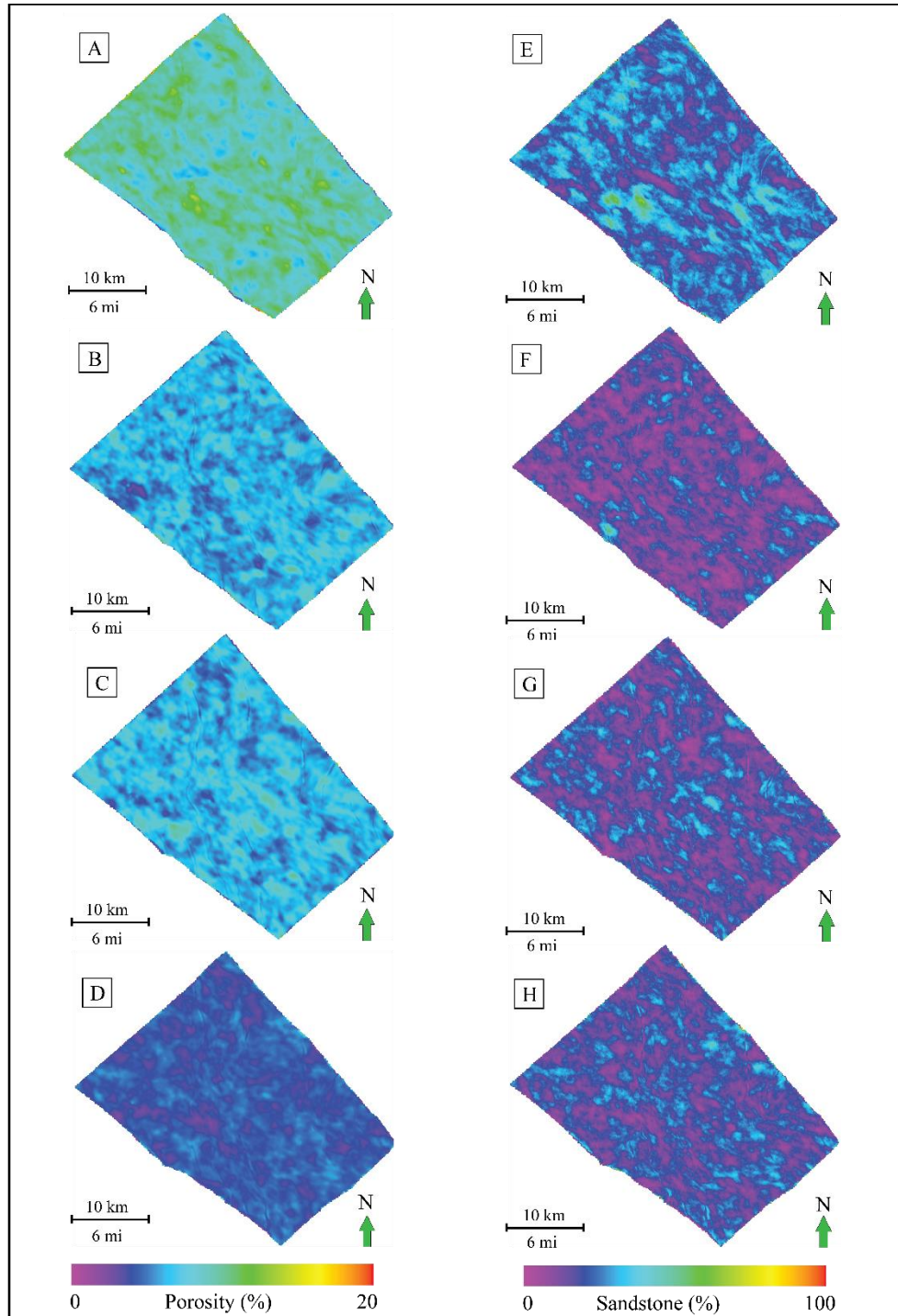
Minor Direction



Vertical Direction

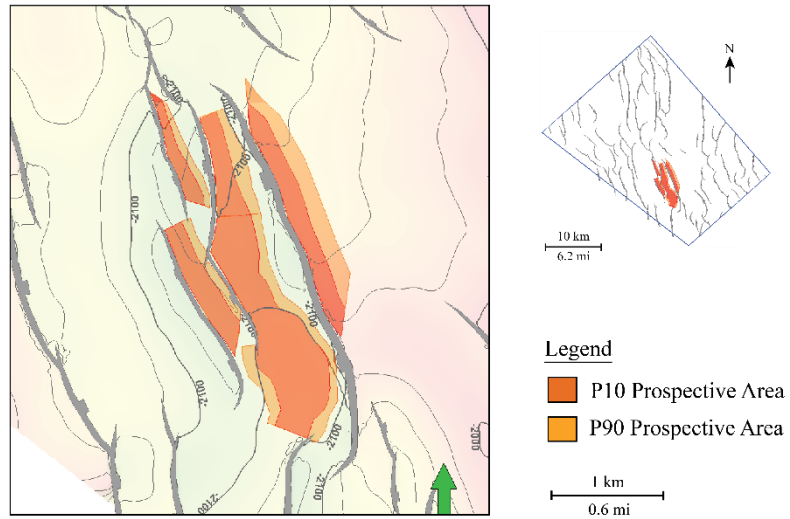


Appendix E: Spatial Distribution of Lithology and Reservoir Quality

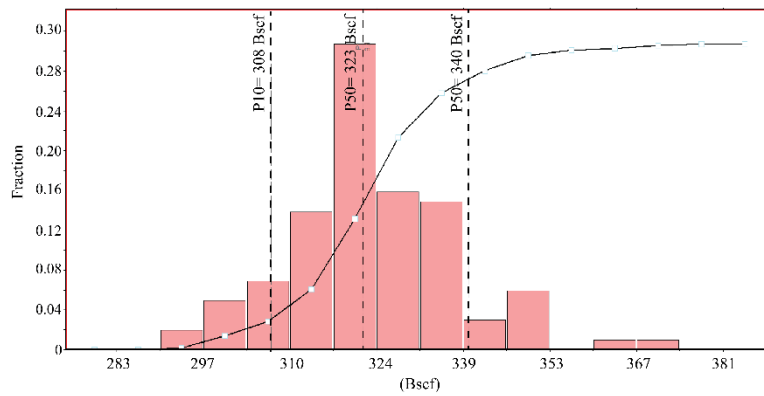


Appendix E-1. Average effective porosity maps (left) and sandstone proportion maps (Right) of A) unit 2D, B) unit 2C, C) unit 2B, and D) unit 2A. These maps indicate that porosity increases stratigraphically upward, with an increasing amount of sandstone content especially in unit 2D.

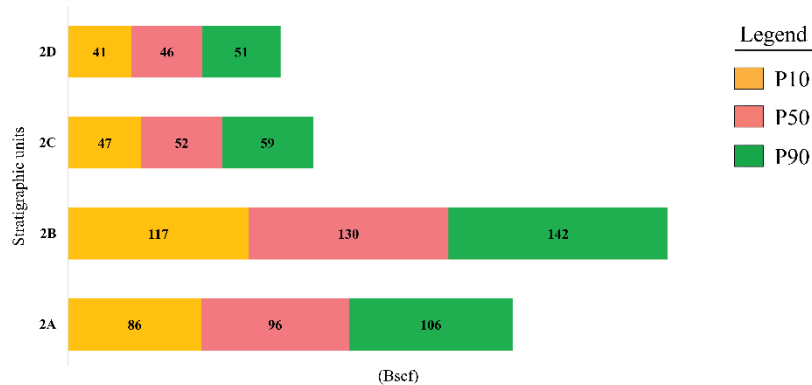
A) Prospective Area



B) Total Original Gas In-Place (OGIP)



C) Original Gas In-Place (OGIP) by Unit



Appendix E-2. OGIP estimation. A) Map showing the defined prospective area at P10 and at P90 according to a combination of the structural and stratigraphic trap. B) Histogram showing a total prospective OGIP distribution. C) Graph presenting OGIP distribution in each stratigraphic unit.